



저작자표시-비영리-동일조건변경허락 2.0 대한민국

이용자는 아래의 조건을 따르는 경우에 한하여 자유롭게

- 이 저작물을 복제, 배포, 전송, 전시, 공연 및 방송할 수 있습니다.
- 이차적 저작물을 작성할 수 있습니다.

다음과 같은 조건을 따라야 합니다:



저작자표시. 귀하는 원저작자를 표시하여야 합니다.



비영리. 귀하는 이 저작물을 영리 목적으로 이용할 수 없습니다.



동일조건변경허락. 귀하가 이 저작물을 개작, 변형 또는 가공했을 경우에는, 이 저작물과 동일한 이용허락조건하에서만 배포할 수 있습니다.

- 귀하는, 이 저작물의 재이용이나 배포의 경우, 이 저작물에 적용된 이용허락조건을 명확하게 나타내어야 합니다.
- 저작권자로부터 별도의 허가를 받으면 이러한 조건들은 적용되지 않습니다.

저작권법에 따른 이용자의 권리는 위의 내용에 의하여 영향을 받지 않습니다.

이것은 [이용허락규약\(Legal Code\)](#)을 이해하기 쉽게 요약한 것입니다.

[Disclaimer](#)

공학박사 학위논문

Novel Synthesis of Nanoporous BN (CNB) and Their Characteristics

미세 다공성 BN (CNB) 의 합성과 그 특성

2014 년 8 월

서울대학교 대학원

재료공학부

김진홍

Novel Synthesis of Nanoporous BN (CNB) and Their Characteristics

지도 교수 강 신 후

이 논문을 공학박사 학위논문으로 제출함
2014 년 8 월

서울대학교 대학원
재료공학부
김 진 홍

김진홍의 공학박사 학위논문을 인준함
2014 년 8 월

위 원 장 홍 성 현 (인)

부위원장 남 기 태 (인)

위 원 강 신 후 (인)

위 원 김 용 선 (인)

위 원 연 순 화 (인)

Abstract

Since its first synthesis, carbide-derived carbon has been examined for use in various applications, and its performance has been both interesting and outstanding. Despite its useful conformal character, its variety of chemical composition is limited because functionalized atoms in its carbonaceous structure are unstable during high-temperature processing. In this thesis, we demonstrate the novel synthetic method for the carbon analogue heterogeneous structure, especially with nitrogen and boron, by chlorination. The large scale fabrication is possible by this method under moderate conditions.

As an adjacent atom of carbon, nitrogen and boron are complementary to one other regardless of existence of carbon. Although they are bonded directly to form B-N moiety as the most stable state, the enhancement of nitrogen stability by boron addition still works even they are not. Under this concept, we synthesized porous C-N-Bs with several compositions successively without complex procedure.

The noticeable hydrogen (H_2) and carbon dioxide (CO_2) gas adsorptions were observed up to their compositions and surface area. At first, porous boron nitride indicates higher heat of adsorption for H_2 than carbonous materials. Whereas a hollow spherical nitrogen- and boron-co-doped porous carbon structure, developed by a nitrogen-rich precursor, show high CO_2 capture at ambient temperature and 1 bar with an excellent CO_2/N_2 selectivity.

Moreover, better capture abilities are expected if synthesized porous C-N-Bs are substituted by other proper elements or activated. The former can enhance the binding energy of guest molecules and the latter would enlarge the surface area.

Keywords: carbide derived carbon, boron nitride, nitrogen doping, hydrogen storage, carbon capture and storage, DFT calculation

Student number: 2008-20636

Contents

Abstract

Contents

List of Figures

List of Tables

1. Introduction	1
1. 1. Current study on porous C-N-B	1
1. 1. 1. Porous carbon	1
1. 1. 2. Porous boron nitride (BN).....	4
1. 1. 3. Porous nitrogen and boron co-doped carbon (CNB)	8
1. 2. Gas storage in porous materials	11
1. 2. 1. Hydrogen storage.....	11
1. 2. 2. Carbon dioxide (CO ₂) capture.....	17
1. 3. Aim of the work	21
2. Experimental procedure	22
2. 1. Synthesis of porous materials	22
2. 1. 1. Synthesis of porous BN	22
2. 1. 2. Synthesis of porous CNB.....	22
2. 1. 3. Chemical activation of porous CNB.....	23
2. 2. Characterization	24
2. 2. 1. Characterization of porous BN.....	24

2. 2. 2. Characterization of porous CNB	24
2. 3. Calculation details	25
2. 3. 1. Aluminum doped BN for hydrogen storage	25
2. 3. 1. Formation energy of nitrogen functional group in graphene	26
3. Results and discussion.....	28
3. 1. Porous BN.....	28
3. 1. 1. Synthesis of porous BN	28
3. 1. 2. Hydrogen storage of porous BN.....	41
3. 1. 3. Formation energy of Al- doped BN	46
3. 1. 4. Hydrogen adsorption properties of Al- doped BN.....	50
3. 1. 5. Density of states (DOS) investigation of Al- doped BN	55
3. 1. 6. Conclusions	61
3. 2. Porous CNB	63
3. 2. 1. Synthesis of porous CNB.....	63
3. 2. 2. Theoretical consideration of CNB	82
3. 2. 3. CO ₂ capture of porous CNB	86
3. 2. 4. Synthesis of super-activated CNB	91
3. 2. 5. CO ₂ capture of super-activated CNB	101
3. 2. 6. Conclusions	107
4. Overall conclusions	109
References	111

Further works	127
Publications List.....	128
Abstract (korean).....	129

List of Figures

Figure 1. Classification of BN materials. Microscope pictures are reprinted from [10], [13], [14] and [15].

Figure 2. General methods of porous BN synthesis. Substitution (top) and template (bottom) method.

Figure 3. Classification of CNBs. Microscope pictures are reprinted from [31], [32] and [36].

Figure 4. ¹¹B MAS NMR spectra of CNB samples reprinted from [37].

Figure 5. Various candidates to improve hydrogen storage in porous substrates. Spillover (a, reprinted from [57]), Kubas binding (b, reprinted from [64]), electrostatic interaction (c, reprinted from [70]).

Figure 6. Theoretical consideration of BNs for hydrogen storage using activation (a, reprinted from [79]), metal doping (b, reprinted from [80]), substitution (c, reprinted from [81]) methods.

Figure 7. Post-, Pre- and oxyfuel combustion process reprinted from [85].

Figure 8. Schematic diagram of chlorination procedure.

Figure 9. Schematic diagram of typical carbide derived carbon method (a) and our developed ceramic derived boron nitride method (b).

Figure 10. Change of Gibbs free reaction energy of following equation:
$$\text{TiB}_2(\text{s}) + 2\text{TiN}(\text{s}) + 6\text{Cl}_2(\text{g}) = 2\text{BN}(\text{s}) + 3\text{TiCl}_4(\text{g}).$$

Figure 11. XRD diffraction patterns of synthesized BNs.

Figure 12. B 1s (left) and N 1s (right) XPS spectra of BN-600.

Figure 13. EELS spectra of BN-600.

Figure 14. FE-SEM images of BN series (scale bar: 0.2 μm).

Figure 15. 77K N₂ isotherms of the BN samples. Closed symbols represent adsorption and open symbols represent desorption.

Figure 16. Micropore size distribution of BN series based on MP-plot method.

Figure 17. Low-pressure hydrogen uptake properties of BN series at 77K. Closed symbols for adsorption and open symbols for desorption.

Figure 18. Hydrogen adsorption uptake of BN-600 at low pressures (a). Black for 77K, red for 87K, respectively. Heat of adsorption (Q_{st}) of BN-600, CDC-800 and activated carbon (AC) and single wall carbon nanotube (SWCNT) as a function of the hydrogen uptake (b).

Figure 19. Geometrical configuration of Al doped BN sheet.

Figure 20. Geometrical optimization of Al-doped BN sheet after first hydrogen molecule adsorption.

Figure 21. Geometrical difference between first and second hydrogen molecule adsorption on Al- doped BN sheet.

Figure 22. Change of density of states (DOS). Free hydrogen molecule with Al- doped BN sheet (up), Al- doped BN sheet after first hydrogen molecule adsorption and that after second hydrogen molecule adsorption. Red line represents PDOS of H-1s orbitals and black line represents PDOS of Al- 2p orbitals.

Figure 23. Change of density of states (DOS) as increase of adsorbed hydrogen molecules on Al- doped BN sheet. Dashed square means the level repulsion portion.

Figure 24. Geometry and DOS of Ni- doped BN sheets ((a), (b)) compared Al-

doped BN sheet ((c), (d)).

Figure 25. Geometry of two aluminum- doped BN sheet which adsorbed fifth hydrogen molecules when hydrogen adsorbed on the opposite side (a) or same side (b).

Figure 26. N₂ adsorption (ad, filled circles) and desorption (de, unfilled circles) curves of CNs (a) and CNBs (b) at 77 K.

Figure 27. FE-SEM images of Ti(C_xN_y) precursors (left) and their corresponding CNBs (right).

Figure 28. TEM images of (a) CNB73 and (c) CNB55, and high-resolution TEM images of (b) CNB73 and (d) CNB55. Red circles in (b) and (d) indicate short graphitic layers.

Figure 29. TEM images of (a) CN37 and (b),(c) CNB37. (d) High-resolution TEM image of CNB37. Inset in (c) shows SAED pattern at the shell area marked in (c) by the rectangular dashed line.

Figure 30. XRD spectra of synthesized CNs and CNBs.

Figure 31. Proposed mechanism for the formation of hollow CNB37 structure where titanium, carbon or nitrogen, boron, and chlorine are represented by

pink, black, blue, and green spheres, respectively. A quartered section of the CNB37 is excluded for clarity.

Figure 32. Elemental mapping of (a) carbon, (b) nitrogen, and (c) boron, and (d) EELS spectrum of CNB37 in the same region.

Figure 33. TEM images of CNB37 made with excess boron precursor and its corresponding EELS spectra for the regions of C- and BN-rich phases.

Figure 34. XPS N 1s spectra of (a) CN37 and (b) CNB37. Each peak is deconvoluted into several functional groups as Npyr (398.2 eV), Nq (400.8 eV), and N–O (402.8 eV).

Figure 35. XPS N 1s spectra of CN55 (a), CNB55 (b), CN73 (c), and CNB73 (d). Each spectrum is deconvoluted into Npyr, Nq, and N–O, respectively.

Figure 36. XPS B 1s spectra of CNB37 (a), CNB55 (b), and CNB73 (c). Each spectrum is deconvoluted into BN and BC3.

Figure 37. Calculated formation energy for nitrogen doping in graphene sheets with respect to the boron position relative to nitrogen. The carbon, nitrogen, and boron atoms are shown in gray, red, and blue, respectively.

Figure 38. Geometric configuration of BCl₃ molecule in the vicinity of

quaternary nitrogen embedded in a graphene sheet (C, N, B, and Cl atoms are black, red, blue, and green, respectively).

Figure 39. (a) CO₂ adsorption isotherms of CNs and CNBs measured at 298 K and (b) their CO₂/N₂ selectivity versus N₂ molar fraction. Evaluation at 1 bar total pressure by the IAST method.

Figure 40. CO₂ capture properties of CNB37 at 298 K for five adsorption–desorption cycles.

Figure 41. FE-SEM images of synthesized K-CNBs.

Figure 42. TEM image of K-CNB37 and HR-TEM image of K-CNB37.

Figure 43. Schematic diagram of KOH activation process.

Figure 44. N₂ isotherms of synthesized K-CNBs. Close symbol represents adsorption (ad) and open symbol represent desorption (de).

Figure 45. TGA analysis of synthesized CNBs under air.

Figure 46. N 1s spectra of (a)CNB37, (b) CNB73, (c)K-CNB37 and (d)K-CNB73.

Figure 47. CO₂ adsorption isotherms of K-CNBs compared to corresponding

CNBs measured at 298K.

Figure 48. CO₂ uptakes of various nitrogenous carbon versus surface area.

Figure 49. CO₂ capture amount per surface area of various nitrogenous carbon versus surface area.

List of Tables

Table 1. Pore properties of the BN samples as a function of chlorination treatment temperature. ^a Surface area was measured using the BET method. ^b The total pore volume was measured up to $P/P_0=0.95$. ^c Micropore volumes were estimated using the MP-plot method. ^d Mesopore volumes were estimated using the BJH method (adsorption branch between $0.3 < P/P_0 < 0.95$). ^e Max of micropore diameter was estimated using the MP-plot method.

Table 2. Estimated values of the heat of the adsorption (Q_{st}) about BN-600 according to H_2 uptake based on Clausius-clapeyron equation and Langmuir-freundlich fitting.

Table 3. Formation energy of Aluminum substitution for boron in BN sheet according to various boron sources.

Table 4. The average hydrogen binding energy and related structural factors of Al- doped BN sheet.

Table 5. Textural properties of synthesized CNs and CNBs. Surface area was derived from the BET equation. The total pore volume was measured up to $P/P_0 = 0.99$. Micro- and mesopore volumes were measured by the deBoer t-

plot and Barrett–Joyner–Halenda (BJH) methods (adsorption branch between $0.3 < P/P_0 < 0.80$), respectively. Yield is calculated based on the amount of C, N, and B in the precursors.

Table 6. Chemical composition and CO₂ capture properties of synthesized CNs and CNBs. Composition analyses are done by XPS. Values in parentheses are determined by EA for nitrogen and ICP-AES for boron. The ratio of nitrogen functional groups is evaluated from their areas. The amount of CO₂ captured and the CO₂/N₂ selectivities are measured at 298 K. A CO₂ partial pressure of 0.1 bar is selected as the standard for the determination of selectivity.

Table 7. Single-site Langmuir fitting values for IAST evaluation where each sample was fitted separately for CO₂ and N₂ adsorption.

Table 8. Overall properties of K-CNBs compared to corresponding CNBs. Nitrogen contents are measured by elemental analysis.

Table 9. CO₂ capture properties of various porous materials. CO₂/N₂ selectivity is evaluated by IAST method at 0.1 bar of CO₂ partial pressure.

1. Introduction

1. 1. Current study on porous C-N-B

1. 1. 1. Porous carbon

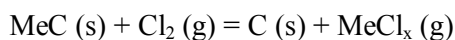
2nd period atoms have received lots of attention because of its light weighed bodies. Except 1S orbital ones, every electron in orbitals is recognized as valence electron in this period. So lots of effectiveness is expected especially in electrochemistry field. Lithium is maybe one of the most comprehensive examples to explain their advantages. Lots of efforts have been devoted to develop better Li-based energy storage materials such as Li-ion, Li-sulfur and Li-air batteries.

However, even before the intensive research on lithium, many researchers have focused on other atom in the same period. Carbon, abundant and inexpensive atom exists in 0- to 3-dimensional form, is without doubt an atom of many merits. It possesses not only high thermal and chemical stability but large surface area up to its synthetic procedure. Therefore, it is often selected for various applications, such as supporting materials, electrochemical devices, and gas storage materials.

Several methods are already discussed for this large surface area porous carbon and probably activated carbon is the most familiar and ubiquitous one.

It is produced by physical activation or mostly chemical activation from carbonous materials like coconut shell, coal, wood and etc. Since cheap materials can be used for precursor with a simple procedure, large scale production is available and they have been widely used.

Nevertheless of these advantages, activated carbons have limitations of control the pore size. Since pore size is important parameter for applications of general interests, narrow pore distribution of porous carbon has been recognized as the long-cherished desire. Carbide derived carbons (CDCs) are one of the most definite answer until now for these needs.¹⁻⁶ The general relation is expressed by follows



Since carbon is stable above around 200 °C in chlorine atmosphere, metal is selectively etched as a chloride gas phase. At first, it was considered as by-product of metal chloride. However, after their unique property of narrow size distribution was identified, they have been researched in various fields which include gas storage, lithium sulfur batteries and supercapacitors.

In CDCs, pore size and structure is determined by the precursor and the synthesis conditions. For example, narrow pore size distributed CDCs of 0.5~2.0nm were produced by chlorination of Titanium carbide (TiC) in various metal etching temperature.⁶ Furthermore, they possess high specific surface area (1000~3000m²/g) with a large pore volume (~1.6cm³/g).

However, despite of its useful conformal character with high porosity, the

variety in chemical composition is very limited because of the instability of functionalized atoms in carbonous structure under operating conditions.

1. 1. 2. Porous boron nitride (BN)

Boron nitride (BN) is recognized as cutting edge materials these days because of its unique properties. Among them, since hexagonal BN is structurally similar to graphite and electrical insulator (band gap $\sim 5.5\text{eV}$) at the same time, graphene related approaches are now actively in progress.⁷⁻⁹ Actually, the nanostructured BN not only possesses such electrical nature also displays other properties that would be attractive in a variety of applications, i.e., catalyst supports, gas sorption materials, including a high thermal conductivity, good oxidation resistance, and high thermal stability.^{10, 11} For these applications, high surface area from large pore volume is the key to maximize efficiency.

Boron nitride nanotubes (BNNTs) are one of the most interesting materials of the porous BN family. After discovery of carbon nanotubes (CNTs), they also got some interests as an analogue. It is successfully synthesized in 1995¹² and have been researched in various fields. Contrast to CNTs, which show metallic or semiconducting, BNNTs are electrically insulator. Arc-discharge, chemical vapor deposition (CVD), laser ablation are usually adopted to synthesis BNNTs.¹⁰ Not only nanotube types, but also other structures such as nanoparticles,¹³ nanosheets¹⁴ and hollow spheres¹⁵ are reported in recent years as shown in figure 1. BN, therefore, is considered as a key materials in electrochemical energy devices (EEDs) because of this diversity of classification.¹⁶

However, Porous BN has not yet been well developed. Although high-surface area BN (with surface areas of 150–550 m²/g) has been synthesized via substitution or template methods, these values are too lower than other porous materials.¹⁷⁻²² BNNTs themselves have some limitation for enlarge surface area as it observed in CNTs. Also contamination problems have plagued the former method and process complexity and costs render the latter method uneconomical. Moreover, nearly all BN studies have focused exclusively on the mesopore materials. For the variety of applications, microporous BN should be researched.

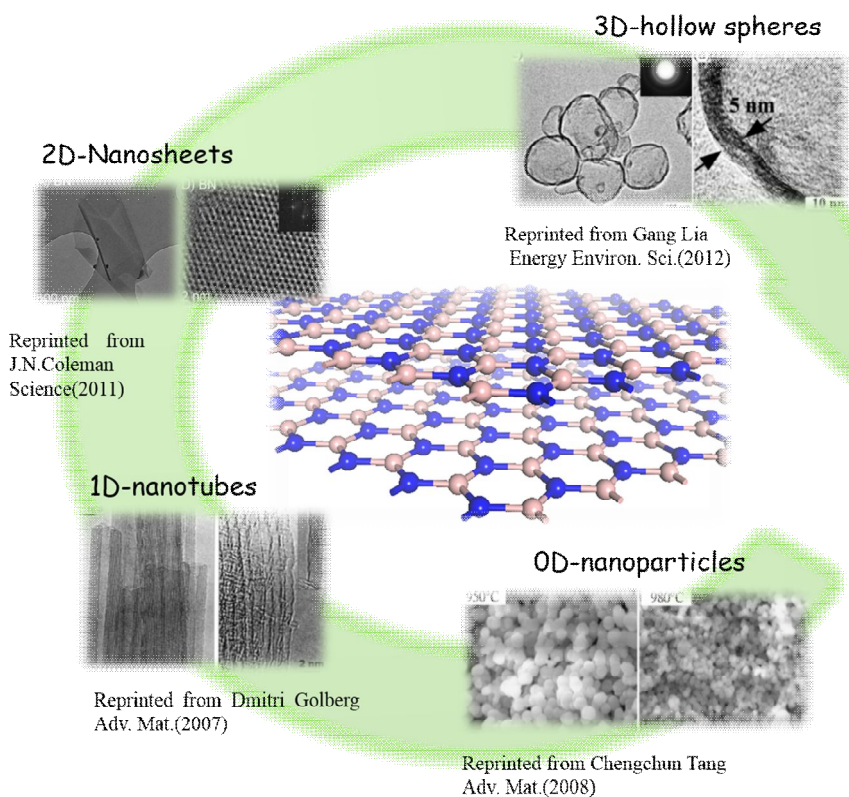


Figure 1. Classification of BN materials. Microscope pictures are reprinted from [10], [13], [14] and [15].

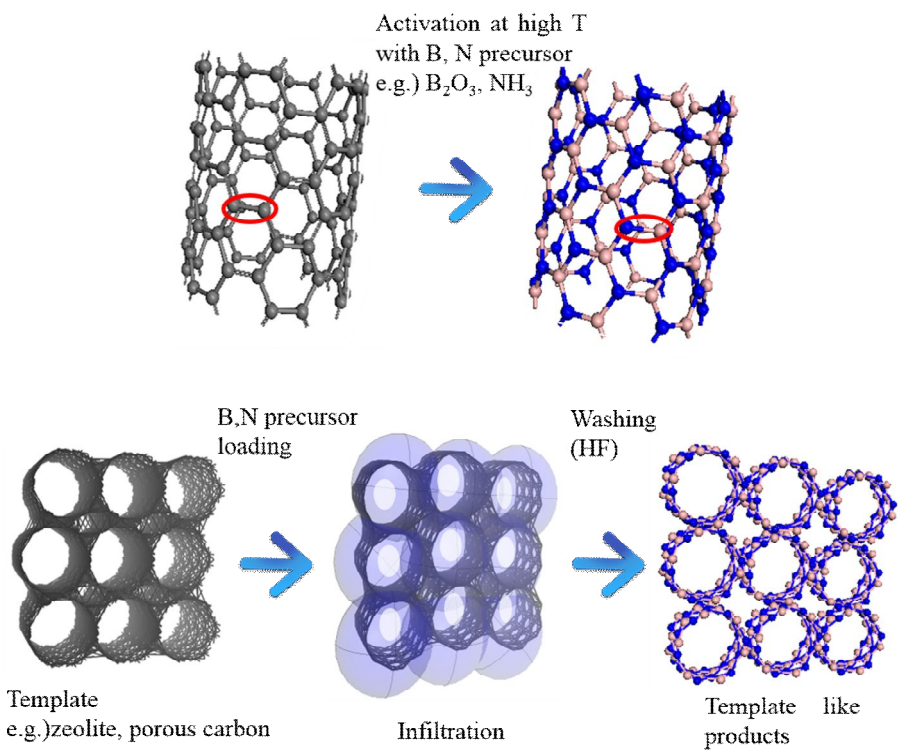


Figure 2. General methods of porous BN synthesis. Substitution (top) and template (bottom) method.

1. 1. 3. Porous nitrogen and boron co-doped carbon (CNB)

The nitrogen-doped porous carbon (CN) materials, which have been much explored, and are still under extensive investigation. Several synthesis methods, including ammonia heat treatment,²³ copolymerization followed by carbonization,²⁴ and template method, known as the most ubiquitous and effective way, with suitable nitrogen precursors, i.e., melamine,²⁵ acetonitrile,²⁶ and diaminobenzene,²⁷ already have been demonstrated. Whereas, boron-doped porous carbon (CB) has been rarely reported since the bonding between carbon and boron is too unstable under moderate conditions. CBs are known as materials requiring high-temperature synthetic processes and only a few papers reported the substitution of a small amount boron in porous carbon structure and demonstrated the possibility to improve gas sorption properties.^{28, 29}

In recent years, nitrogen and boron co-doped porous carbon (CNB) has been newly spotlighted. CNBs have been verified its utility as phosphors,³⁰ catalysts,^{31, 32} supercapacitors^{33, 34} and gas sorption materials.³⁵ It can also be existed as several structures as nanotubes³¹ or nanosheets^{32, 36} (figure 2). However, these materials usually consist of two separate phases, i.e., C-N rich phase and B-N rich phase owing to C-B instability.³⁷ It is difficult to obtain homogenous CNB framework. Therefore, the judicious selection for these CNBs is highly needed.

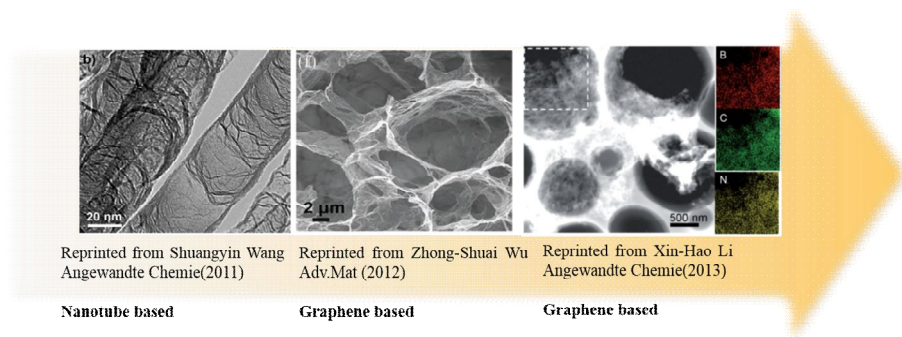


Figure 3. Classification of CNBs. Microscope pictures are reprinted from [31], [32] and [36].

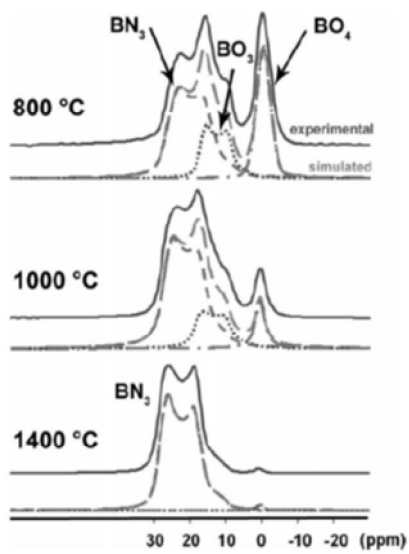


Figure 4. ^{11}B MAS NMR spectra of CNB samples reprinted from [37].

1. 2. Gas storage in porous materials

1. 2. 1. Hydrogen storage

The global economy of the 20th century has been characterized as a carbon economy. Given the projected trends in energy storage, the 21th century will likely see a transformation to a hydrogen economy. With the tremendous increase in interest in environmental preservation, much effort has been focused on hydrogen as a non-polluting energy delivery system.

Until now, several methods for storing hydrogen have been developed.³⁸⁻⁴³ Solid-state storage of hydrogen such as chemical compounds or adsorption on large surface area materials have lots of advantages from safety issue to small energy penalty.⁴⁴ Among them, physisorption shows promise due to its excellent kinetic properties. According to DOE's standard, hydrogen storage at ambient temperature should be increased to 5.5wt% at first and ideally be reached to 7wt%. But its intrinsic undesirable properties pose several challenges to the technologies associated with hydrogen storage. Several methods for storing hydrogen have been developed. Among them, physisorption shows promise due to its excellent kinetic properties. Carbonous materials and MOFs have been studied as candidate physisorption substrates in this area.⁴⁵⁻⁴⁸ These materials have yielded high and fully reversible storage rates; however, the binding energy between substrate and hydrogen molecules is too weak (4–6 kJ/mol van der waals force) to permit

stable storage at ambient temperatures. Bhatia and Myers proposed an average ideal target adsorption enthalpy of at least 13–15 kJ/mol.⁴⁹ Therefore low interaction energy is the main drawbacks to the use of physisorption in hydrogen storage applications.

To overcome this limitation of moderate hydrogen storage, lots of alternatives were proposed. Among them, spillover, Kubas binding and electrostatic interaction maybe the most promising candidates and shown in figure 5.

Among them, spill over mechanism is the oldest classical theory and already being discussed from several decades ago.⁵⁰ At first, it became known as catalyst not for hydrogen storage. Even though it is still being debated, this mechanism is a well-known phenomenon in the catalysis community. That for hydrogen storage has been discussed within a decades in several previous reports.⁵¹⁻⁵⁷ In this theory, nickel, palladium and platinum are work as hydrogen acceptor.⁵⁸ When hydrogen molecule approach to this metal, it is divided into atoms and form as metal hydride. Then this hydrogen atoms are spilled to the substrate, usually carbonous materials. But the experiments are not repeated well because of the large dependence of metal cluster size.⁵³ Also hydrogen uptake enhancement tend to concentrate on the low coverage. This kind of enhancement almost origin from metal hydride formation. Therefore, it is not easily desorbed under moderate temperature but also not enough amount to reach the goal.

On the other hand Kubas binding, proposed by Kubas in 1984,⁵⁹ show another possibilities for hydrogen storage. According to this theory, usual transition

metals such as titanium, iron, and etc., can bind several hydrogen molecules without any phase-transformation. It stands midway between hydrides and physisorption in binding strength, and therefore recognized as ideal system for H₂ storage.⁶⁰ Theoretically, the made compounds are stable at room temperature and needs moderate heat or decompression to liberate H₂.⁶¹⁻⁶⁴ Calcium as well as transition metals known to as a kuba binding acceptor theoretically.^{65, 66} Since some elongation occurs when hydrogen molecules interact with transition metals, we usually called this molecule as di-hydrogen. The mechanism of kuba binding is based on donation & back-donation process which means the interaction between transition metal d orbitals and H₂ σ (σ^*) orbitals. However, the main drawback of it is the high tendency of metal clustering because of their high cohesive energy. Since it needs a room for interaction with H₂, transition metal should be deposited atomically. Therefore, it is really hard to observe it experimentally except some premature results.⁶⁷⁻⁶⁹

The last candidate is electrostatic interaction.⁷⁰⁻⁷² It is combined by electrostatic effects and orbital interaction more precisely. The electrostatic interaction usually comes from small quadrupole moments of row H₂ or dipole moments induced by distorting the bonding H₂- σ orbitals. At this time, charge transfer, generated by orbital interaction, also can be occurred depending on the circumstance.⁷³ The metal cation caused the charge polarization and this polarity induce the enough hydrogen molecule binding force to the substrate. Probably ionic bonded hetero-structure maybe the best choice for this mechanism since there are no free ions. Some DFT calculation

already proved its potential in various composition or structure. However there are no experimental proof for this except some MOFs. Actually almost all the proposed structure are really hard to synthesize under present developed technology. Even though it could be done, surface area to interact with hydrogen molecules (the essential condition for enough gravimetric hydrogen storage) is too small. Moreover even in MOFs, metal ions already connected by ligands. So that metals could not provide enough room for hydrogen interaction and only small increase of heat of adsorption observed in consequence.⁷⁴ Therefore, it is really hard to anticipate realistic hydrogen storage mechanism in view of the results so far achieved.

Specifically, BN based hydrogen storage also gain lots of attention as carbonous materials does. BN itself is polar due to the electronegativity difference between the boron and nitrogen centers.² Its dipole moment yields a calculated binding energy between BN and hydrogen (90 meV) that is higher than the binding energies of carbonous materials (60 meV).^{75, 76} BNNT has been demonstrated to store up to 2.6 wt% H₂ at ambient temperature⁷⁷ under 10Mpa further increased up to 4.2 wt% by a post-production treatment procedure for surface area enlargement.⁷⁸ Even though, lots of the adsorbed hydrogens are not desorbed at ambient temperature, the result implies that hydrogen uptake can be increased when large surface are BN is adopted. Theoretical considerations have been vigorously done to find the effective way of hydrogen storage based on BN as shown in figure 6.⁷⁹⁻⁸¹ However, the practicality of them are not well demonstrated yet.

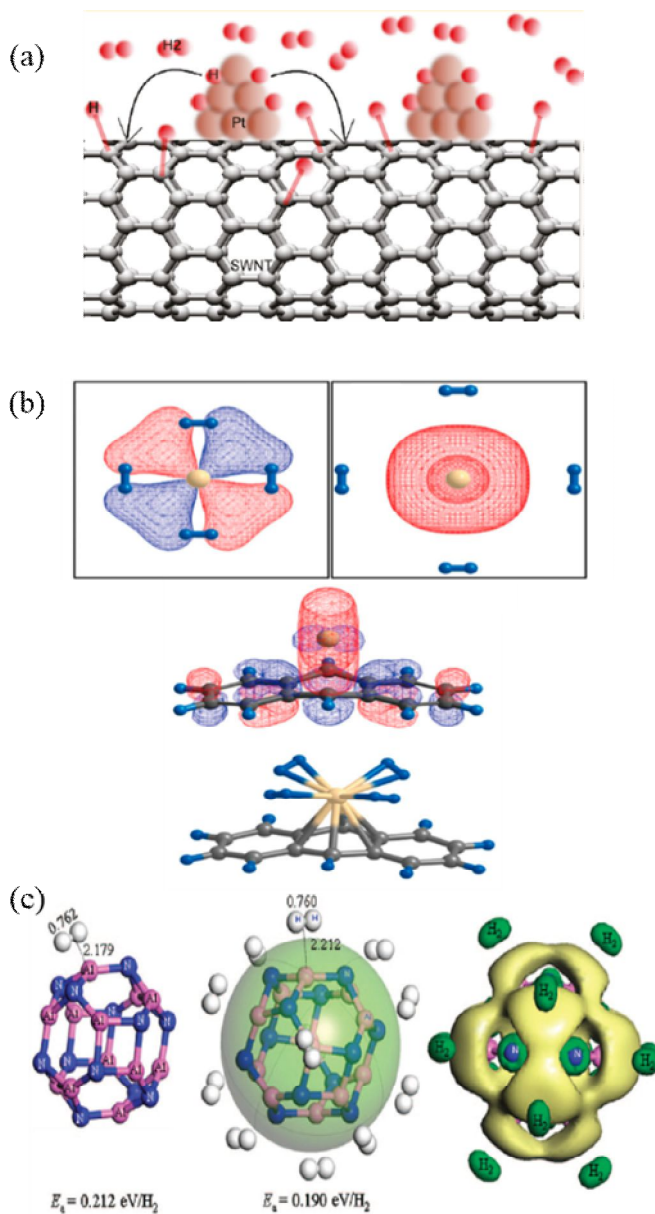


Figure 5. Various candidates to improve hydrogen storage in porous substrates. Spillover (a, reprinted from [57]), Kubas binding (b, reprinted from [64]), electrostatic interaction (c, reprinted from [70]).

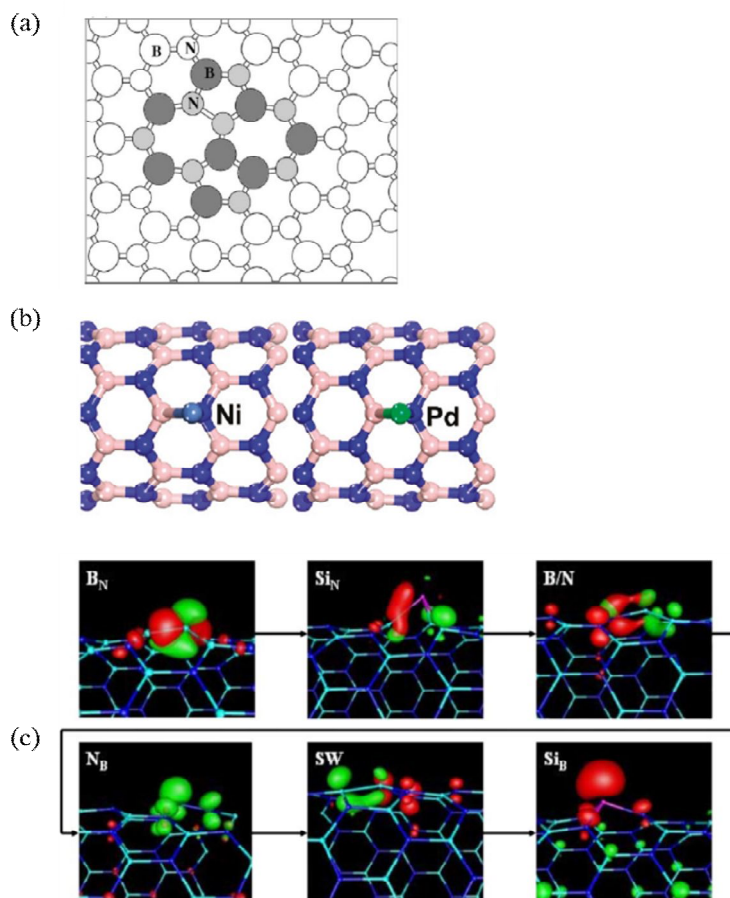


Figure 6. Theoretical consideration of BNs for hydrogen storage using activation (a, reprinted from [79]), metal doping (b, reprinted from [80]), substitution (c, reprinted from [81]) methods.

1. 2. 2. Carbon dioxide (CO₂) capture

Carbon capture and storage (CCS) technologies are a promising way to address the problem of global warming.⁸² There are three major options for this strategy and shown in figure 2. Pre-combustion methods are engaged in high CO₂ partial pressure and are worked for natural gas plants. It is usually adopted for hydrogen evolution system from methane rich fuel. After methane rich fuel is reacted with air at the high pressure and temperature, CO, CO₂ and H₂ gases is evolved. The main advantage of pre-combustion method is that the higher component concentrations and elevated pressures reduce the energy capture penalty of the process.⁸³

Oxyfuel combustions work at the pressurized CO₂-rich recirculation stream. During the combustion step, nitrogen is totally excluded by a preliminary air separation course. A high concentrated steam of CO₂ is produced and is circulated back into the system. Since it is based on the zero emission cycle, it is considered as very promising technology compared to other CCS candidates.⁸⁴

Post-combustion capture of CO₂ is applicable to conventional coal- or gas fired power plants.^{85, 86} Although above-mentioned methods have several advantages, they are not yet economically available such as the power generation reduction and the lack for scale up development. On the other hand, post-combustion already have been employed industrially from several decades ago. The low pressure of flue gas, which contain 10~15%

concentration of CO₂, is the main target for this method. Maybe aqueous amine solutions are the most promising system and have been used practically from now. It involves the passage of an aqueous solution down the top of an absorption tower when a stream is coming from the bottom.⁸⁷ However, some problems such as high energy-consuming regeneration, corrosion of the equipment and thermal and oxidative degradation of solvents hinder its ubiquitous use.⁸⁵

To overcome these obstacles, solid porous materials such as zeolites,^{88, 89} metal-organic frameworks (MOFs),⁹⁰⁻⁹² porous carbon and etc. are proposed as alternatives. Since these materials are basically based on physisorption, they possess exceptionally fast kinetics. Furthermore, low regeneration energy is acquired because of the absence of plenty of water.⁸⁶ Among them, especially porous carbon can be one of the strongest candidate due to its excellent chemical and thermal stability, low cost and large surface area.^{93, 94} However, compared to other candidates, the interaction between porous carbon and CO₂ is normally too weak to maintain enough adsorption capacities at high temperature with good CO₂/N₂ selectivity.

Nitrogen doped porous carbon (CN) is the attractive substrate to compensate this drawback of pure carbon. At first, amine-functionalization by post-synthetic incorporation has been employed for synergetic effect of amine and porous carbon.^{86, 95} Nevertheless, not only decrease of surface areas by pores blocking but instability in regeneration step still remained which would detract from what they are trying to achieve.²⁶ Therefore, new class of direct synthesis of N doped carbon by various N-containing precursors, such as

acetonitrile, melamine and etc. have been adopted to avoid the disadvantages of this post-synthesis.^{24, 26, 27, 96-100}

Unlike post-synthetic amine functionalization based on chemisorption, the main driving force which encourage CO₂ molecules to CN is molecular interactions. Although it is still unclear which one is the most influential mechanism, it is acceptable that Lewis acid-base interaction and hydrogen bonding are involved during CO₂ capture.^{98, 101} It has been also proven that this nitrogen works as an electron donor and enhance CO₂ uptakes and CO₂/N₂ selectivity.¹⁰² However, there are several obstacles to implementation such as lack of large scale demonstration and cost-effectiveness.

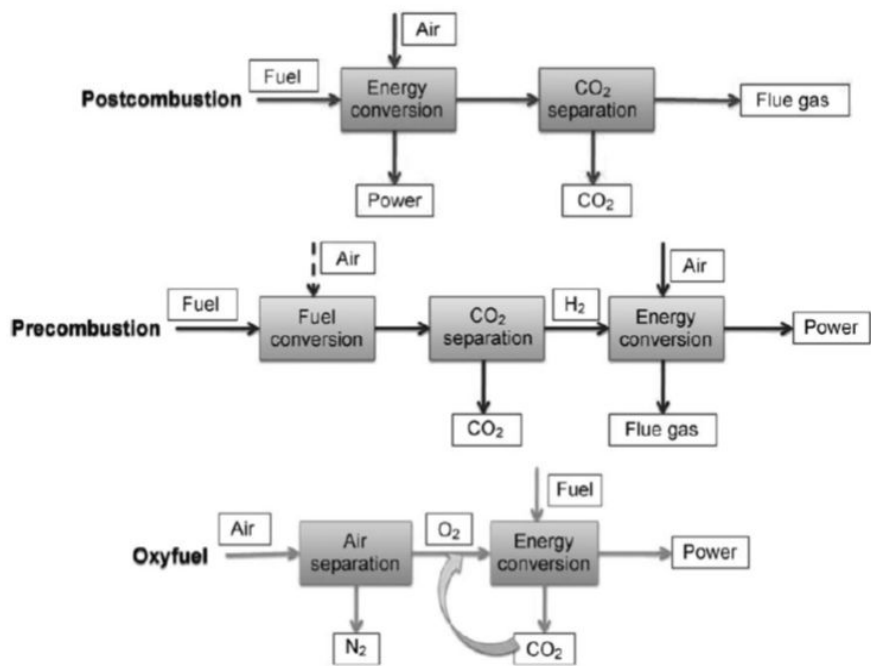


Figure 7. Post-, Pre- and oxyfuel combustion process reprinted from [85].

1. 3. Aim of the work

In this thesis, we demonstrate the possibility of compositional extension using selective etching of chlorination with an in-depth study of their origin of formation. The focus is on the adjacent atoms of carbon, boron and nitrogen. Although researches on the synthesis of composites of C, N and B have been vigorously proceeded as shown before, it is still much far behind than which have done in field of carbonous materials include form of mono-sheet and nanotubes. Especially, the role of doping of B or N in carbonous materials and the driving force of their formation are still unclear and only a superficial perception for various applications are pointed out. By synthesizing BNs and CNBs separately with a theoretical consideration, we tried to give a new insight for them.

After then, gas sorption properties of H₂ and CO₂ are evaluated. C-N-B substrates are potential materials for various gas storage because of the light weighted body. For those, we estimated both gases adsorption properties in heterogeneous materials compared to other pure carbonous one. In addition to the experiments, Density functional theory (DFT) calculations are conducted along to find out the origin of formation and the optimistic structure of gas capture.

2. Experimental Procedure

2. 1. Synthesis of porous materials

2. 1. 1. Synthesis of porous BN

Figure 7 shows the summariness of synthetic environments. TiB_2 (Aldrich) and TiN (Aldrich) powders were mixed by high energy ball milling. Since this process is conducted by direct surface reaction, the extent of mixing significantly affects the quantity of product. For the least contamination, YSZ ball and zirconia jar were used at 200rpm for 20h. The experimental procedure was followed by usual CDC experiment. The starting material (2g; TiB_2 : TiN =1:2 molar ratio for the BN stoichiometry) was placed in the quartz boat and injected into the quartz tube of the furnace. Then the furnace is heated to the desired temperature (500~800°C) under argon purge. When the temperature was reached, chlorination was performed under chlorine with a 10sccm for 3h. To remove unreactive or chemically adsorbed chlorine trapped in pore, hydrogen annealing was also performed at 600°C for 2h. Assumed that Titanium and Chlorine is fully removed (According to XPS analysis, it seems reasonable except BN-500), the product yield was around 60~65%.

2. 1. 2. Synthesis of porous CNB

CNs were synthesized based on our previous reported method as follows. A quartz boat containing 2 g $\text{Ti}(\text{C}_x\text{N}_y)$ (Treibacher Industry AG) was placed in a quartz tube furnace under flowing argon. The furnace was heated to 800 °C at 10 °C/min, after which the argon was replaced by chlorine and maintained under these conditions for 3 h. After chlorination, argon gas was fed into the system again and the furnace was cooled to 600 °C. Further heat treatment was performed at 600 °C in a hydrogen atmosphere for 2 h to remove residual chlorine trapped in the pores. BCNs were synthesized in the same way but with the addition of a boron precursor. $\text{Ti}(\text{C}_x\text{N}_y)$ and TiB_2 were mixed by hand in a mortar jar for 15 min before the heat treatment was repeated. The mixing molar ratio of carbon to boron in the precursors was 4:1 for all the CNB samples.

2. 1. 3. Chemical activation of porous CNB

The post-treatment of CNBs by KOH works as follows. Each CNB is physically mixed with KOH in mortar jar for 15min at the weight ratio of 1:2. Then it was inserted in a quartz furnace again under nitrogen atmosphere. After the purging process, conducted by 1000sccm of N_2 for 30min, heat treatment was proceeded to 600°C with 3°C/min heating ratio. The product is naturally cooled to room temperature and then washed by 2N HCl solution and distilled water several times.

2. 2. Characterization

2. 2. 1. Characterization of porous BN

XRD diffraction patterns were analyzed by M18XHF-SRA (Macscience, Japan) using Cu-K α . XPS (X-ray Photoelectron Spectroscopy) was performed using AXIS-NOVA (Kratos. Inc., UK) with monochromatic Al-K α at the 3.0×10^{-9} Torr (Figure S1). Elemental analysis was also done by XPS instrument to confirm the residues like titanium and chlorine (Table S1). Field-emission scanning electron microscope (FE-SEM) instrument, JSM-6330F (JEOL), was used for morphology analysis and depicted in Figure S2. N₂ adsorption was measured at 77K on a BELSORP-mini II (BEL Japan Inc., Japan) after degassing under vacuum at 300°C for 20h. Specific surface area was estimated by BET (Brunauer-Emmett-Teller) equation with the 0.01-0.10 relative pressure range. 0.6~0.7nm size pore, optimum size for hydrogen storage², were well developed in BN-600, BN-700, and BN-800 as shown in Figure S3 (MP-plot method). Low pressure H₂ uptake was also measured by BELSORP-mini II (BEL Japan Inc., Japan) after degassing under vacuum at 300°C for 20h with 77K, 87K both.

2. 2. 2. Characterization of porous CNB

N₂ and CO₂ adsorption were measured using a BELSORP-mini (BEL JAPAN INC., Japan) at 298 K. Before the gas adsorption, pre-heat treatment was conducted for 24 h at 300 °C under vacuum to remove residual water and other physically adsorbed impurities. The specific surface area of each sample was determined using the BET equation based on 77 K N₂ adsorption from 0.01 atm to 0.15 atm. The CO₂/N₂ selectivity was obtained using the IAST from the single component gas sorption properties, measured at the same temperature (298 K). The modified IAST was used after fitting using the single-site Langmuir model. Details are provided in the supporting information. X-ray diffraction (XRD) spectra were obtained using a Rigaku X-ray diffractometer (D-MAX2500-PC) with Cu-K α radiation. XPS was carried out using an ASIS-Hsi (KRATOS, UK) with Mg in Mg/Al dual anode source. A binding energy of 284.5 eV was selected as a reference for C 1s. The bulk boron content was measured by ICP-AES (PerkinElmer Inc., Optima-4300 DV) and C, N, and O were determined by EA (Thermo Scientific, Flash2000). Morphological studies were conducted by FE-SEM (Hitachi, SU70, 5 kV) and TEM was conducted using a Tecnai F20 (FEI, 200 kV). EELS and the corresponding elemental mapping were also conducted using a Tecnai F20.

2. 3. Calculation details

2. 3. 1. Aluminum doped BN for hydrogen storage

We used the CASTEP code, along with the generalized-gradient approximation (GGA) for the exchange-correlation potential in the Perdew-Burke-Ernzerhof (PBE) version. The Plane-wave cutoff energy is set at 330eV, and K-point sampling is used. The convergence tolerance was 5.0×10^{-6} eV per atom. The interactions between the ions and electrons are described by the Vanderbilt ultrasoft pseudopotentials. To prevent mutual interaction between atoms in the different sheets, 9×9 layer (128 atoms) was introduced with 15 Å vacuum slab.

2. 3. 2. Formation energy of nitrogen functional group in graphene

The CASTEP code was used to optimize the boron- or nitrogen-doped graphene monolayer. To prevent mutual interaction between the guest atoms, a 9×9 layer super-cell (128 atoms) was introduced with a 15 Å vacuum slab. The ultrasoft pseudo-potential with spin-polarized generalized gradient approximation Perdew–Burke–Ernzerhof (GGA-PBE) functional was used to optimize the geometry. The cut-off energy was set at 330 eV, and the convergence tolerance was 5.0×10^{-6} eV/atom.

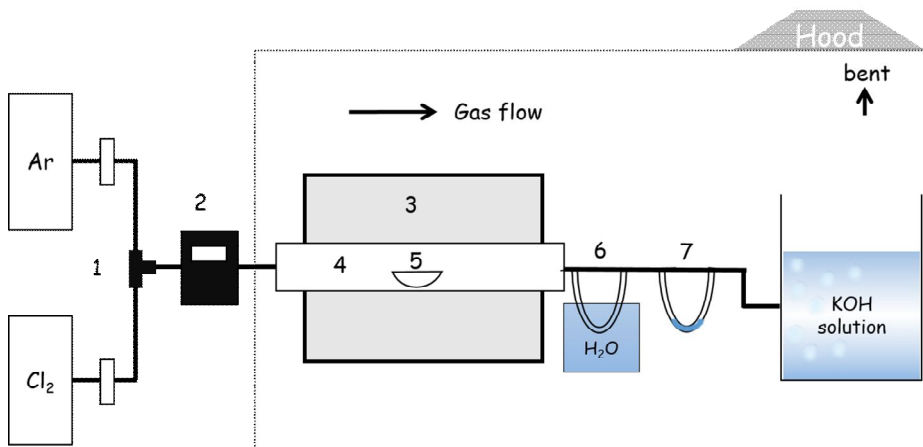


Figure 8 . Schematic diagram of chlorination procedure.

3. Results and discussion

3. 1. Porous BN

3. 1. 1. Synthesis of porous BN

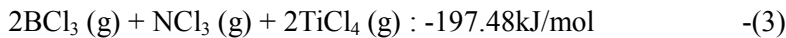
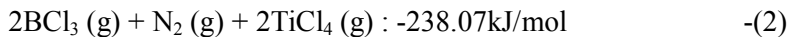
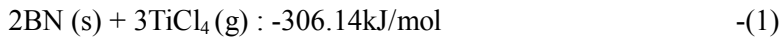
At first, solo reactions of TiB₂ and TiN each with chlorine gas were conducted for the comparison. According to them, the reaction between TiB₂ and Cl₂ gas only occurs over around 300°C. On the other hands, TiN readily react with Cl₂ even at 200°C. After the reaction, nothing was left because all of the product were existed as a gas phase such as TiCl₄, BCl₃ for TiB₂ and N₂ for TiN. The activation E (E_a) of each reactant is also evaluated by Arrhenius equation as follows.

$$k = \exp (-E_a/RT)$$

The temperature range for evaluation is from 200°C to 600°C and every experiments are repeated two times. Each data is plotted to ln(k) versus 1/T and shows the E_a of 6.15, 6.40 kJ/mol for TiN, TiB₂ respectively. It means that chlorination of TiN and TiB₂ occurs without any large energy barrier.

The reaction process of chlorination of TiB₂, TiN mixed powder may be expressed as follows (Figure 9(b)). This method is widely applied to the synthesis of microporous carbon, called carbide-derived-carbon (CDC) (figure

9(a)).^{2, 3, 6} Here, TiB₂ and TiN were used as precursors instead of metal carbides. The titanium in these compounds is easily removed by reaction with chlorine gas, yielding titanium tetrachloride (TiCl₄). However, unlike carbon, which is stable under chlorine atmospheres above 400°C, boron and nitrogen are very unstable and readily react as shown before. Actually, there are several reaction paths that this mixture is going to be as follows including desirable BN materials.



The reaction enthalpy is calculated based on JANAF data per 1 mole of chlorine gas. If reaction occurs as equation 2 or 3, there are no solid product as it did when they are solely reacted with chlorine. However equation 1 is thermodynamically the most stable, the main reaction tends to follow it. Figure 10 also shows the change of Gibbs E for reaction per 1 mole of chlorine. The negative sign means that BN will be spontaneously synthesized at our operation temperature (500–800°C).

During the course of the boron–nitrogen reaction, the continuous extraction of the large TiCl₄ molecules from the solid material enables pore development and results in a high-surface area turbostratic BN. The BN powders are referred to here as BN-T, where T indicates the chlorination temperature.

Figure 11 shows the XRD patterns for each BN. Two large diffraction peaks at (002) and (10) were observed in all samples, corresponding to turbostratic BN also confirmed by the XPS spectra (Figure 12). (The B 1s and N 1s peak positions, i.e. 190.9 eV, 397.8 eV, respectively, were comparable to those reported previously.^{103, 104} EELS analysis is also adopted for BN-600 to figure out the composition and its structure more precisely (Figure 13). That spectra shows that K-shell excitations of boron, carbon and nitrogen are well presented. The sp^2 bonding character of B-N is identified by the sharp π^* -peaks on the right and the broad σ^* -peaks at left in the vicinity of 190eV and 400eV, which stands for boron and nitrogen, respectively. While the peaks around 280~290eV indicates that carbon contamination works after the porous BN is exposed to air.

Since BN is structurally similar to carbonous materials, the relative amorphous character of BN can be extrapolated from XRD patterns.¹⁰⁵ Among the samples, BN-600 displayed a more amorphous character than others. As the temperature increased beyond 600°C, the degree of crystallization increased. However, at 500°C, it didn't follow that behavior. It seems that chlorine, not easily released at low temperature, may have chemically adsorbed and stabilized the BN structure. XPS elemental analysis proves that BN-500, a contrast to other samples, possesses significant chlorine amount of 5.6wt%. The Field emission scanning electron microscope (FE-SEM) images also show the different morphology character of BN-500 (Figure 14). Other samples have well developed porous features compared to BN-500.

The nitrogen adsorption isotherms supported the structural trend observed in the XRD patterns and is shown in figure 15. According to IUPAC classification, BN-500 yielded a type IV isotherm with a large hysteresis loop due to chlorine trapping, whereas BN-600–BN-800 exhibited both type I and type IV components in the isotherm. The BN-600–BN-800 samples possessed micropores and mesopores simultaneously. The pore properties of all BN samples are summarized in Table 1. Specific surface areas calculated in the relative pressure (here range from 0.01 to 0.1) showed that the modified Brunauer-Emmett-Teller (BET) specific area was up to $960\text{m}^2/\text{g}$. For more details, micropore and mesopore volumes were calculated according to MP-plot and Barret-Joyner-Halenda (BJH) methods, respectively. The micropore size distribution analysis based on MP-plot method is shown in Figure 16. BN-600 showed the highest specific area with a large micropore volume ($0.38\text{cm}^3/\text{g}$).

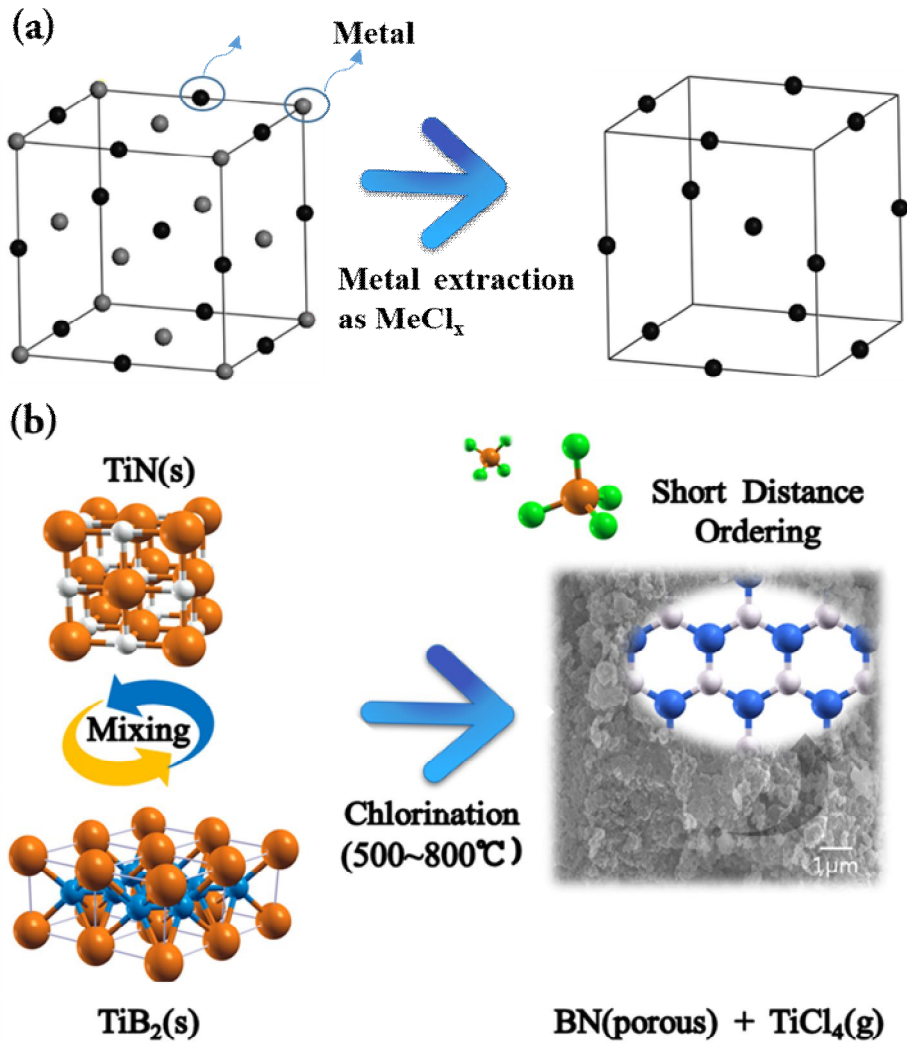


Figure 9. Schematic diagram of typical carbide derived carbon method (a) and our developed ceramic derived boron nitride method (b) (Colored online).

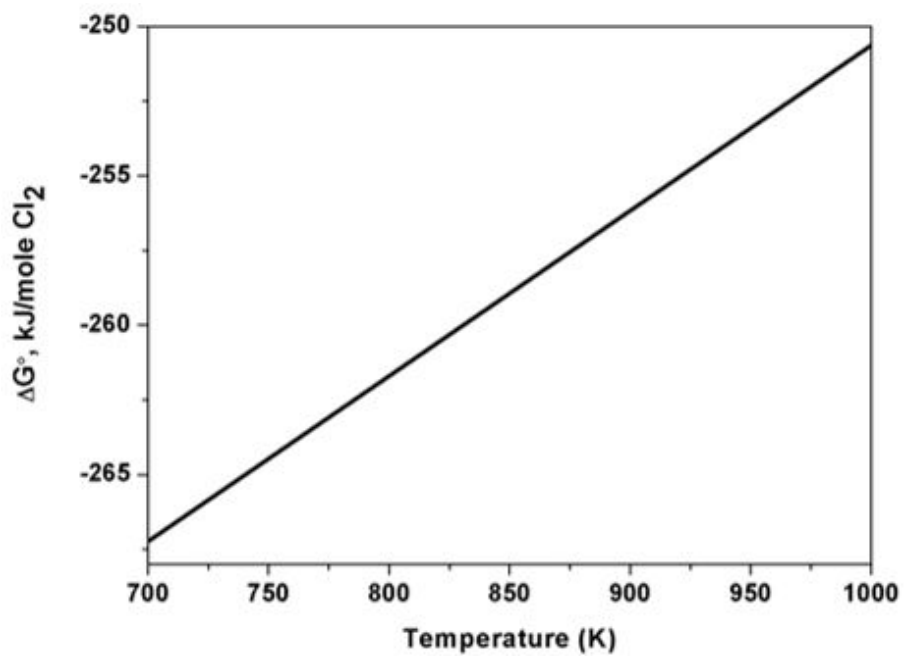


Figure 10. Change of Gibbs free reaction energy of following equation:
 $\text{TiB}_2(\text{s}) + 2\text{TiN}(\text{s}) + 6\text{Cl}_2(\text{g}) = 2\text{BN}(\text{s}) + 3\text{TiCl}_4(\text{g})$.

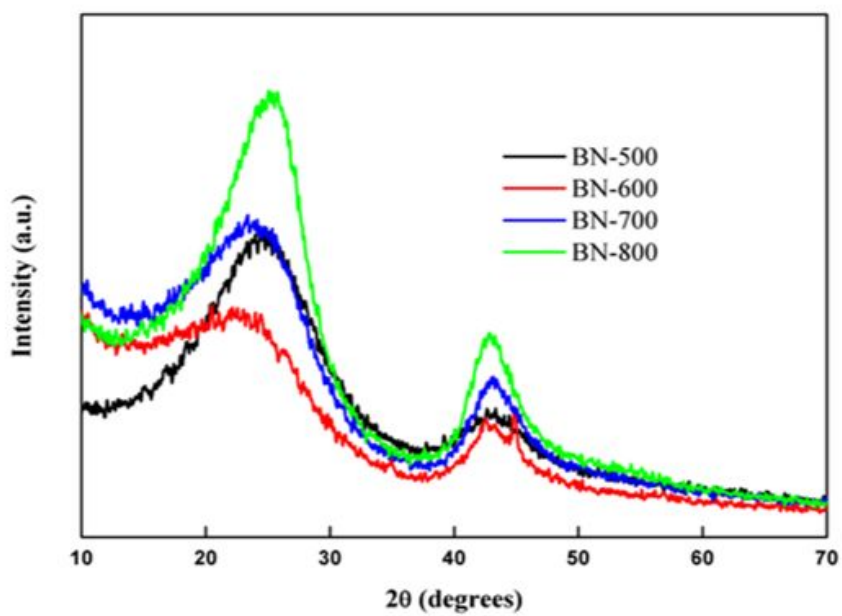


Figure 11. XRD diffraction patterns of synthesized BNs.

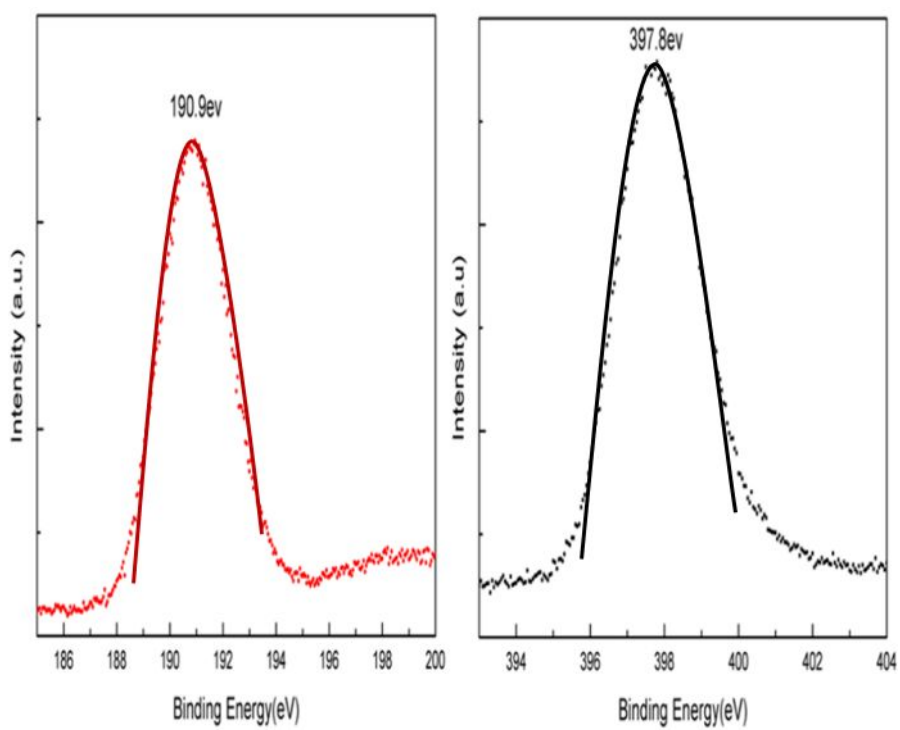


Figure 12. B 1s (left) and N 1s (right) XPS spectra of BN-600.

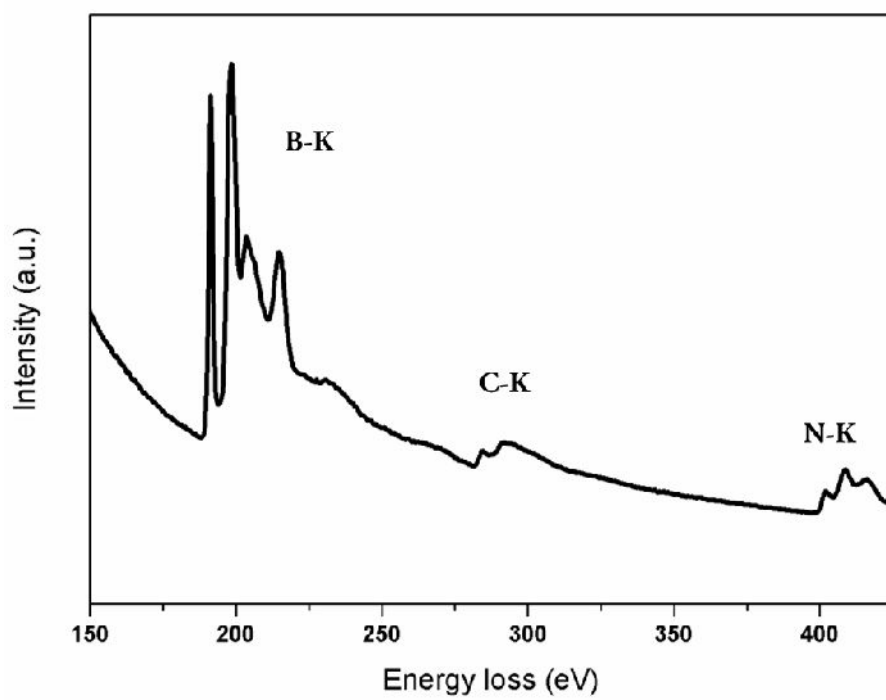


Figure 13. EELS spectra of BN-600.

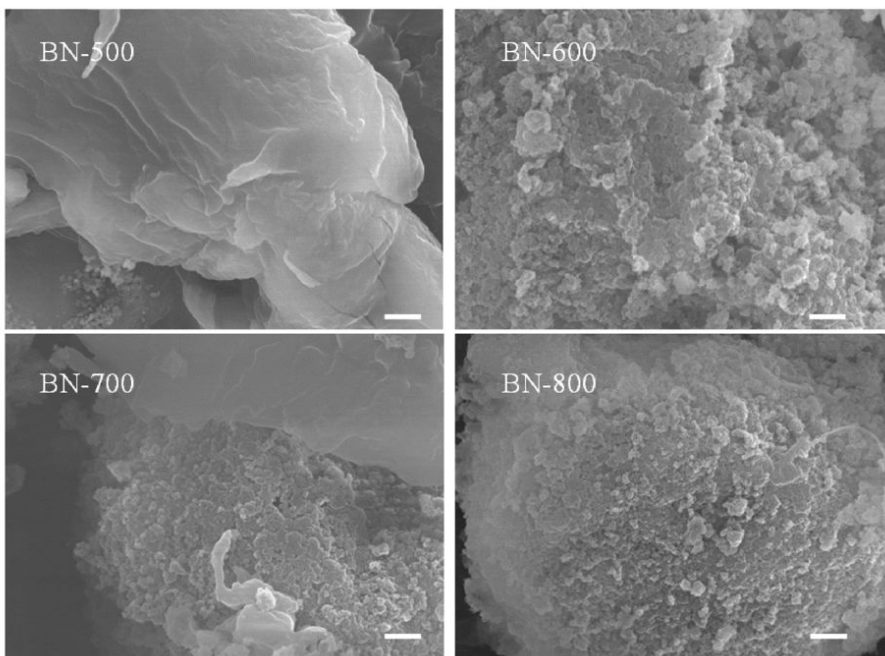


Figure 14. FE-SEM images of BN series (scale bar: 0.2 μ m).

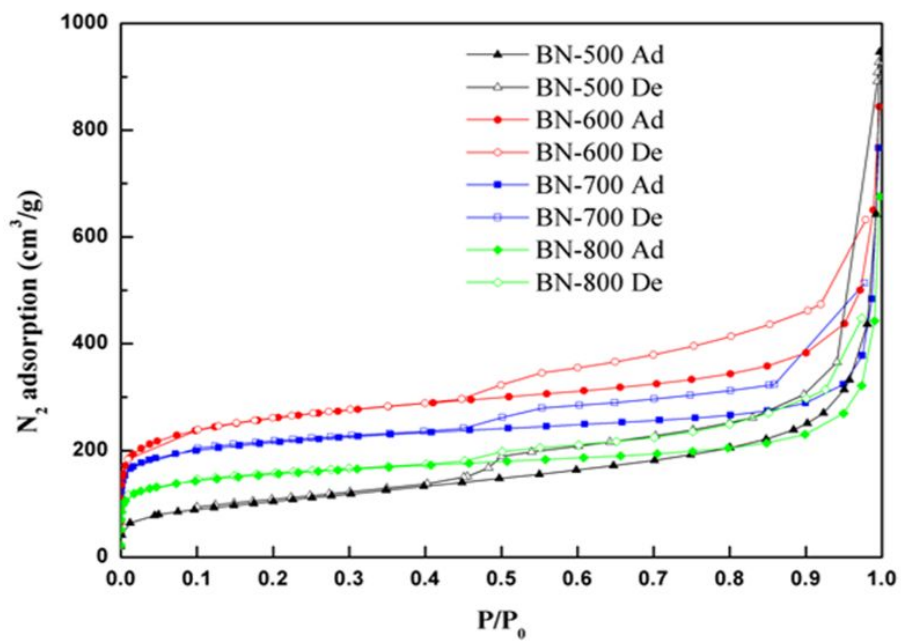


Figure 15. 77K N₂ isotherms of the BN samples. Closed symbols represent adsorption and open symbols represent desorption.

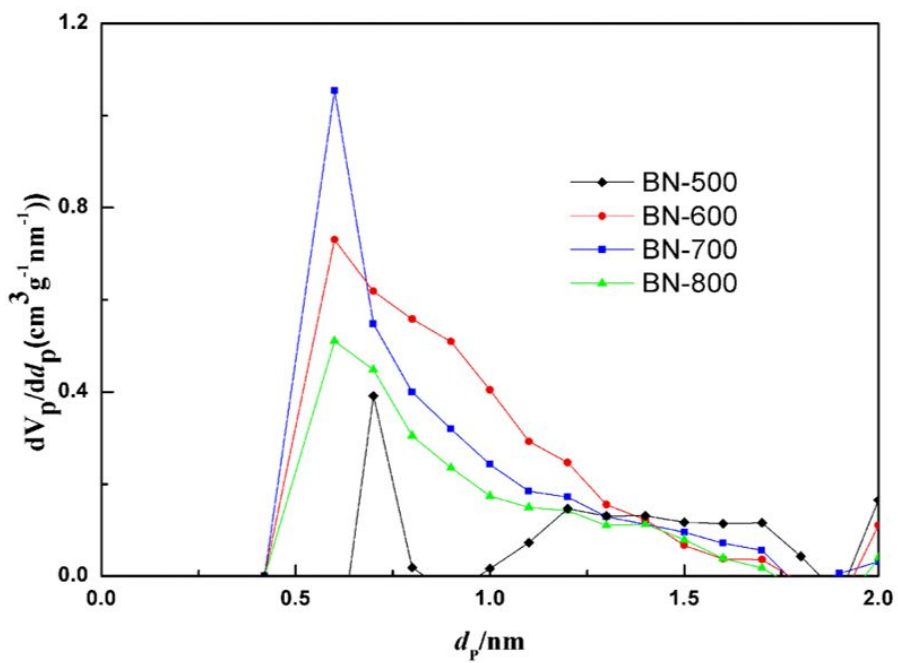


Figure 16. Micropore size distribution of BN series based on MP-plot method (Colored online).

Chlorination Temperature (°C)	Surface area (m²/g)^a	Total pore volume (cm³/g)^b	Micropore volume (cm³/g)^c	Mesopore volume (cm³/g)^d	Micropore size (nm)^e
500	334	0.48	0.14	0.34	0.7
600	960	0.68	0.38	0.28	0.6
700	796	0.50	0.31	0.18	0.6
800	570	0.42	0.22	0.18	0.6

Table 1. Pore properties of the BN samples as a function of chlorination treatment temperature. ^a Surface area was measured using the BET method. ^b The total pore volume was measured up to P/P₀=0.95. ^c Micropore volumes were estimated using the MP-plot method. ^d Mesopore volumes were estimated using the BJH method (adsorption branch between 0.3 < P/P₀ < 0.95). ^e Max of micropore diameter was estimated using the MP-plot method.

3. 1. 2. Hydrogen storage of porous BN

The hydrogen adsorption properties were also measured to test the utility of the BN-600 sample's high microporosity. Figure 17 provides the low-pressure hydrogen uptake properties of other BN samples at 77 K. As the surface area decreases, the H₂ uptake amounts are also decreased and these trend is in common for H₂ physisorption. Measurements were repeated at 77 K and 87 K to estimate the heat of adsorption (Q_{st}) for H₂, as shown in Figure 18. Hydrogen was stored up to a level of 1.01 wt% at 77 K and at ambient pressures, and storage was fully reversible, consistent with the properties of physisorption. Q_{st} depends on the surface coverage (θ) and was estimated using the Clausius–Clapeyron equation with Langmuir–Freundlich fitting as follows.

$$Q_{st} = -R \left[\frac{\partial \ln(P)}{\partial (1/T)} \right]_{\theta}$$

Where R means the gas constant, P the pressure and T the temperature. From the plotted line of ln(P) vs. 1/T (T for 77K, 87K), we can get the slope of the line used to get the Q_{st} at each pressure point.

Langmuir-Freundlich fit for the isotherms was used to determine Pressure as a function of the amount of H₂ adsorbed.

$$\frac{M}{M_{\max}} = \frac{A \times P^{\left(\frac{1}{t}\right)}}{1 + A \times P^{\left(\frac{1}{t}\right)}}$$

Where, M means absorbed moles of hydrogen, M_{\max} the moles adsorbed at saturation, P the pressure, A and t the constant, respectively. All of the determined values of BN-600 based on these equations are listed in this table 2.

BN-600 exhibited a high Q_{st} of 12 kJ/mol at low coverage, and this value decreased as the hydrogen uptake increased. It is higher than other well-known carbonous materials as expected except TiC-CDC800. Generally, Q_{st} of carbonous materials, i.e., activated carbon (AC) and single wall carbon nanotube (SWCNT), are around 4~5kJ/mol and it is in the range of van der waals forces. Since TiC-CDC800 shows very narrow pore size distribution (PSD) around 0.6~0.7nm, known as optimum size for effective hydrogen storage, it causes some exception.

The trend changed once Q_{st} reached a value of 7 kJ/mol, and then reversed with a slight increase.³ Even better Q_{st} than TiC-CDC800 at higher coverage occurs in consequence of this reverse. It is still unclear to identify the reason of this phenomenon, the interactions between the hydrogen molecules polarized by the adsorbent surface could potentially have resulted in this rise.^{91, 106} This behavior is unfamiliar to general hydrogen physisorption materials.^{3, 107}

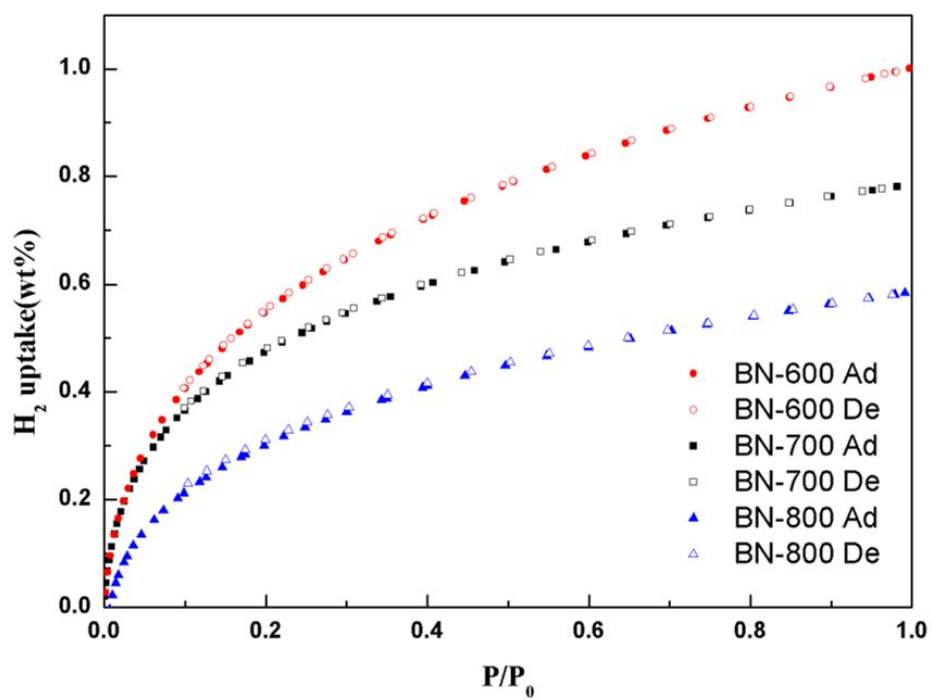


Figure 17. Low-pressure hydrogen uptake properties of BN series at 77K. Closed symbols for adsorption and open symbols for desorption.

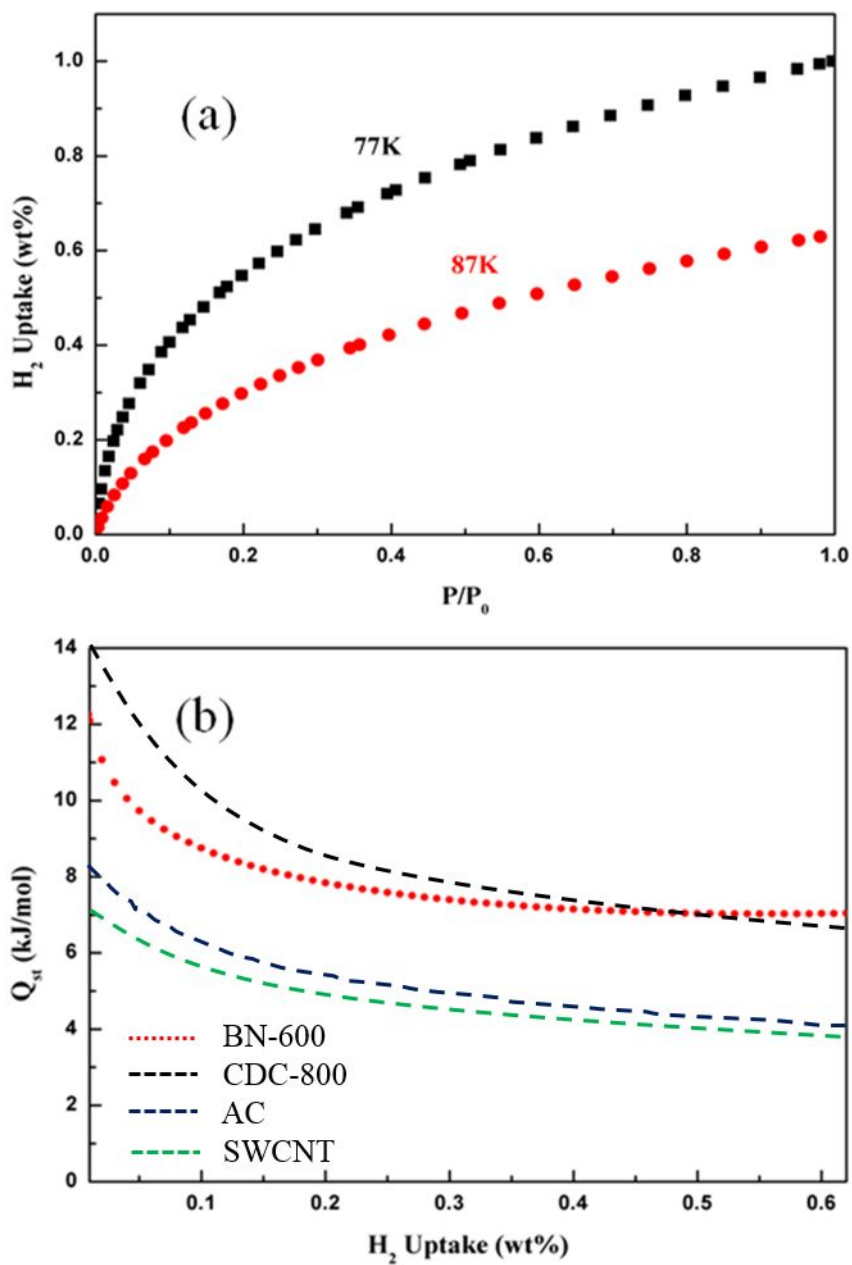


Figure 18. Hydrogen adsorption uptake of BN-600 at low pressures (a). Black for 77K, red for 87K, respectively. Heat of adsorption (Q_{st}) of BN-600, CDC-800 and activated carbon (AC) and single wall carbon nanotube (SWCNT) as a function of the hydrogen uptake (b).

H₂ (wt%)	uptake Q_{st} (kJ/mol)	H₂ (wt%)	uptake Q_{st} (kJ/mol)
0.01	12.0998	0.32	7.33183
0.02	11.06989	0.33	7.30359
0.03	10.47221	0.34	7.27703
0.04	10.05161	0.35	7.25207
0.05	9.7281	0.36	7.22866
0.06	9.46608	0.37	7.20672
0.07	9.24655	0.38	7.18621
0.08	9.05816	0.39	7.16707
0.09	8.89361	0.4	7.14926
0.1	8.7479	0.41	7.13274
0.11	8.61748	0.42	7.11746
0.12	8.49971	0.43	7.10341
0.13	8.39261	0.44	7.09054
0.14	8.29462	0.45	7.07883
0.15	8.20452	0.46	7.06825
0.16	8.12131	0.47	7.05879
0.17	8.0442	0.48	7.05041
0.18	7.97251	0.49	7.0431
0.19	7.90568	0.5	7.03685
0.2	7.84324	0.51	7.03164
0.21	7.78479	0.52	7.02746
0.22	7.72999	0.53	7.0243
0.23	7.67853	0.54	7.02215
0.24	7.63015	0.55	7.02099
0.25	7.58463	0.56	7.02083
0.26	7.54178	0.57	7.02166
0.27	7.5014	0.58	7.02348
0.28	7.46335	0.59	7.02628
0.29	7.42748	0.6	7.03007
0.3	7.39368	0.61	7.03484
0.31	7.36183	0.62	7.04059
		0.63	7.04733

Table 2. Estimated values of the heat of the adsorption (Q_{st}) about BN-600 according to H₂ uptake based on Clausius-clapeyron equation and Langmuir-freundlich fitting.

3. 1. 3. Formation energy of Al- doped BN

Tried to suggest a reasonable model for hydrogen storage at moderate operating conditions, two main standards are set as follows. First, conceived structure should have large enough surface area. For this, main constituent of body should be light weighted atoms like B, C, N, O. Carbonous materials, Boron nitrides or MOFs are belong to this category.

Second, formation energy of structure should be reasonable. Even though it shows high hydrogen adsorption energy, it would be just a fictional materials if it is not stable thermodynamically. Under this criteria, not only transition metal doping, the most popular modeling for hydrogen storage, also other atoms i.e., calcium, potassium has been excluded because of their quite high cohesive energies.

We found that Al doped BN is highly satisfying prior standards as a hydrogen storage materials. Instead of dispersion of doping atom, substitution method is used to avoid the atom clustering. It shows enough hydrogen binding energy which involves curvature increases.

Figure 19 shows the geometrical configuration of Al doped BN sheet. The formation E of this sheet is calculated based on following equation.

$$E_{\text{form}} = E_{\text{total}}(\text{Al doped BN sheet}) - E_{\text{total}}(\text{BN sheet}) + \mu_{\text{B}} - \mu_{\text{Al}}$$

Where, E_{total} means the total energy of the system and μ_{x} means the chemical potential of x. In case of μ_{Al} , α -Al is used stationary. Minus sign means the

reaction occurs spontaneously and plus sign vice versa. As shown in table 3, Formation E is decreased as the energy of boron sources is increased. Especially, BCl_3 , the highest energy of boron source evaluated in this calculation, show negative formation E. Therefore energetically stable Al doped BN can be synthesized depending on the source of precursor.

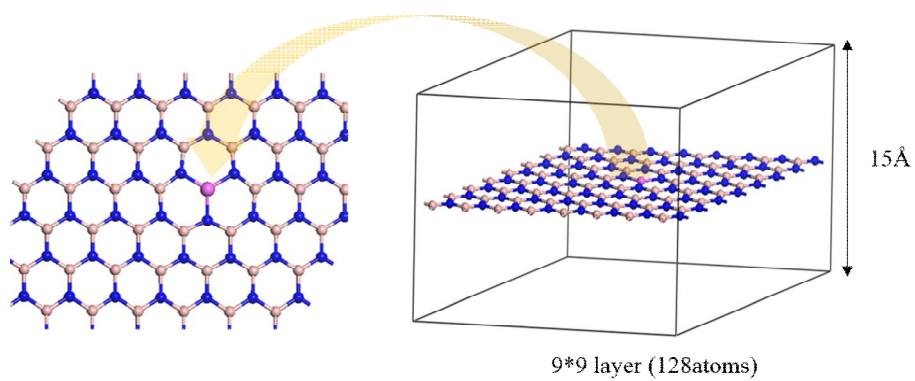


Figure 19. Geometrical configuration of Al doped BN sheet.

	α -B	BH ₃	B ₂ H ₄	BCl ₃
E _{form} (Al doped)	2.53	3.49	3.8	-0.39

Table 3. Formation energy of Aluminum substitution for boron in BN sheet according to various boron sources.

3. 1. 4. Hydrogen adsorption properties of Al-doped BN

After boron is substituted to aluminum, there are no any big structural changes compared to pristine BN-sheet since Al possesses similar atomic radius with same number of valence electrons. At this time, once the first hydrogen molecule adsorption, Al metal atom is protruding upward to the H₂. All details of optimized structure is present in Figure 20. The original AlN structure is wurtzite, Al atom is 4 fold coordinated to nitrogen atoms. However when Al is doped in BN structure, it could only possess 3 nitrogen per each. Since the electronegativity of Al (1.61) is smaller than primitive B (2.04), induction force to N become stronger after substitution. This difference induced the charge redistribution and caused the strong interaction with H₂ molecules. It was already demonstrated that 3-fold AlN also shows its potential as hydrogen storage materials. The calculated first binding energy (E_{ads}) is 0.80eV with a hydrogen bonding elongation. (From 0.752Å to 0.764Å) However, the significant increase of binding energy could not be explained just by this electrostatic forces.⁷³ Since the low lying vacant valence orbitals of Al³⁺ is symmetrically available, the favorable mixing between them and hydrogen σ -bonding orbital is highly expected. We will discuss this with DOS (Density of States) later.

Actually, the protrusion of doped metal and accompanying increase of H₂ adsorption E (E_{ads}) is not a unique issue. Similar results are already reported

and discussed several times as above mentioned mechanism. However, after the second H_2 molecule adsorption, strange structure reconstruction is happened and curvature is reversed opposite to H_2 molecules as shown in figure 21. This shape resemble two magnets with the opposite poles facing each other and seems like no more significant interactions between them. In general, if there is no more room for new H_2 molecule, it leave as itself from the substrate without causing any transformation of already formed dihydrogen.

And surprisingly, although curvature is reversed, this Al doped BN show enough E_{ads} after several H_2 molecule adsorption. The distance of around 3.3\AA from Al to H_2 molecules are too far to anticipate direct interaction. The average E_{ads} and related structural factors are summarized in table 4. As number of adsorbed H_2 molecule increases, E_{ads} decreases reversely. However, even after 7th H_2 adsorption, it is kept over 0.1ev. This maintained average biding E is very unfamiliar. Generally, when H_2 molecules are move away from the substrate, the adsorption E become lower in range of the van der waals force.⁷⁰ Nevertheless, Al doped BN is reliable to work under moderate condition even after several H_2 adsorption as the angle of N-Al-N of it become closer to original AlN wurtzite structure.

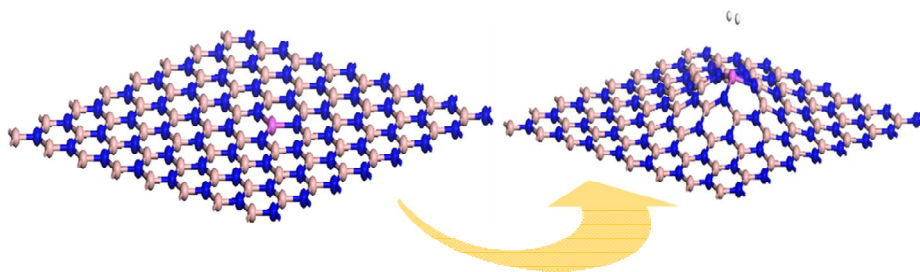


Figure 20. Geometrical optimization of Al-doped BN sheet after first hydrogen molecule adsorption.

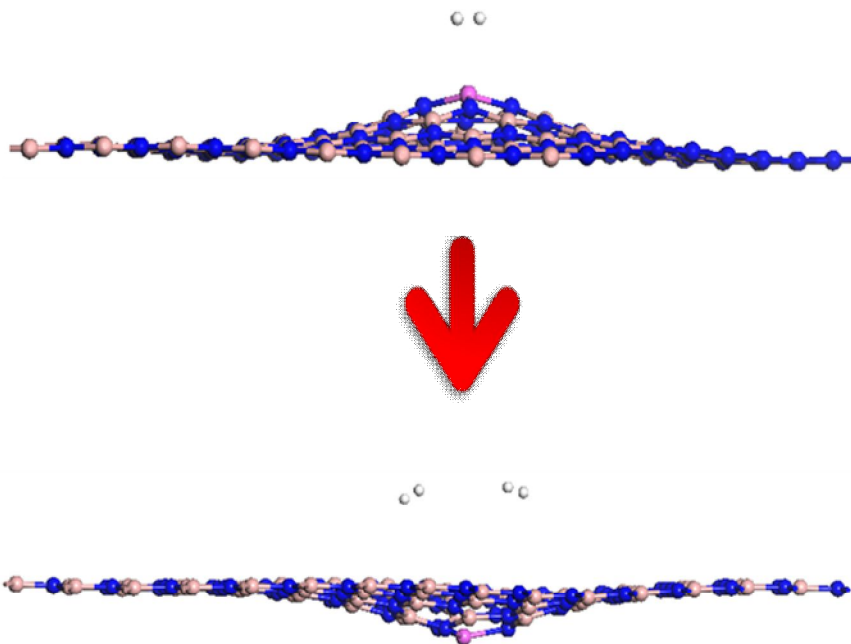


Figure 21. Geometrical difference between first and second hydrogen molecule adsorption on Al- doped BN sheet.

	1H ₂	2H ₂	3H ₂	4H ₂	5H ₂	6H ₂	7H ₂
Average H ₂ binding E(ev)	0.80	0.35	0.23	0.18	0.14	0.13	0.12
H-H (Å)	0.764	0.753	0.753	0.753	0.753	0.753	0.753
∠N-Al-N(°)	115.85	117.21	117.14	117.11	117.10	117.09	117.06

Table 4. The average hydrogen binding energy and related structural factors of Al- doped BN sheet.

3. 1. 5. Density of states (DOS) investigation of Al-doped BN

To find out the origins of its unique H₂ adsorption, density of states (DOS) are plotted for each states and depicted as figure 22. After first H₂ adsorption, the σ -bond of H₂ is shifted by -2.5ev to that of free states which means the stabilization of electrons. The significant interaction between H-s orbitals and Al-p orbitals induce the sp-hybridization and in correspondence to this change. Furthermore, unoccupied Al-p orbitals are appeared at around 5ev as a level repulsion proof. These overall evidence indicates that H₂ molecule is strongly bound to Al doped BN.

Then after second H₂ adsorption, the σ -bond of H₂ is back shifted to the original states as if there are no interactions anymore. However, orbital splitting is occurred at the part of Al-p orbitals as explained by ligand field theory. That is, some of the unoccupied Al-p orbitals, composed of p_x and p_y mainly, around 5ev are shifted positively to 4ev. The still remained part of Al-p orbitals at 5ev indicates that the reduction of the total energy is still works. This maintaining level repulsion is the proof of interaction between H₂ molecules and Al doped BN. The similar result, called electron-donation mechanism, has been already demonstrated when CO₂ is physisorbed on Boron rich Boron-Nitride Nanotubes.¹⁰⁸ As the amounts of adsorbed H₂ molecules increases, these repellent portion inversely decreases as shown in figure 23 and it is well agreed with decrease of average H₂ binding energies.

For the comparison, we further conducted H₂ molecules interaction with Nickel (Ni)-doped BN as shown in figure 24. The geometrical transformation after first H₂ adsorption is very similar to Al-doped BN and protrusion of Ni occurs toward to the H₂ molecule. Contrast to Al-doped BN, this change is maintained even after second and third H₂ molecule adsorption. The meaningful interaction just works until second H₂ molecule with an average binding E of 0.37eV (figure 24 (a)). On the other hands, third one is no more adsorbed and exist as a free state without any influences to former adsorbed H₂ molecules as shown in DOS of figure 24 (b).

To judge the possibility of further enhancement, we substituted two B atoms to Al atoms in the same sheet and five H₂ molecules are arranged per each Al as depicted in figure 25. When H₂ molecules are putted on the same side (figure 25 (a)), the average binding E is 0.14eV and it is exactly the same with calculated parameter in single Al doped BN. However, after loading of H₂ molecules at the opposite side of each Al, it is changed to 0.18eV, about 30% of increase (figure 25 (b)). It means that the binding energy can be further increased by geometrical consideration.

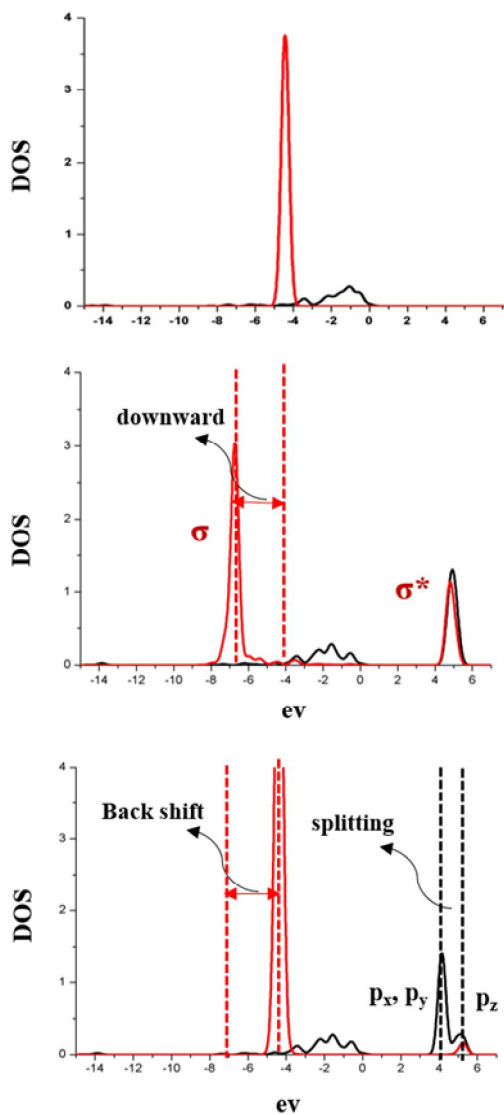


Figure 22. Change of density of states (DOS). Free hydrogen molecule with Al- doped BN sheet (up), Al- doped BN sheet after first hydrogen molecule adsorption and that after second hydrogen molecule adsorption. Red line represents PDOS of H-1s orbitals and black line represents PDOS of Al- 2p orbitals.

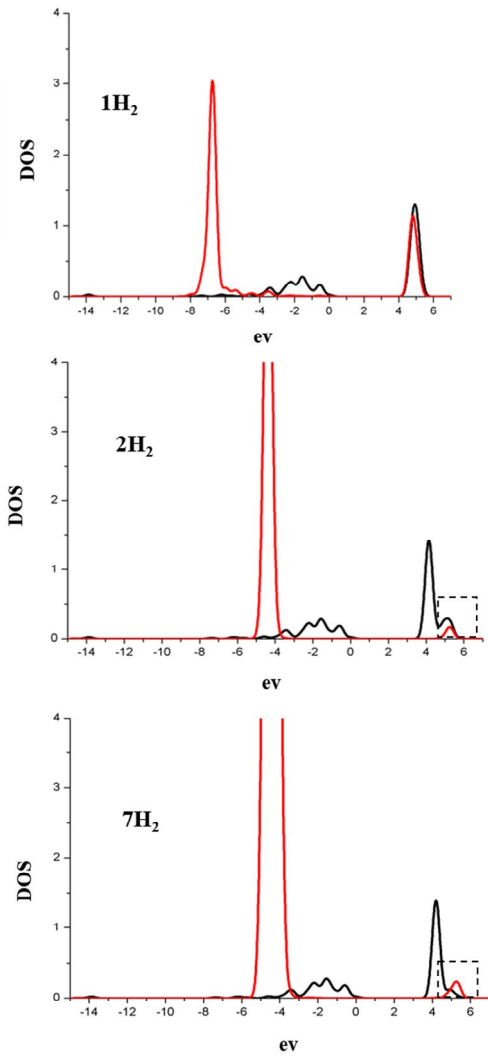


Figure 23. Change of density of states (DOS) as increase of adsorbed hydrogen molecules on Al- doped BN sheet. Dashed square means the level repulsion portion.

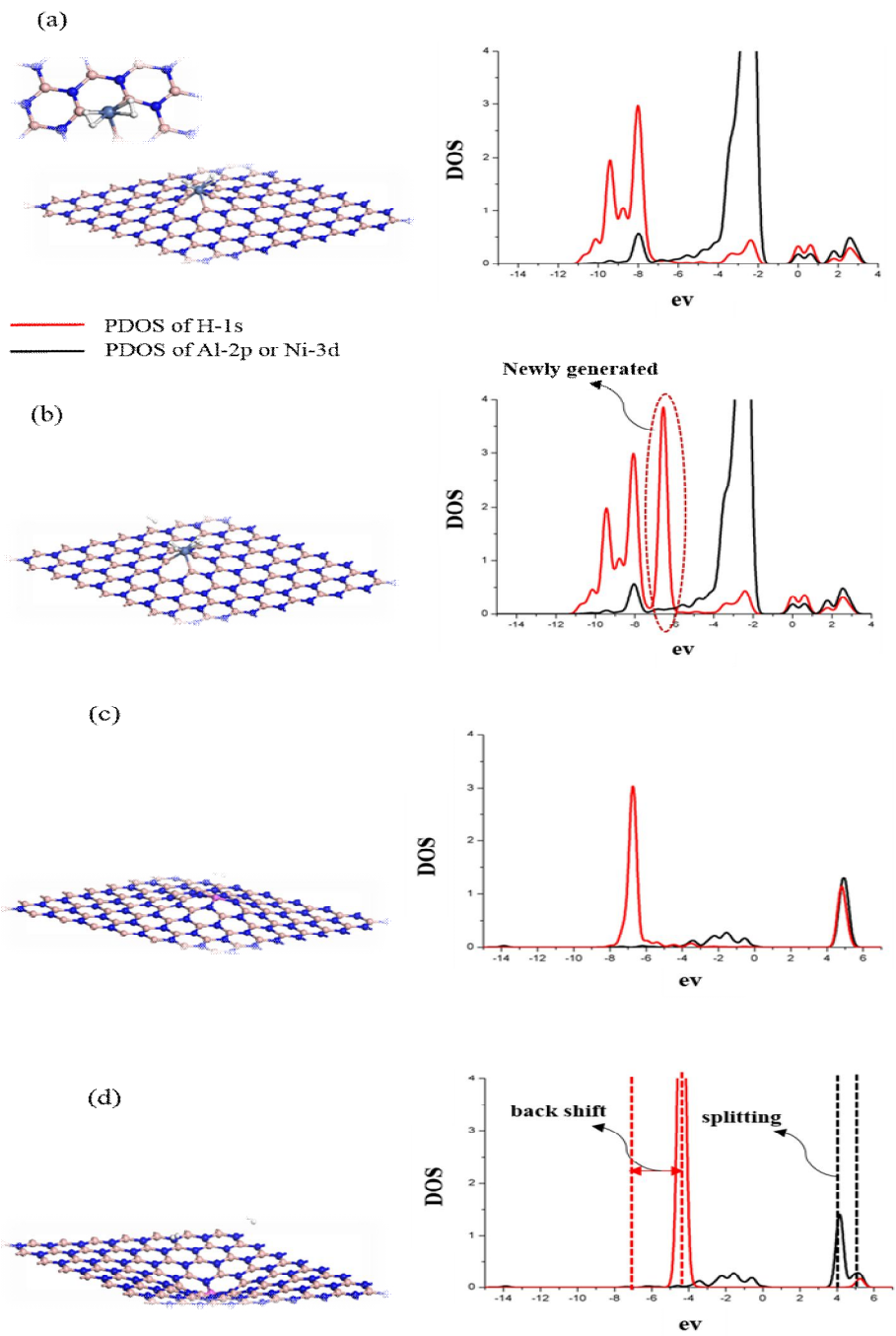
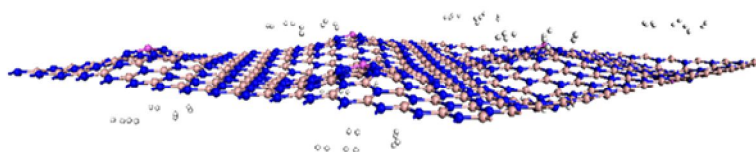


Figure 24. Geometry and DOS of Ni-doped BN sheets ((a), (b)) compared Al-doped BN sheet ((c), (d)).

(a)



(b)

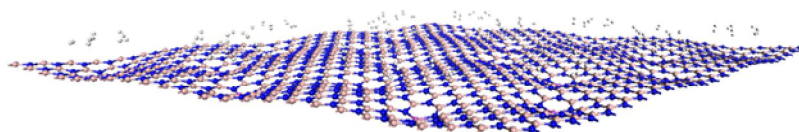


Figure 25. Geometry of two aluminum- doped BN sheet which adsorbed fifth hydrogen molecules when hydrogen adsorbed on the opposite side (a) or same side (b).

3. 1. 6. Conclusions

In summary, we present a new and simple procedure for synthesis of high surface porous BN with a large micropore volume. Synthesizing high-surface area BN (up to 960 m²/g) with large micropore volumes (0.38 cm³/g) was demonstrated. To the best of our knowledge, the reported surface areas and micropore volumes are the highest values and almost double those reported than ever reported for BN materials. The potential utility of the porous BN in hydrogen storage applications was evaluated too by measuring the isosteric heat of adsorption (Q_{st}) for H₂. Although the measured value is still far from the target ideal values of 13–15 kJ/mol, the value is one of the highest yet reported for hydrogen physisorption materials. In this situation, BN is considered as an alternative physisorption substrate with a strong surface–hydrogen interaction potential. Increasing the surface area and controlling the pore size will be the next steps toward enhancing hydrogen uptakes and enlarging the applications of this material. Judging from its unique properties as mentioned above, our results are also supportive of the further development of porous BN as catalyst supports or gas adsorbents.

First principle calculation is adopted to figure out the stability and H₂ molecule binding E. Among several candidates, Al doped BN is thermodynamically proper and shows reasonable E_{abs} at the same time. Even after the adsorption of 7th H₂ molecule, the average binding E is beyond the range of van der waals force. The geometrical preference of Al-N bond to 4-

fold configuration lead the stabilization of total structure. Even though, further research for this structure is still needed, we hope that it will trigger the doping chemistry of BN based materials for gas adsorption and storage.

3. 2. Porous CNB

3. 2. 1. Synthesis of porous CNB

Figure 26 shows the N₂ adsorption properties of CNs and CNBs at 77K. Except CN37, which behaves like a non-porous material, all samples display type I and IV pores, implying active and simultaneous development of both micro- and meso- pores. Particularly, boron addition causes a sharp increase of adsorption branch at P/P₀=0.90-0.99 with the H2 type of hysteresis loops, especially when precursors of high nitrogen contents are used. The result indicates that the size and shape of the pores are not fixed and the pore size spreads from micro to macropore regions. Detailed textural properties of the samples are summarized in Table 5. There is no significant textural difference between CN73 and CNB73 except small decrease in mesopore volume. It seems to be related with the chemical stability of precursor. Indeed, when Ti(C_{0.7}N_{0.3}) were used for CN73 as precursor, high amount of carbon ensures the stability of CN in the precursor under chlorination atmosphere, resembling normal CDC products.

In contrast, the situation is different with CN55 and CNB55. Since nitrogen functional groups are not stable enough during chlorination at high temperature, the structure of CN55 is partially collapsed because of the deficiency in neighboring carbons due to the formation of C_xN_y gas.¹⁰⁹ Thus, BET surface area are decreased by pores encroached. Pore detainment is

observed in CNB55 and becomes glaringly obvious when CN37 and CNB37 are compared each other. Since most of CN37 structure is lost as CNCl and C_xN_y gas phases,¹⁰⁹ the yield is extremely low (1.5%) and pore formation is also retarded. But, after boron addition, the yield is significantly enhanced to 18.3% with a pore development. The BET surface area is also increased dramatically from $183\text{m}^2/\text{g}$ to $730\text{m}^2/\text{g}$.

Figure 27 shows the morphologies of the CNBs, which are similar to those of $\text{Ti}(C_xN_{1-x})$ precursors. This observation is consistent with normal CDC products which provide narrow pore size distributions.^{3, 6} The increase of nitrogen content in the $\text{Ti}(C_xN_{1-x})$ precursors causes the shape change of CNBs from angular to spherical with decrease of average particle size as noted from CDCs. TEM analysis was performed for further characterization. In Figure 28, typical turbostratic images are observed from CNB73 and CNB55. Some short range ordered graphene-like layers, indicated by circles, are detected especially at the edge boundaries.

On the other hand, CNB37 is in the form of a hollow sphere (Figure 29 (b)), which is much different from that of CN37. (Figure 29 (a)) The shell thickness of the sphere is estimated 7~8nm. Two diffusive rings were obtained from selected-area electron diffraction (SAED) pattern; (100)/(101) and (110)/(112) patterns with 0.21nm and 0.12nm of d-spacing, respectively. The existence of short ordered (002) interlayers, which are observed nearly at the boundaries, confirms the turbostratic nature of CNB37. (Figure 29 (c), (d)) This character is also supported by two broad peaks in X-ray diffraction pattern as shown in Figure 30. Like a fullerene, carbon and its isotopes are

known to have a capability to construct spheroidal microstructure. Although the hollow spherical carbons^{110, 111} and boron nitrides (BN)¹⁵ without a hard template have been reported, a hollow structure of CN or CNB is rarely mentioned yet. It is because C-N bonds are unstable compared to C-C or B-N bonds, which tend to decompose easily, resulting in the structure collapse during synthesis.

The mechanism of hollow CNB formation is elucidated as shown in figure 31. The shape of $\text{Ti}(\text{C}_{0.3}\text{N}_{0.7})$ precursor is assumed as a sphere for simplicity in Scheme 1. Based on the CDC formation, the initial morphology is expected to conformal to that of $\text{Ti}(\text{C}_{0.3}\text{N}_{0.7})$ after titanium extraction by chlorination, resulting in an analogous porous structure as shown in Figure 27 (f). In this stage CNB37 of high stability is believed to form along the surfaces of $\text{Ti}(\text{C}_{0.3}\text{N}_{0.7})$ particles as shown in Figure 27 (e), which are actual interface between $\text{Ti}(\text{C}_{0.3}\text{N}_{0.7})$ and TiB_2 precursors. This is in contrary to CN37 that experiences structure collapse. Further, the interfacial areas become a shell skin, leaving a hollow structure, as the internal CN structure from $\text{Ti}(\text{C}_{0.3}\text{N}_{0.7})$ disappears as C_xN_y gas.

Not only direct interaction of boron with the surface layer but the CNB hollow surface is further stabilized by BCl_3 that are inevitably formed from the reaction between TiB_2 and Cl_2 . Since BCl_3 is a strong Lewis acid, Lewis acid-base (nitrogen functional group) interaction induces relatively lower surface energy of exterior than that of inner portions. It is similar to the hollow structure obtained from iron oxide by inorganic anions in the solution.¹¹² As a result, the shell is formed and the densification follows as the

loosely connected CNB shell gains part of C-N moieties from interior. This is well supported by the facts that the size of the hollow structure in Figure 29 (b) matches closely to those of the precursor, $\text{Ti}(\text{C}_{0.3}\text{N}_{0.7})$ in Figure 27 (e) and that the CNB37 productivity increases significantly, from 1.5% to 18.3% in weight as listed in Table 5, compared to that of CN37. Thus, we can conclude from this result that the presence of boron in CN stabilizes the C-N bonding, facilitating the formation of robust CNB hollow structure.

According to elemental mapping of CNB37, as shown in Figure 32 (a)-(c), C, N and B atoms are uniformly distributed without any segregation. Corresponding EELS is described in Figure 32 (d). Among them, two peaks of high intensity are appeared at ~ 284 and 292eV . These are related to the $1s-\pi^*$ and $1s-\sigma^*$ transitions of C K-shell excitation edges, respectively, which means the abundance of graphitic carbon.³³ Also, sp^2 bonding character of N atoms are shown as two broad peaks around 400eV .¹⁸ But there are only weak signals around 194eV , which is originated from B K-shell excitation edges and attributed to the low contents of boron. These signals are more obvious when the content of boron precursor is increased as shown in Figure 33. The figure shows two distinguished regions, i.e., C-rich and BN-rich regions and BN-rich region exhibits two clear peaks at $190\sim 195\text{eV}$. The lower peak (191eV) comes from boron bonded to carbon whereas the higher peak (194eV) is from boron bonded to nitrogen.³³

For accurate chemical compositions and their bonding nature, CNs and CNBs were analyzed by XPS and the results are summarized in Table 6. The Elemental Analysis (EA) and Inductively Coupled Plasma Atomic Emission

Spectroscopy (ICP-AES) are used additionally to compare the surface composition with that of bulk. According to the table, CNBs consist of carbon mostly, nitrogen, boron and oxygen, the amount of which vary according to those of their precursors. An increase in nitrogen content in bulk compared to surface are observed in all samples, which is common for CNs.¹¹³ On the other hand, boron contents in CNBs are rather increased on the surface and it seems to be related to our proposed surface-preferred reaction.

There is no big difference among the samples in nitrogen bonding states as depicted in Figures 34 and 35. Though there is some difference in the relative amounts, pyridinic N, N_{pyr} at 398.2eV, and quaternary N, N_{q} at 400.8eV, are developed mostly in the CNs and CNBs during the chlorination process. Considering the synthetic temperature (800°C) of the chlorination, normal nitrogen functional groups are supposed to change to quaternary nitrogen as observed from other study.²³ However, TiCl_4 , which facilitates pore formation during CN or CNB synthesis, is presumed to develop pyridine in the system.

Since binding energy of N_{pyr} is similar to that of B-N moiety in N 1s XPS, it is hard to distinguish each other in our CNBs. Therefore, the deconvolution of B 1s XPS is conducted and the results are shown in Figure 36. It indicates that C-B-N and B-N bonding (190.9ev) are the main sources for boron participation. But a small BC_3 contribution also appears as a sub peak (189ev) and the peak increases as the nitrogen content of the precursors increases. Even though BC_3 bonds are formed, they are unstable and break easily as a gas phase. However, once boron is bound to carbon, it behaves like a stabilizer in the reaction, making the C-N bonds strong. The high nitrogen

content of CNB37, despite of a low boron amount, proves that this nitrogen increment is not ascribed to that from B-N bonding. It seems that the role of BC_3 is more vigorous in making C-N bond strong under nitrogen-rich condition.

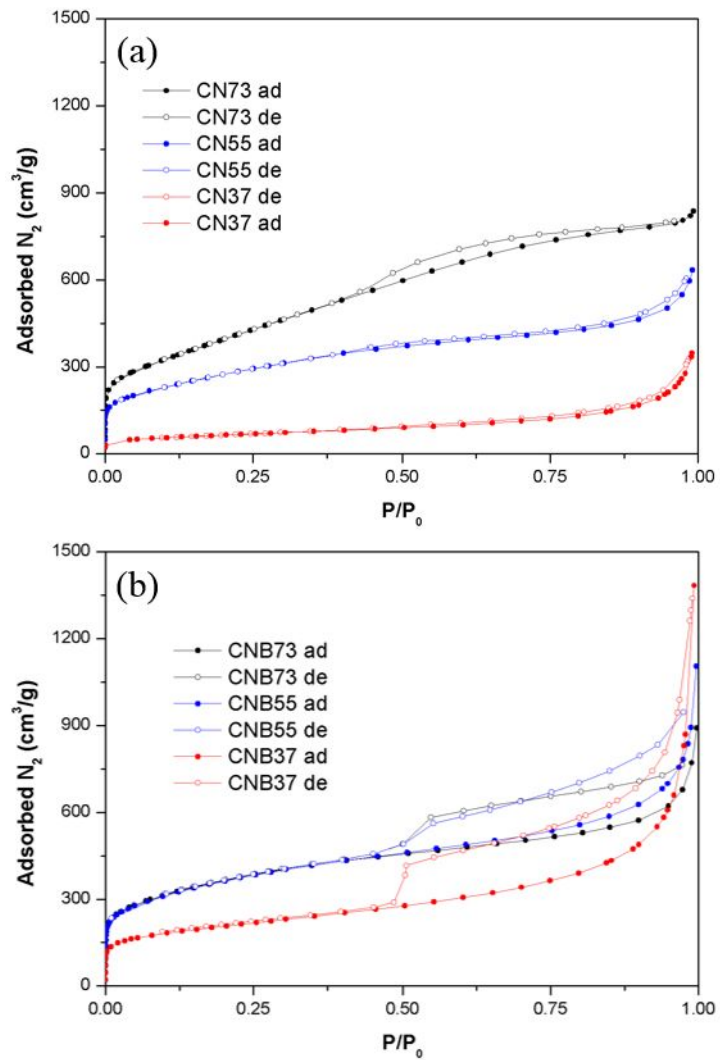


Figure 26. N₂ adsorption (ad, filled circles) and desorption (de, unfilled circles) curves of CNs (a) and CNBs (b) at 77 K.

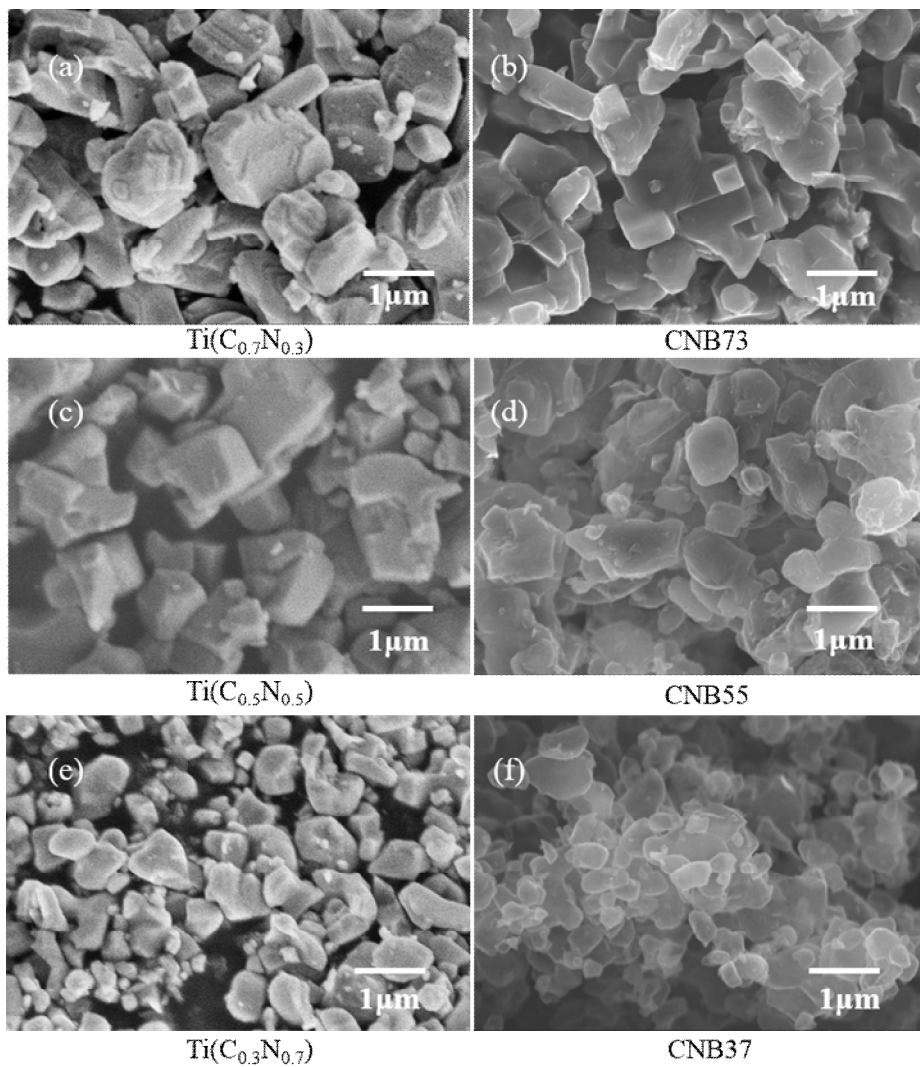


Figure 27. FE-SEM images of Ti(C_xN_y) precursors (left) and their corresponding CNBs (right).

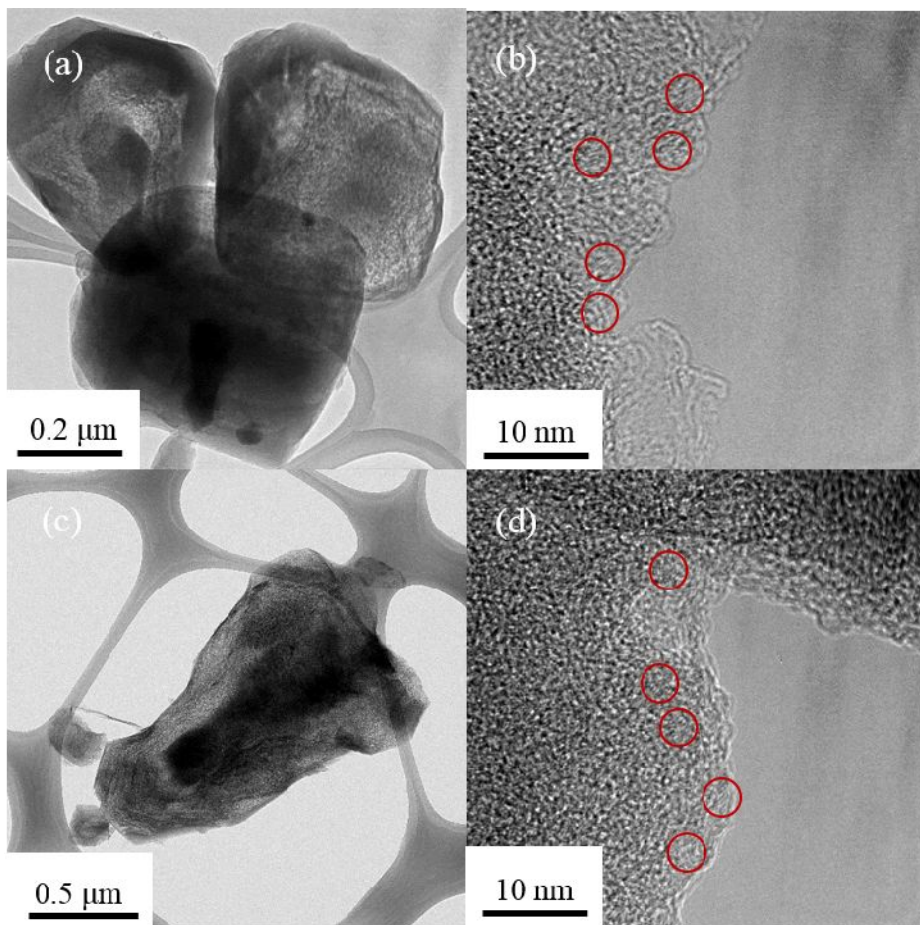


Figure 28. TEM images of (a) CNB73 and (c) CNB55, and high-resolution TEM images of (b) CNB73 and (d) CNB55. Red circles in (b) and (d) indicate short graphitic layers.

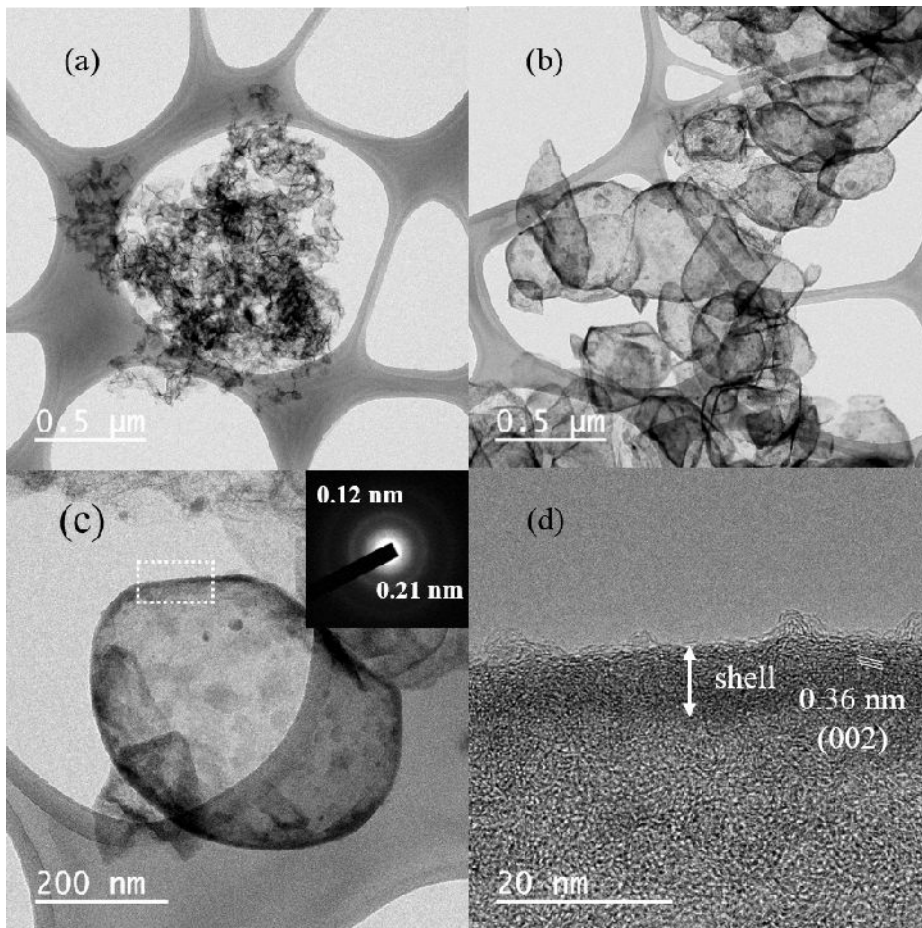


Figure 29. TEM images of (a) CN37 and (b),(c) CNB37. (d) High-resolution TEM image of CNB37. Inset in (c) shows SAED pattern at the shell area marked in (c) by the rectangular dashed line.

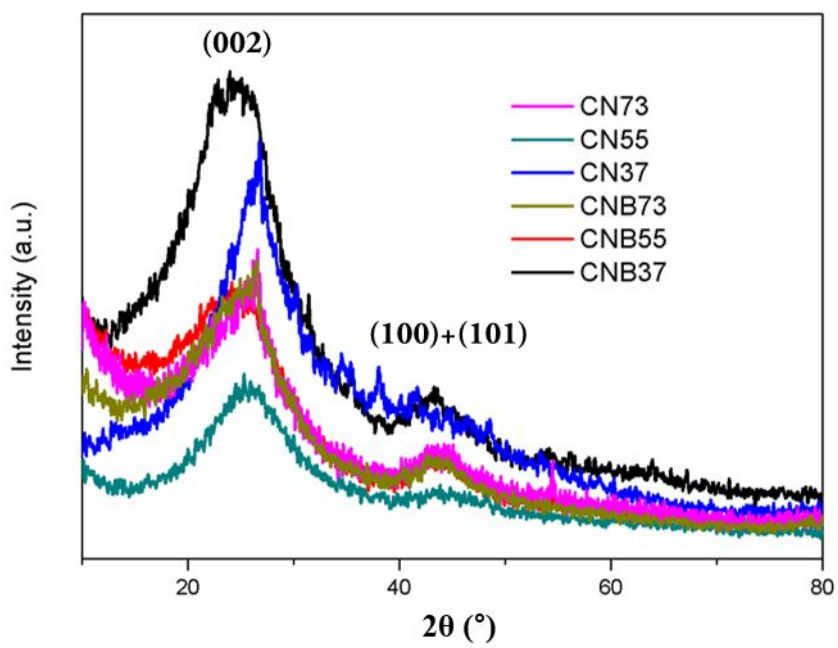


Figure 30. XRD spectra of synthesized CNs and CNBs.

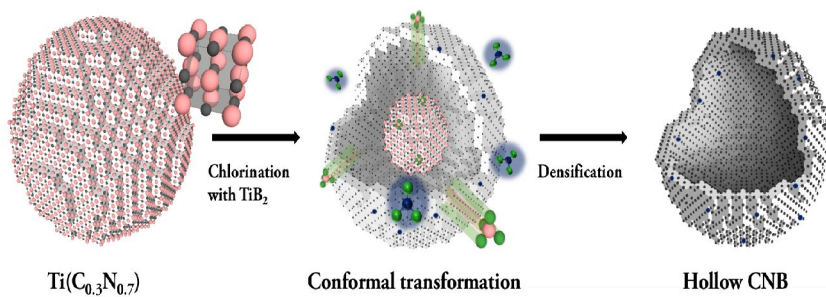


Figure 31. Proposed mechanism for the formation of hollow CNB37 structure where titanium, carbon or nitrogen, boron, and chlorine are represented by pink, black, blue, and green spheres, respectively. A quartered section of the CNB37 is excluded for clarity.

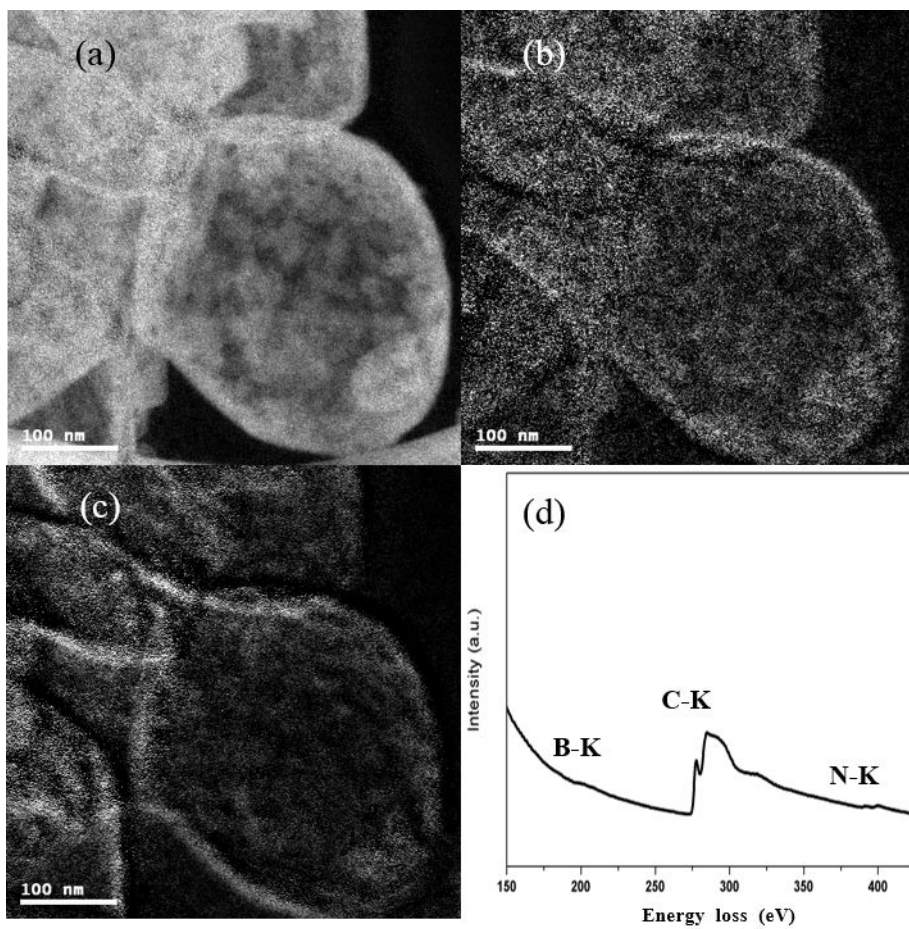


Figure 32. Elemental mapping of (a) carbon, (b) nitrogen, and (c) boron, and (d) EELS spectrum of CNB37 in the same region.

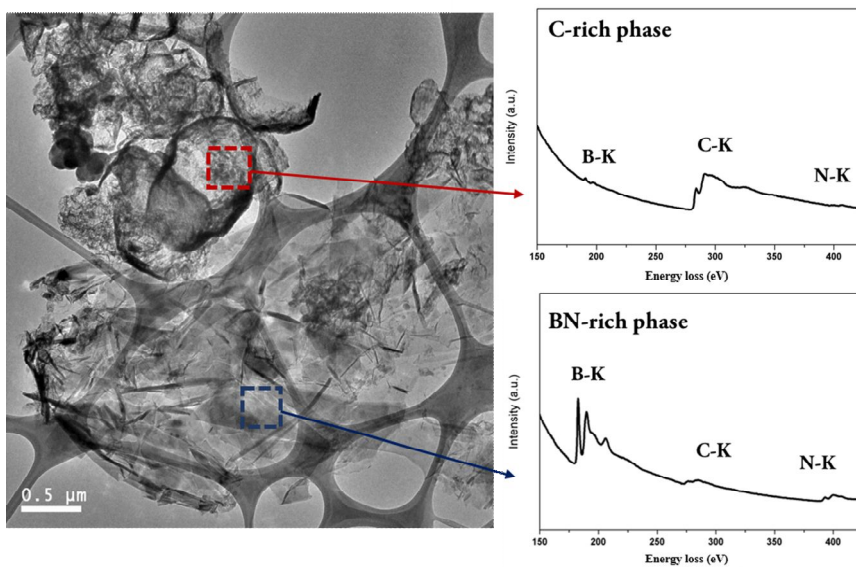


Figure 33. TEM images of CNB37 made with excess boron precursor and its corresponding EELS spectra for the regions of C- and BN-rich phases.

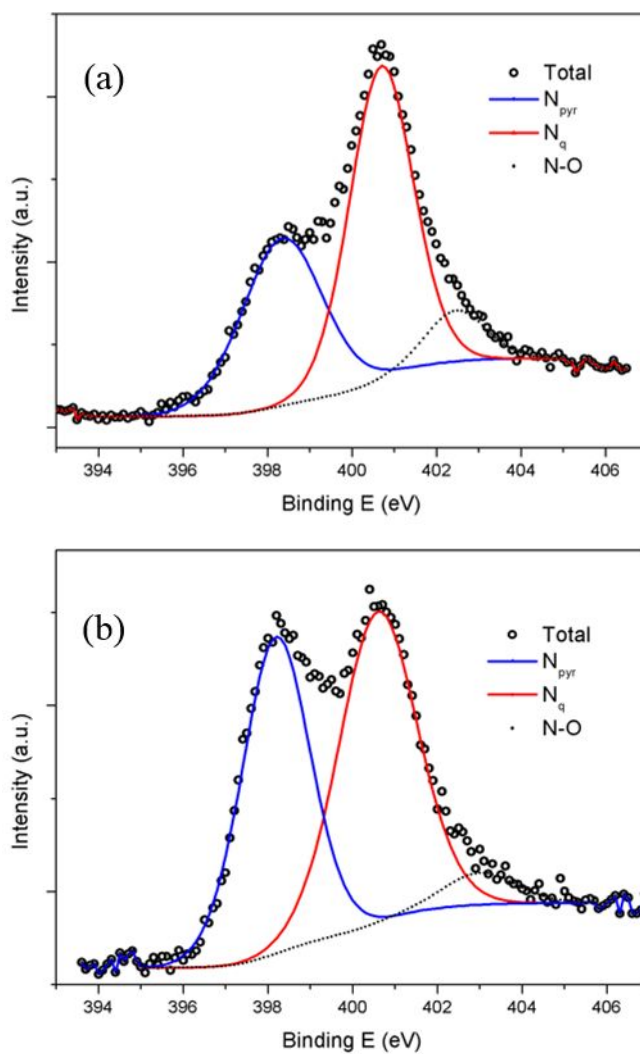


Figure 34. XPS N 1s spectra of (a) CN37 and (b) CNB37. Each peak is deconvoluted into several functional groups as N_{pyr} (398.2 eV), N_q (400.8 eV), and N-O (402.8 eV).

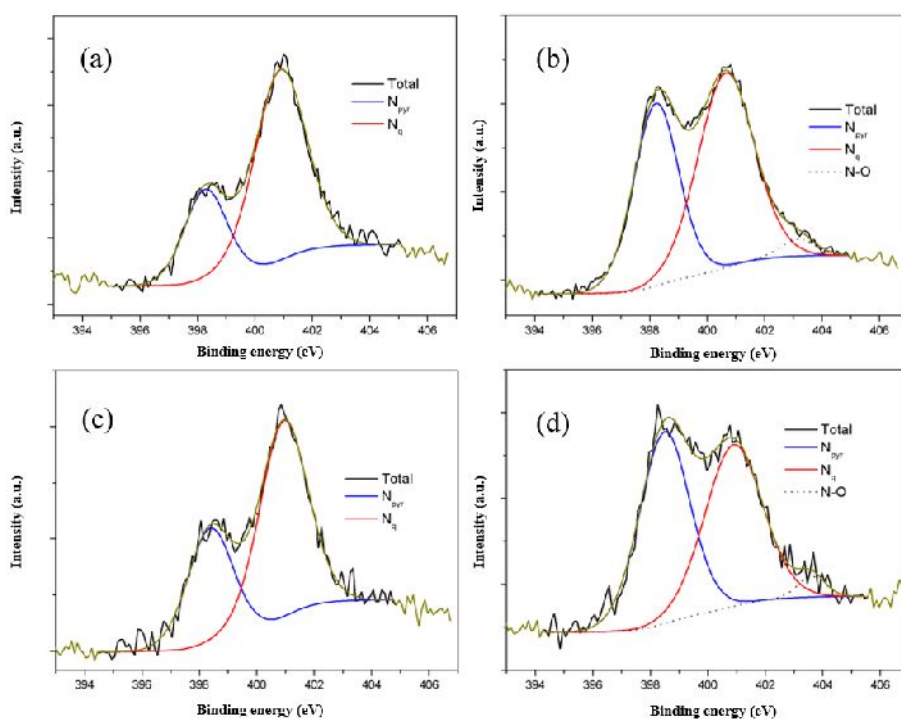


Figure 35. XPS N 1s spectra of CN55 (a), CNB55 (b), CN73 (c), and CNB73 (d). Each spectrum is deconvoluted into N_{pyr}, N_q, and N-O, respectively.

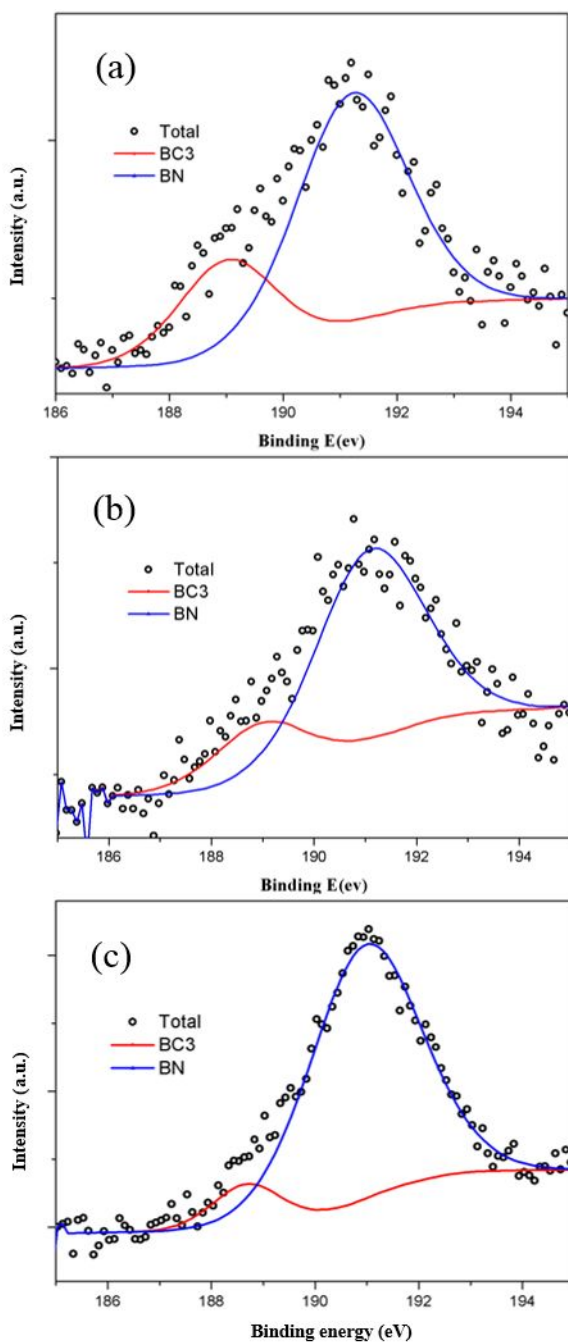


Figure 36. XPS B 1s spectra of CNB37 (a), CNB55 (b), and CNB73 (c). Each spectrum is deconvoluted into BN and BC₃.

	CN73	CN55	CN37	CNB73	CNB55	CNB37
Surface area (m ² /g)	1456	990	183	1304	1300	730
Total pore volume (cm ³ /g)	1.28	0.97	0.53	1.22	1.48	1.99
Micropore volume (cm ³ /g)	0.60	0.45	0	0.55	0.43	0.10
Mesopore volume (cm ³ /g)	0.67	0.37	0.27	0.43	0.59	0.77
Yield (%)	52.5	37.5	1.5	60.5	45.6	18.3

Table 5. Textural properties of synthesized CNs and CNBs. Surface area was derived from the BET equation. The total pore volume was measured up to $P/P_0 = 0.99$. Micro- and mesopore volumes were measured by the deBoer t-plot and Barrett–Joyner–Halenda (BJH) methods (adsorption branch between $0.3 < P/P_0 < 0.80$), respectively. Yield is calculated based on the amount of C, N, and B in the precursors.

	C (wt%)	B (wt%)	O (wt%)	N (wt%)	Nitrogen functional groups			CO ₂ capture (1 bar)	CO ₂ /N ₂ selectivity
					Pyridinic (398.2 eV, %)	Quaternary (400.8 eV, %)	Pyridine-N- oxide (403.5 eV, %)		
CNB73	84.6	1.4 (1.0)	7.3	4.5 (5.5)	49.4	47.7	2.9	3.10	16.6
CNB55	82.4	1.1 (0.7)	9.2	6.2 (8.0)	45.5	51.3	3.2	3.05	17.3
CNB37	79.9	0.4 (0.2)	10.1	8.2 (9.5)	44.8	50.5	4.7	3.70	35.2
CN73	88.3	0	7.2	2.2 (2.9)	35.3	64.7	0	2.55	16.4
CN55	85.4	0	9.0	3.8 (4.5)	28.1	71.9	0	2.33	16.8
CN37	77.6	0	14.2	6.5 (7.9)	37.1	54.7	8.2	-	-

Table 6. Chemical composition and CO₂ capture properties of synthesized CNs and CNBs. Composition analyses are done by XPS. Values in parentheses are determined by EA for nitrogen and ICP-AES for boron. The ratio of nitrogen functional groups is evaluated from their areas. The amount of CO₂ captured and the CO₂/N₂ selectivities are measured at 298 K. A CO₂ partial pressure of 0.1 bar is selected as the standard for the determination of selectivity.

3. 2. 2. Theoretical consideration of CNB

First principle calculation was performed to understand the effect of the BC_3 on the nitrogen functional groups in detail. For the calculation convenience, quaternary nitrogen, which is the most abundant functional group, was built in graphene structure and evaluated in terms of stability. The formation energy, E_{form} , of each nitrogen functional group is calculated as follows:

$$E_{\text{form}} = E_{\text{total}} (\text{N-doped graphene}) - E_{\text{total}} (\text{graphene}) + \mu_{\text{C}} - \mu_{\text{N}}, \quad (1)$$

$$E_{\text{form}} = E_{\text{total}} (\text{B- and N-co-doped graphene}) - E_{\text{total}} (\text{B-doped graphene}) + \mu_{\text{C}} - \mu_{\text{N}}, \quad (2)$$

Where E_{total} is the total energy of the system and μ_x the chemical potential of element x. A negative value of E_{form} means a spontaneous reaction and a positive value vice versa. Actually, boron and nitrogen possess one less and more valence electron per each, respectively, than carbon atom. Therefore, the charge compensation would be expected by co-doping and it gives rise to structural stability. In the calculation, it is found that the most stable configuration is formed when nitrogen is directly connected to boron as shown in Figure 37. The reduction in the formation energy is always low with boron in the vicinity of nitrogen as compared to the case without boron. This means that nitrogen gets more opportunities to have a bond effectively with

carbon under the boron existence. A similar stabilization effect is also noted by BCl_3 addition as shown in Figure 38, proving that with addition of boron its intermediate phase can act as a stabilizing agent for nitrogen incorporation. The effect of BCl_3 on the formation of N-doped graphene is calculated as below;

$$\Delta E = E_{\text{total}} (\text{N-doped graphene with } \text{BCl}_3 \text{ molecule}) - E_{\text{total}} (\text{N-doped graphene}) - E_{\text{total}} (\text{free } \text{BCl}_3 \text{ molecule}) = -0.34$$

Which means that the formation of N-doped graphene is energetically more favorable under BCl_3 existence. Other boron compounds as well as BCl_3 also can be expected to work analogous role due to their common Lewis acid properties.

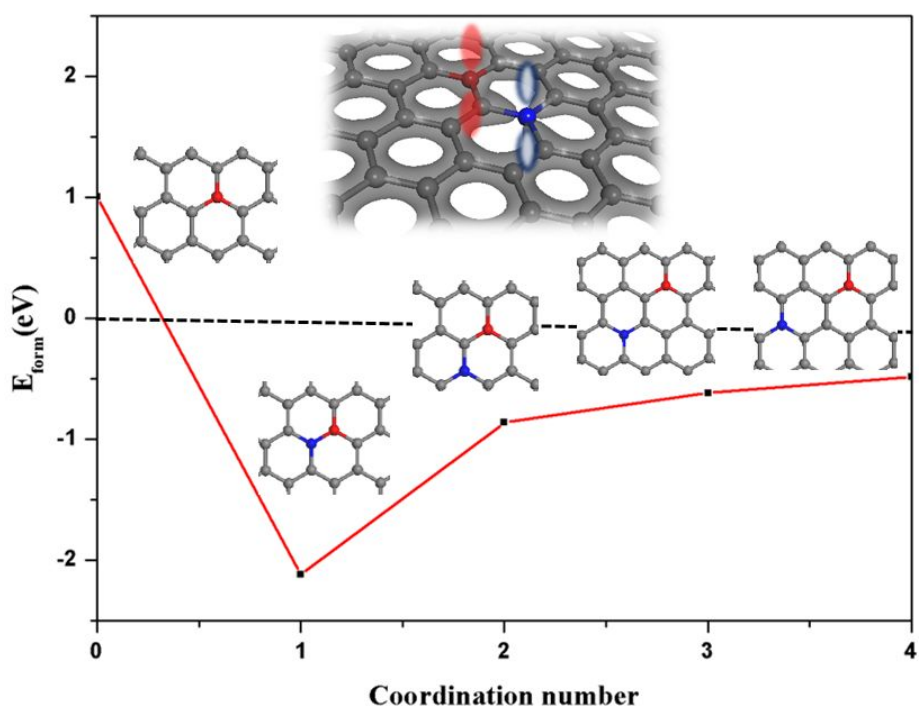


Figure 37. Calculated formation energy for nitrogen doping in graphene sheets with respect to the boron position relative to nitrogen. The carbon, nitrogen, and boron atoms are shown in gray, red, and blue, respectively.

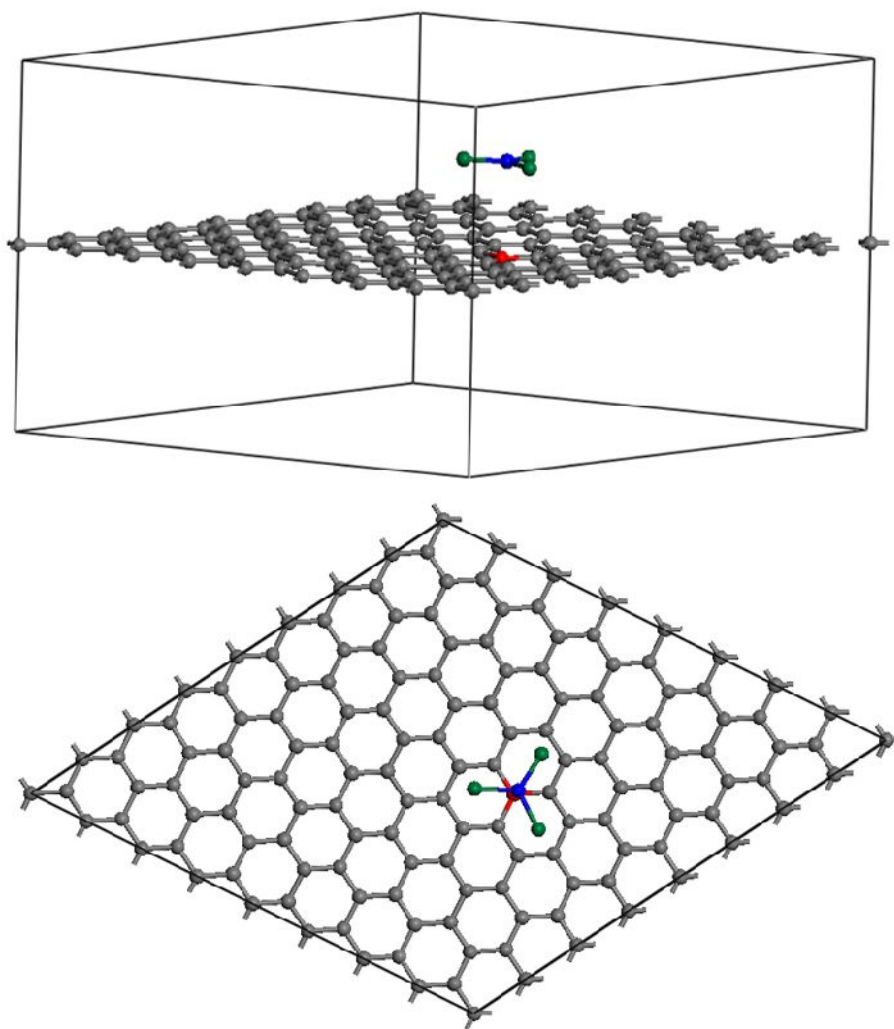


Figure 38. Geometric configuration of BCl₃ molecule in the vicinity of quaternary nitrogen embedded in a graphene sheet (C, N, B, and Cl atoms are black, red, blue, and green, respectively).

3. 2. 3. CO₂ capture of porous CNB

For the application of these nitrogenous porous carbons, CO₂ capture properties are then evaluated. (Figure 39 (a)) In Table 6 is summarized the CO₂ capture properties of the CNs and CNBs. Since the quantity of CN37 we obtained is so small (see the yield in Table S1) and unreliable, we exclude the result. Every CNB provides better uptakes than corresponding CNs regardless of surface area. Of those samples notable uptake, 3.7mmol/g, is achieved by CNB37. After five repeated cycles of CO₂ capture measurements without any heat treatment, there was no degradation observed as shown in Figure 40. Moreover, the CO₂/N₂ selectivity, extrapolated on the basis of IAST (Ideal Adsorption Solution theory),¹¹⁴ was remarkably increased in CNB37. (Figure 39 (b)) The modified IAST can be expressed as follows

$$S = \frac{q_1/q_2}{p_1/p_2}$$

Where S means the selectivity, q the molar quantity of species i (mmol/g) and p the partial pressure of species i (bar).

Single-site Langmuir fitting was used to determine molar quantity as a function of the partial pressure.

$$q_i = q_{i,max} \frac{k_i p_i}{1 + k_i p_i}$$

$q_{i,max}$ = Maximum molar gas uptakes of species i (mmol/g)

k_i = Langmuir constant (bar⁻¹)

The overall values of each samples are summarized in table 7. Especially at

CO₂ partial pressure of 0.1 bar (total pressure of 1 bar), which is similar to real post-combustion gas mixture, outstanding selectivity of 35.2 is observed and it is even better than the best CN materials ever reported.²⁷

This selective sorption of non-ordered structure has been usually explained by nitrogen atoms present on the pore surface, which could increase the surface-adsorbate interaction.⁴⁶ In our experiments, the selectivity increases with nitrogen contents especially at low CO₂ partial pressure. However, comparing to the selectivity difference between CNB73 and CNB55, the great increase of CNB37 cannot be explained simply by nitrogen content or character of functional groups. The uniqueness of hollow CNB37 in short pore features and hierarchical structure could be the cause for the enhancement of the capture amounts as well as selectivity. The effect of the morphology has not been well discussed yet in CCS area, but a hollow structure already has demonstrated its outstanding properties in various fields such as gas sensor and catalysts.^{115, 116} Also, a significant increase in hydrogen uptakes with hollow BN has been reported.¹⁵ Therefore, the hollow structure of CNB37 would be worthy to note for its effectiveness in CO₂ capture and the selectivity.

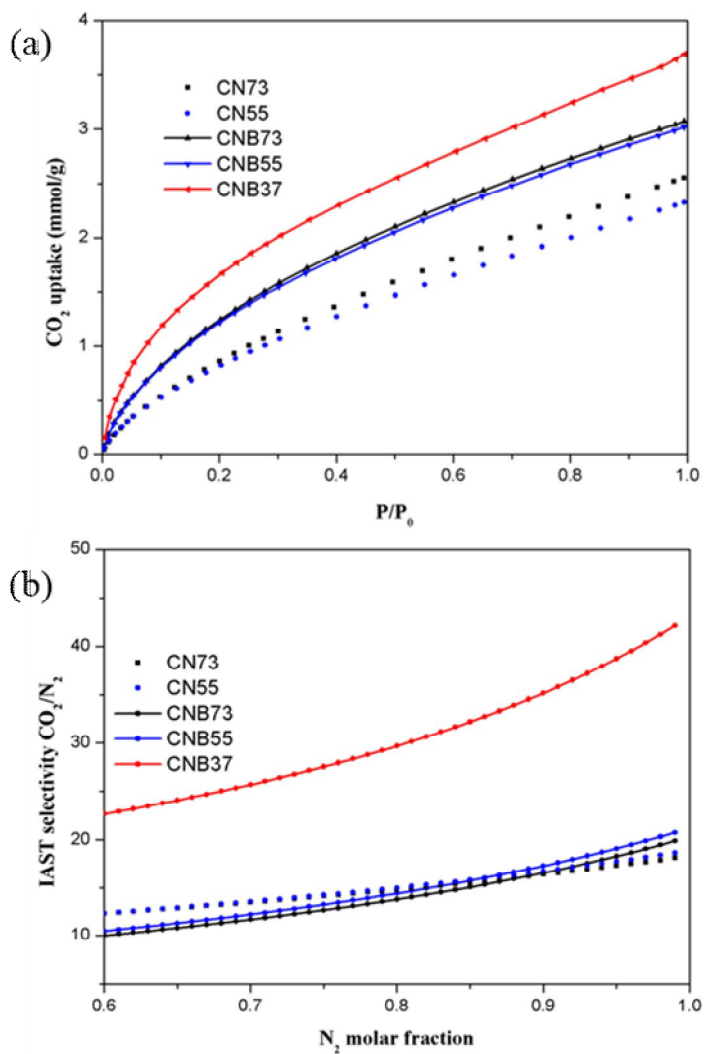


Figure 39. (a) CO₂ adsorption isotherms of CNs and CNBs measured at 298 K and (b) their CO₂/N₂ selectivity versus N₂ molar fraction. Evaluation at 1 bar total pressure by the IAST method.

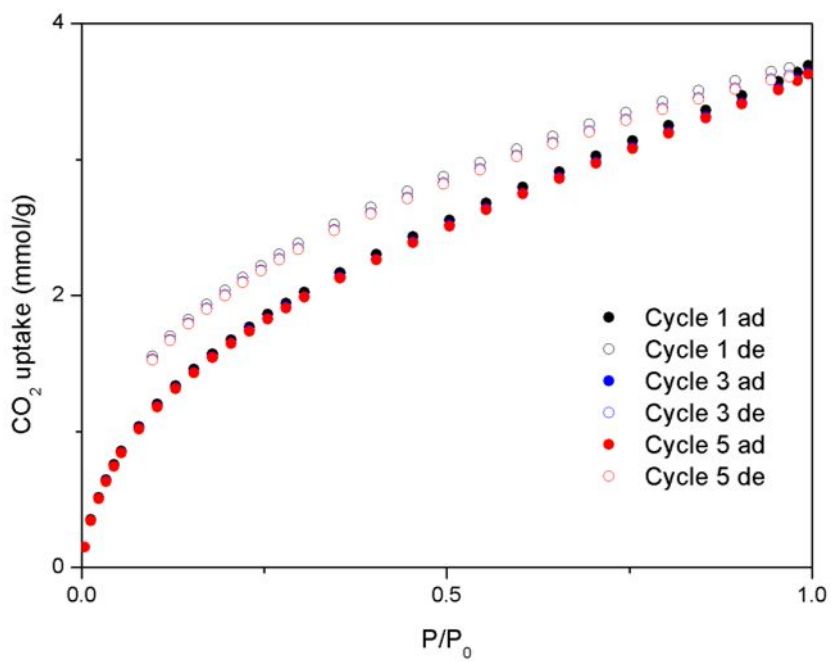


Figure 40. CO₂ capture properties of CNB37 at 298 K for five adsorption-desorption cycles.

	$q_{i,max}$ (mmol/g)		k_i (bar ⁻¹)	
	CO ₂ (298 K)	N ₂ (298 K)	CO ₂ (298 K)	N ₂ (298 K)
CNB73	4.89	0.12	1.81	0.61
CNB55	4.54	0.10	1.80	0.61
CNB37	4.76	0.37	2.70	2.55
CN73	4.93	0.20	1.01	0.16
CN55	4.19	0.23	1.16	0.12

Table 7. Single-site Langmuir fitting values for IAST evaluation where each sample was fitted separately for CO₂ and N₂ adsorption.

3. 2. 4. Synthesis of super-activated CNB

In our previous section, the new concept of synthetic method for nitrogen and boron co-doped porous carbon was demonstrated by CDC (Carbide derived carbon)-like process and proved its effectiveness for CO₂ capture. The small amount of boron addition enhance the stability of nitrogen functional groups and affects the amount of capture capacities. Herein, for the further improvement, we conducted the KOH activation to enlarge the surface area and the expectation agrees well with experimental values. This super-activated samples are denoted here as K-CNBXY where K means KOH activation and X, Y are referred to as molar ratio of precursor Ti(C_{0.x}N_{0.y}), respectively.

FE-SEM analysis were performed to explore the shape of samples at first and shown in figure 41. Even though more porous character is appeared, an overall morphology of K-CNBs are not altered compared to corresponding CNBs and maintain its original forms of precursors. Especially, K-CNB37 shows unique hollow structure according to TEM analysis and it assemble to CNB37 (Figure 42). But a deep contrast at the vicinal shell tells that the total density of K-CNB37 is decreased than CNB37 due to the chemical activation.

This super-activation method is already reported as a post activation of CDC materials.^{117, 118} According to them, much more pores, especially micropores, are developed when porous materials is further activated by KOH as shown in figure 43. The general activation reaction occurs as follows.



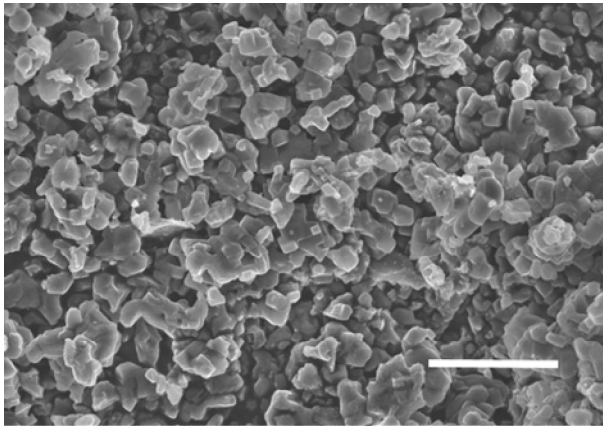
A respectable amount of carbon is etched by this mechanism and pore is generated as results. As shown of the N₂ adsorption-desorption isotherms in figure 44, the significant adsorption branch is observed at $<0.1P/P_0$ which means the development of micropore. It also results in meaningful increase of surface area as porous carbon or nitrogenous carbon did.

Nevertheless, the decrease of nitrogen contents was small and some were rather increased in produced K-CNBs merely more prominent for carbon richer precursors. The nitrogen contents, measured by elemental analysis (EA), before and after KOH activation is summarized with textural properties in table 8. In General, when nitrogen containing carbon is activated by KOH, significant loss of N occurs simultaneously because of the less stability of that functional group to the oxidation atmosphere under certain temperatures.¹¹⁹ Therefore, it is known that high nitrogen contents is incompatible with large surface area.

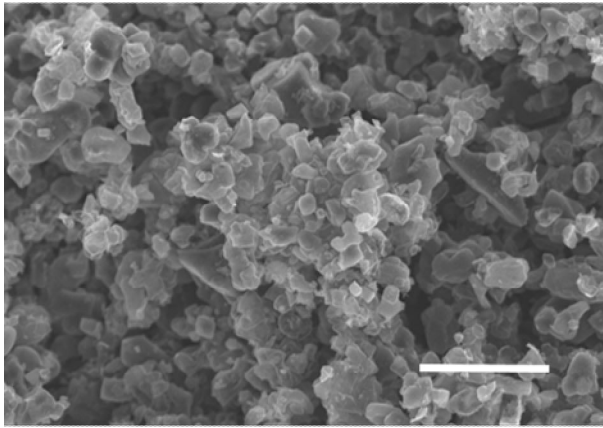
It seems that since CNBs are synthesized under quite high temperature (800°C), higher stabilities are accomplished as the results. According to Thermal Gravimetric Analysis (TGA) (fig. 45), although more decrease was detected as nitrogen contents of precursor increases, there is no serious weight loss of CNBs until 800°C under air atmosphere. The initial loss around 100°C is just originated from physically adsorbed air and water. These behaviors are

certainly different from that of general CN materials which ready to decompose around 400°C under air.¹²⁰

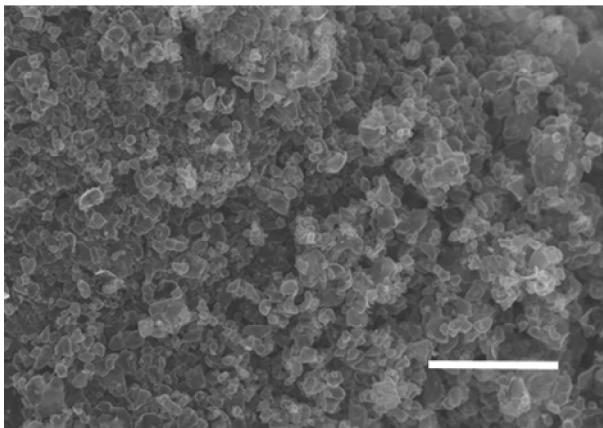
To figure out the bonding nature, chemical states are investigated by XPS analysis and present in figure 46. It confirms that quaternary N group (N_q , 400.8ev) is transformed to pyridonic (N_{don}) or pyrrolic (N_{rol}) N groups (400ev) and it is very common in KOH activation of nitrogenous carbon.²⁷ Since KOH activation induce oxidation atmosphere, we refer it here as N_{don} . The portion decrease of pyridinic N peak (N_{pyr} , 398ev) is also observed in every K-CNBs and it can be explained by two ways. First of all, N_{pyr} was transformed to N_{don} as N_q did in this oxidation atmosphere. Also B-N moieties, which is hard to distinguish from N_{pyr} in our samples, can be by etched by KOH. This etching conditions are resulted in decrease of total B content.



K-CNB73



K-CNB55



K-CNB37

Figure 41. FE-SEM images of synthesized K-CNBs.

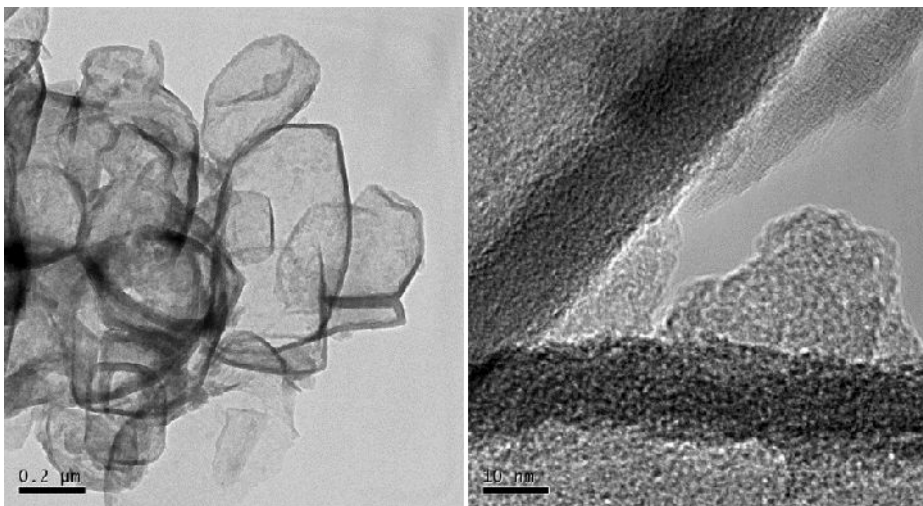


Figure 42. TEM image of K-CNB37 and HR-TEM image of K-CNB37.

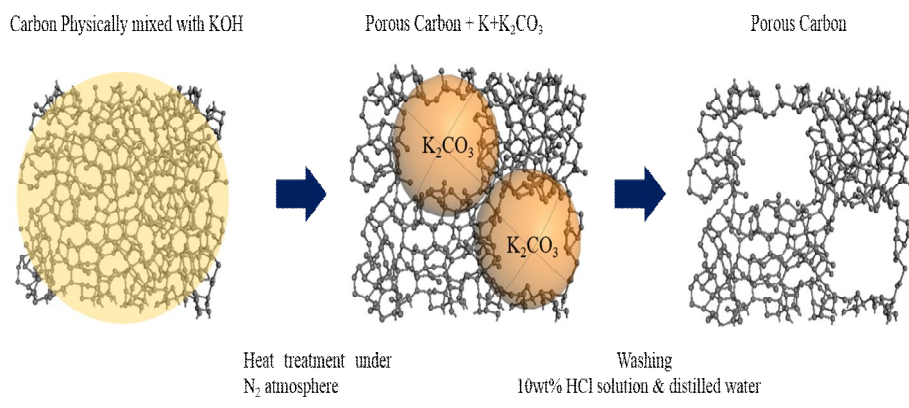


Figure 43. Schematic diagram of KOH activation process.

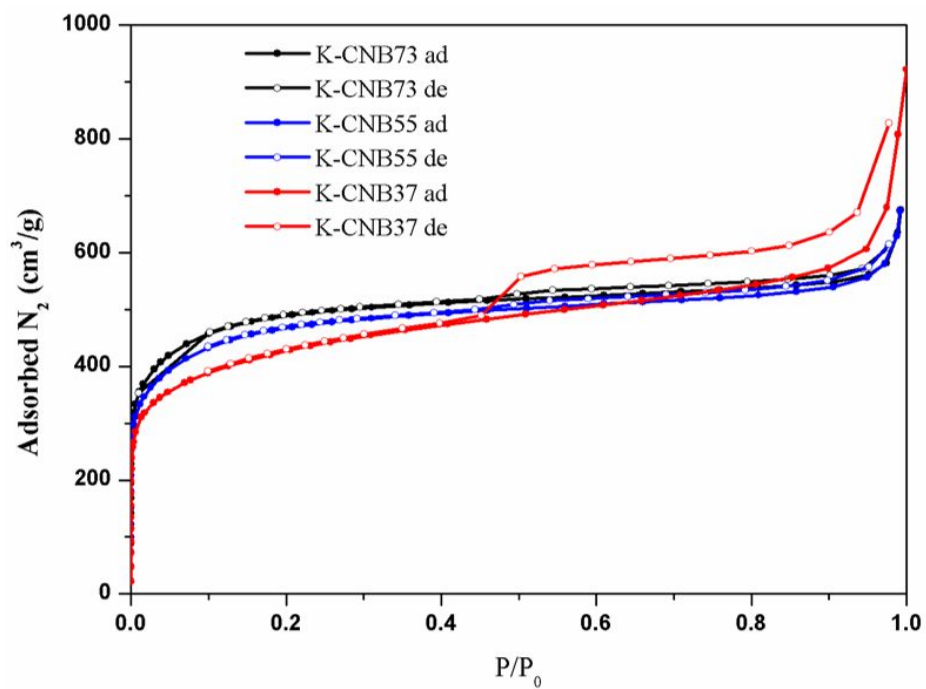


Figure 44. N₂ isotherms of synthesized K-CNBs. Close symbol represents adsorption (ad) and open symbol represent desorption (de).

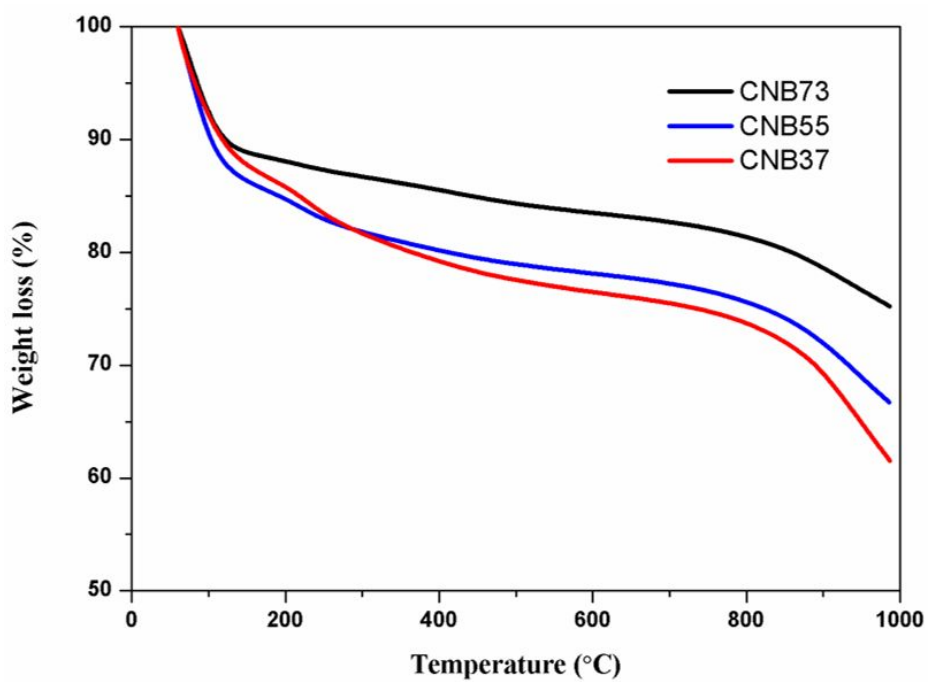


Figure 45. TGA analysis of synthesized CNBs under air.

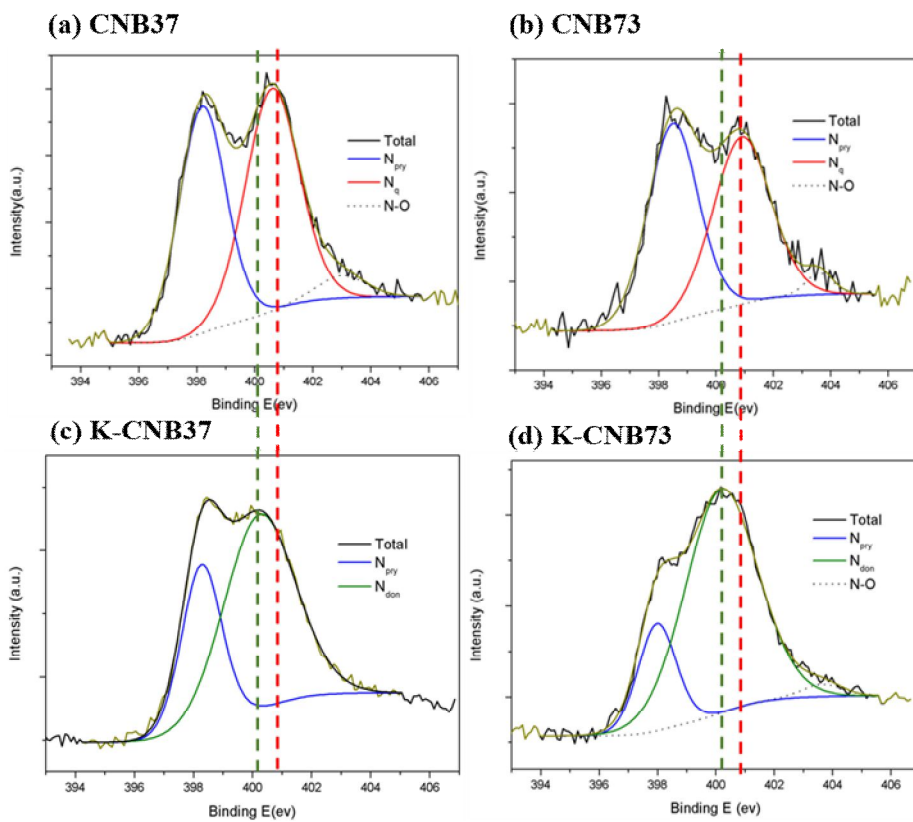


Figure 46. N 1s spectra of (a) CNB37, (b) CNB73, (c) K-CNB37 and (d) K-CNB73.

sample	N (wt%)	BET SSA (m ² /g)	CO ₂ Uptakes (298K) (mmol/g)	
			0.1 bar	1 Bar
CNB73	5.5	1310	0.80	3.10
CNB55	8.0	1280	0.78	3.05
CNB37	9.5	725	1.10	3.75
K-CNB73	7.8	1870	0.90	4.40
K-CNB55	8.9	1750	0.91	4.29
K-CNB37	10.1	1340	1.23	4.75

Table 8. Overall properties of K-CNBs compared to corresponding CNBs. Nitrogen contents are measured by elemental analysis.

3. 2. 5. CO₂ capture of super-activated CNB

These synthesized K-CNBs show significant CO₂ capture properties as shown in figure 47. Since surface area become larger without heavy loss of nitrogen contents, rather increase in K-CNB73, it results in such an enhancement. The abundance of pyridonic groups is also known as assistant of that. Especially K-CNB37 shows excellent CO₂ uptakes of 4.75mmol/g at ambient temperature and 1bar compared to other nitrogenous carbon as depicted in figure 48. To the best of our knowledge, it is the highest value among carbon based materials. Furthermore, it possesses high CO₂/N₂ selectivity evaluated by IAST method as we did in previous section. That reaches 30 at 0.1bar of CO₂ partial pressure. The maintained hollow structure of K-CNB37 effects such an enhancement as it does in the previous section of CNB37.

To examine the CO₂ capture properties of samples more precisely, we summarized several CCS candidates, mostly CNs, in table 9. The normalization of capture per surface area was also conducted for better comparison. According to the results, nitrogen doping apparently subserve the enhancement of CO₂ capture at low pressure. Even though CN generally possesses smaller surface area, better uptakes compared to row carbons are well presented as the pressure of CO₂ decreases.

However, we can hardly find the direct correlation of capture amounts to the absolute contents of nitrogen similar to previous report.⁹⁵ Instead, the

proportional decrease versus surface area is observed as shown in figure 49 regardless of nitrogen content. Actually, K-CNB37, the best capturer, doesn't likewise free from this trend and which means large surface area with high nitrogen content doesn't satisfy the enhanced capture property. Furthermore, compared to zeolite called Ca-A,¹²¹ every CNs show deficient capture property with remarkably lower selectivity.

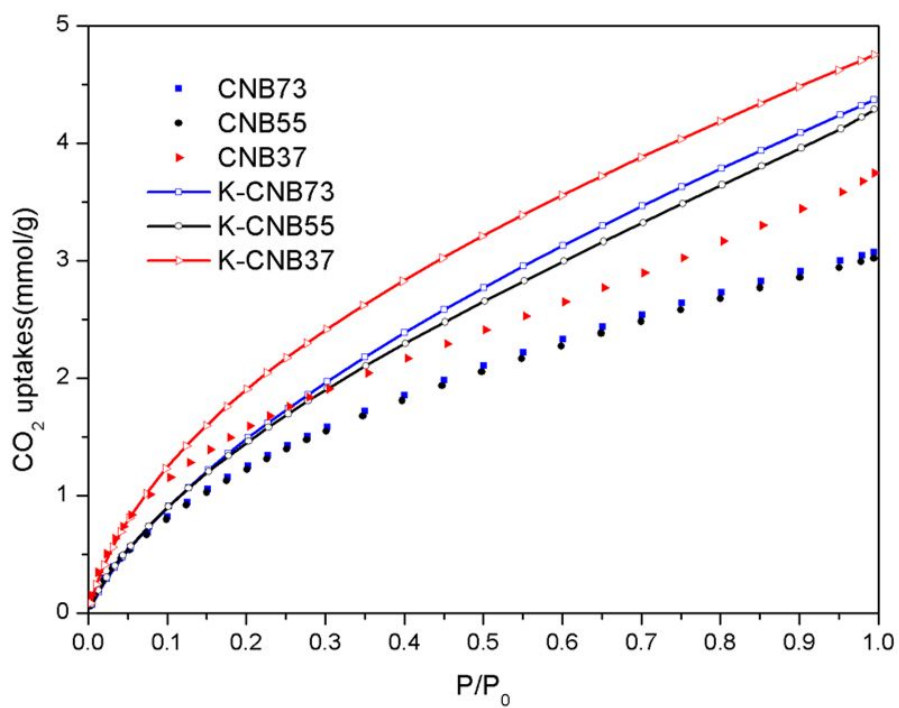


Figure 47. CO₂ adsorption isotherms of K-CNBs compared to corresponding CNBs measured at 298K.

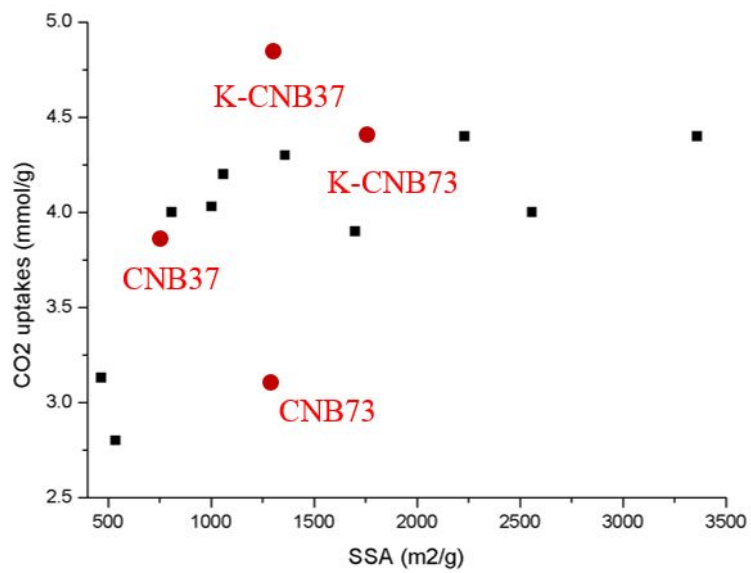


Figure 48. CO₂ uptakes of various nitrogenous carbon versus surface area.

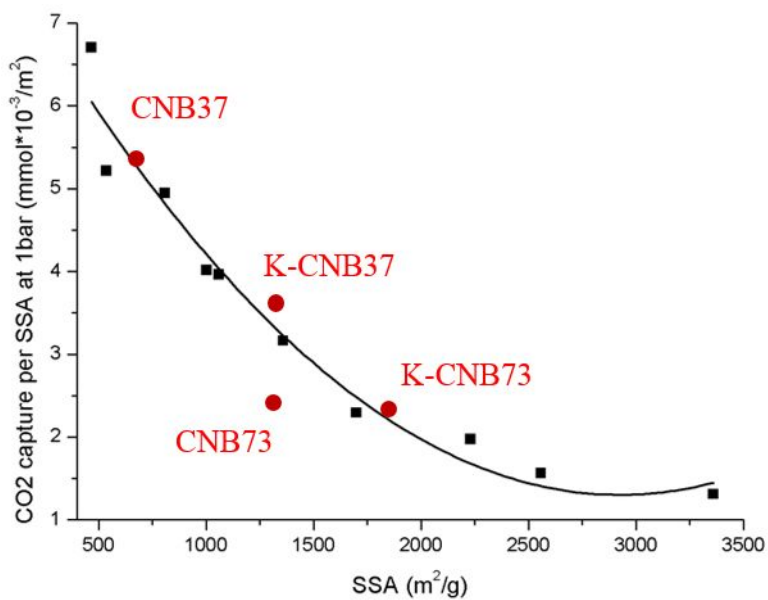


Figure 49. CO₂ capture amount per surface area of various nitrogenous carbon versus surface area.

Nomenclature	SSA (m ² / g)	N content	CO ₂ capture (298K)		CO ₂ /N ₂ Selectivit y	CO ₂ capture per SSA (0.1bar) mmol/m ² (*10 ⁻³)
			0.1bar	1bar		
CNB-37	752	7.49	1.17	3.8	21.5	1.61
K-CNB-37	1340	8.50	1.23	4.8	Not yet	1.27
CNB-73	1310	4.10	0.80	3.1	Not yet	0.61
K-CNB-73	1870	6.80	0.90	4.4	16.6	0.48
AC	3000	0	0.5	2.5	NA	0.17
TiC-CDC-700	1490	0	0.65	3.8	NA	0.44
CEM-750	3360	5.2	0.74	4.38	NA	0.22
PAN-PK	2231	8.1	0.63	4.4	NA	0.28
N-TC-EMC	2559	7	1.07	4.0	14	0.42
CP-2-600	1700	10.1	0.83	3.9	5.3	0.49
A-NDC6	1360	4.8	0.85	4.3	34	0.63
SK-0.5-700	1060	0.4	1.01	4.2	NA	0.95
HMT-80-900	809	2.0	1.3	4.0	NA	1.60
H-NMC-2.5	537	13.10	1.1	2.8	NA	2.05
RFL-500	467	1.92	1.01	3.13	NA	2.16
KNC-A-HCl	1004	12.9	1.03	4.03	26	1.03
Ca-A	NA	-	3.8	5.0	250	NA

Table 9. CO₂ capture properties of various porous materials. CO₂/N₂ selectivity is evaluated by IAST method at 0.1 bar of CO₂ partial pressure.

3. 2. 6. Conclusions

Nitrogen containing porous carbon has been successively synthesized by the addition of boron source at a high synthetic temperature, rendering a large surface area. A small amount of boron addition changes the reaction atmosphere and facilitates nitrogen to participate in the carbon structure. The CNBs obtained from the chlorination process show higher thermal stability and productivity (yields) than corresponding CNs. Among the CNBs, CNB37 shows a hollow spherical structure. The nitrogen-rich titanium carbo-nitride precursor works as a self-template and titanium is completely consumed, leaving a hollow shell structure. The working mechanism can be explained by the direct boron doping to the surface of the precursor particles along with the loss of the interior CN and the effect of BCl_3 as a Lewis acid-base interaction on the surface energy. It is worth noticing that morphology modification of CN(B) would be possible, depending on the shape control of nitrogen containing precursor without any post-treatments. Additionally, although CNB37 possesses smaller area than others, it shows higher CO_2 uptakes and CO_2/N_2 selectivity at ambient temperature. It seems that hollow morphology affects the sensitivity of interaction and is in consequence this enhancement. The additional works for further improvement and the development of variable applications, based on self-template hollow CNB, are now in progress and will be discussed in our future publication.

Furthermore, large surface area CNBs are synthesized by KOH post-

activation called super-activation. This activation doesn't affect overall morphology much and rather causes the increase the nitrogen content contrary to normal KOH treatment because of the higher thermal stability of corresponding CNBs. This high nitrogen content with the development of micropore at the same time result in enhancement of CO₂ capture and their properties, which has increased to 4.75mmol/g, are surely the best among reported nitrogenous carbon at ambient temperature of 1bar.

4. Overall conclusions

The novel synthesis of carbon analogue, C-N-B has been demonstrated. Ceramic derived high surface area C-N-Bs are simply developed by chlorination method. This approach provides a new method for synthesizing other porous binary or multi-nary compounds as well. The driving force of formation and the influence of hetero atoms in matrix are explored both experimental and theoretical methods.

Porous boron nitrides (BNs) were successively synthesized by chlorination of TiB_2 and TiN mixture. High micro-porosity with a large surface area ($960\text{m}^2/\text{g}$) was measured especially at the synthetic temperature of 600°C and unique hydrogen sorption properties was also observed. The evaluated heat of adsorption (Q_{st}) is higher than general carbonous materials and it match with previous theoretical prediction.

However, despite of its enhancement, Q_{st} is still too low to operate at the ambient temperature. Aluminum doped BN is one of the realistic candidate to solve this problem. It can be synthesized by high energy boron source and binding energy is maintained above 0.1eV even after seventh hydrogen molecules adsorption. Therefore, the experimental efforts are highly encouraged to fabricate this aluminum doped BN for sustainable developments.

Porous nitrogen and boron co-doped carbon (CNBs) were further derived by similar method for porous BNs. The judicious approach of precursor ratio was

conducted to prevent phase isolation, common in reported CNBs. The prepared CNBs form variable structures, depending on their compositions of precursors via chlorination. Especially, hollow structure without any additional templates was developed, which is definitely of first discovery in this CNB field. We also expect that this new insight of the role of boron or boron compounds for the nitrogen incorporation could offer other materials opportunities to the scientific community. After chemical activation, surface area was increased without significant nitrogen loss. These factors result in enhancement of carbon dioxide capture and, to the best of our knowledge, it is the highest uptake property among carbon based materials.

References

1. Gogotsi, Y.; Nikitin, A.; Ye, H. H.; Zhou, W.; Fischer, J. E.; Yi, B.; Foley, H. C.; Barsoum, M. W. Nanoporous carbide-derived carbon with tunable pore size. *Nat. Mater.* 2003, 2, 591-594.
2. Gogotsi, Y.; Dash, R. K.; Yushin, G.; Yildirim, T.; Laudisio, G.; Fischer, J. E. Tailoring of nanoscale porosity in carbide-derived carbons for hydrogen storage. *J. Am. Chem. Soc.* 2005, 127, 16006-16007.
3. Yushin, G.; Dash, R.; Jagiello, J.; Fischer, J. E.; Gogotsi, Y. Carbide-derived carbons: Effect of pore size on hydrogen uptake and heat of adsorption. *Adv. Funct. Mater.* 2006, 16, 2288-2293.
4. Simon, P.; Gogotsi, Y. Materials for electrochemical capacitors. *Nat. Mater.* 2008, 7, 845-854.
5. Chmiola, J.; Largeot, C.; Taberna, P. L.; Simon, P.; Gogotsi, Y. Monolithic Carbide-Derived Carbon Films for Micro-Supercapacitors. *Science* 2010, 328, 480-483.
6. Presser, V.; Heon, M.; Gogotsi, Y. Carbide-Derived Carbons - From Porous Networks to Nanotubes and Graphene. *Adv. Funct. Mater.* 2011, 21, 810-833.
7. Giovannetti, G.; Khomyakov, P. A.; Brocks, G.; Kelly, P. J.; van den Brink, J. Substrate-induced band gap in graphene on hexagonal boron nitride: Ab initio density functional calculations. *Phys. Rev. B* 2007, 76.
8. Dean, C. R.; Young, A. F.; Meric, I.; Lee, C.; Wang, L.; Sorgenfrei, S.; Watanabe, K.; Taniguchi, T.; Kim, P.; Shepard, K. L.; Hone, J. Boron

- nitride substrates for high-quality graphene electronics. *Nat. Nanotechnol.* 2010, 5, 722-726.
9. Decker, R.; Wang, Y.; Brar, V. W.; Regan, W.; Tsai, H. Z.; Wu, Q.; Gannett, W.; Zettl, A.; Crommie, M. F. Local Electronic Properties of Graphene on a BN Substrate via Scanning Tunneling Microscopy. *Nano Lett.* 2011, 11, 2291-2295.
10. Golberg, D.; Bando, Y.; Tang, C. C.; Zhi, C. Y. Boron nitride nanotubes. *Adv. Mater.* 2007, 19, 2413-2432.
11. Golberg, D.; Bando, Y.; Huang, Y.; Terao, T.; Mitome, M.; Tang, C. C.; Zhi, C. Y. Boron Nitride Nanotubes and Nanosheets. *ACS Nano* 2010, 4, 2979-2993.
12. Chopra, N. G.; Luyken, R. J.; Cherrey, K.; Crespi, V. H.; Cohen, M. L.; Louie, S. G.; Zettl, A. BORON-NITRIDE NANOTUBES. *Science* 1995, 269, 966-967.
13. Tang, C. C.; Bando, Y.; Huang, Y.; Zhi, C. Y.; Golberg, D. Synthetic Routes and Formation Mechanisms of Spherical Boron Nitride Nanoparticles. *Adv. Funct. Mater.* 2008, 18, 3653-3661.
14. Coleman, J. N.; Lotya, M.; O'Neill, A.; Bergin, S. D.; King, P. J.; Khan, U.; Young, K.; Gaucher, A.; De, S.; Smith, R. J.; Shvets, I. V.; Arora, S. K.; Stanton, G.; Kim, H. Y.; Lee, K.; Kim, G. T.; Duesberg, G. S.; Hallam, T.; Boland, J. J.; Wang, J. J.; Donegan, J. F.; Grunlan, J. C.; Moriarty, G.; Shmeliov, A.; Nicholls, R. J.; Perkins, J. M.; Grievson, E. M.; Theuwissen, K.; McComb, D. W.; Nellist, P. D.; Nicolosi, V. Two-Dimensional Nanosheets Produced by Liquid Exfoliation of Layered Materials. *Science* 2011, 331, 568-

571.

15. Lian, G.; Zhang, X.; Zhang, S. J.; Liu, D.; Cui, D. L.; Wang, Q. L. Controlled fabrication of ultrathin-shell BN hollow spheres with excellent performance in hydrogen storage and wastewater treatment. *Energy Environ. Sci.* 2012, 5, 7072-7080.

16. Tiwari, J. N.; Tiwari, R. N.; Kim, K. S. Zero-dimensional, one-dimensional, two-dimensional and three-dimensional nanostructured materials for advanced electrochemical energy devices. *Prog. Mater. Sci.* 2012, 57, 724-803.

17. Han, W. Q.; Brutchey, R.; Tilley, T. D.; Zettl, A. Activated boron nitride derived from activated carbon. *Nano Lett.* 2004, 4, 173-176.

18. Vinu, A.; Terrones, M.; Golberg, D.; Hishita, S.; Ariga, K.; Mori, T. Synthesis of mesoporous BN and BCN exhibiting large surface areas via templating methods. *Chem. Mat.* 2005, 17, 5887-5890.

19. Dibandjo, P.; Bois, L.; Chassagneux, F.; Cornu, D.; Letoffe, J. M.; Toury, B.; Babonneau, F.; Miele, P. Synthesis of boron nitride with ordered mesostructure. *Adv. Mater.* 2005, 17, 571-574.

20. Rushton, B.; Mokaya, R. Mesoporous boron nitride and boron-nitride-carbon materials from mesoporous silica templates. *J. Mater. Chem.* 2008, 18, 235-241.

21. Lin, L. X.; Li, Z. H.; Zheng, Y.; Wei, K. M. Synthesis and Application in the CO Oxidation Conversion Reaction of Hexagonal Boron Nitride with High Surface Area. *J. Am. Ceram. Soc.* 2009, 92, 1347-1349.

22. Schlienger, S.; Alauzun, J.; Michaux, F.; Vidal, L.; Parmentier, J.;

- Gervais, C.; Babonneau, F.; Bernard, S.; Miele, P.; Parra, J. B. Micro-, Mesoporous Boron Nitride-Based Materials Templated from Zeolites. *Chem. Mat.* 2012, 24, 88-96.
23. Arrigo, R.; Havecker, M.; Schlogl, R.; Su, D. S. Dynamic surface rearrangement and thermal stability of nitrogen functional groups on carbon nanotubes. *Chem. Commun.* 2008, 4891-4893.
24. Hao, G. P.; Li, W. C.; Qian, D.; Lu, A. H. Rapid Synthesis of Nitrogen-Doped Porous Carbon Monolith for CO₂ Capture. *Adv. Mater.* 2010, 22, 853-+.
25. Pevida, C.; Drage, T. C.; Snape, C. E. Silica-templated melamine-formaldehyde resin derived adsorbents for CO₂ capture. *Carbon* 2008, 46, 1464-1474.
26. Xia, Y. D.; Mokaya, R.; Walker, G. S.; Zhu, Y. Q. Superior CO₂ Adsorption Capacity on N-doped, High-Surface-Area, Microporous Carbons Templated from Zeolite. *Adv. Energy Mater.* 2011, 1, 678-683.
27. Zhao, Y. F.; Liu, X.; Yao, K. X.; Zhao, L.; Han, Y. Superior Capture of CO₂ Achieved by Introducing Extra-framework Cations into N-doped Microporous Carbon. *Chem. Mat.* 2012, 24, 4725-4734.
28. Chung, T. C. M.; Jeong, Y.; Chen, Q.; Kleinhammes, A.; Wu, Y. Synthesis of microporous boron-substituted carbon (B/C) materials using polymeric precursors for hydrogen physisorption. *J. Am. Chem. Soc.* 2008, 130, 6668-+.
29. Sheng, Z. H.; Gao, H. L.; Bao, W. J.; Wang, F. B.; Xia, X. H. Synthesis of boron doped graphene for oxygen reduction reaction in fuel cells.

J. Mater. Chem. 2012, 22, 390-395.

30. Lei, W.; Portehault, D.; Dimova, R.; Antonietti, M. Boron Carbon Nitride Nanostructures from Salt Melts: Tunable Water-Soluble Phosphors. *J. Am. Chem. Soc.* 2011, 133, 7121-7127.

31. Wang, S. Y.; Iyyamperumal, E.; Roy, A.; Xue, Y. H.; Yu, D. S.; Dai, L. M. Vertically Aligned BCN Nanotubes as Efficient Metal-Free Electrocatalysts for the Oxygen Reduction Reaction: A Synergetic Effect by Co-Doping with Boron and Nitrogen. *Angew. Chem.-Int. Edit.* 2011, 50, 11756-11760.

32. Li, X. H.; Antonietti, M. Polycondensation of Boron- and Nitrogen-Codoped Holey Graphene Monoliths from Molecules: Carbocatalysts for Selective Oxidation. *Angew. Chem.-Int. Edit.* 2013, 52, 4572-4576.

33. Iyyamperumal, E.; Wang, S. Y.; Dai, L. M. Vertically Aligned BCN Nanotubes with High Capacitance. *ACS Nano* 2012, 6, 5259-5265.

34. Guo, H. L.; Gao, Q. M. Boron and nitrogen co-doped porous carbon and its enhanced properties as supercapacitor. *J. Power Sources* 2009, 186, 551-556.

35. Portehault, D.; Giordano, C.; Gervais, C.; Senkovska, I.; Kaskel, S.; Sanchez, C.; Antonietti, M. High-Surface-Area Nanoporous Boron Carbon Nitrides for Hydrogen Storage. *Adv. Funct. Mater.* 2010, 20, 1827-1833.

36. Wu, Z. S.; Winter, A.; Chen, L.; Sun, Y.; Turchanin, A.; Feng, X. L.; Mullen, K. Three-Dimensional Nitrogen and Boron Co-doped Graphene for High-Performance All-Solid-State Supercapacitors. *Adv. Mater.* 2012, 24, 5130-5135.

37. Komatsu, T.; Goto, A. Synthesis and characterization of graphite-like B-C-N materials of composition $CN_x(BN)_y$ ($x \ll 1$, $y \leq 1$). *J. Mater. Chem.* 2002, 12, 1288-1293.
38. van den Berg, A. W. C.; Arean, C. O. Materials for hydrogen storage: current research trends and perspectives. *Chem. Commun.* 2008, 668-681.
39. Eberle, U.; Felderhoff, M.; Schuth, F. Chemical and Physical Solutions for Hydrogen Storage. *Angew. Chem.-Int. Edit.* 2009, 48, 6608-6630.
40. Jena, P. Materials for Hydrogen Storage: Past, Present, and Future. *J. Phys. Chem. Lett.* 2011, 2, 206-211.
41. Jeon, K.-J.; Moon, H. R.; Ruminski, A. M.; Jiang, B.; Kisielowski, C.; Bardhan, R.; Urban, J. J. Air-stable magnesium nanocomposites provide rapid and high-capacity hydrogen storage without using heavy-metal catalysts. *Nat Mater* 2011, 10, 286-290.
42. Schlapbach, L.; Züttel, A. Hydrogen-storage materials for mobile applications. *Nature* 2001, 414, 353-358.
43. Bastos-Neto, M.; Patzschke, C.; Lange, M.; Mollmer, J.; Moller, A.; Fichtner, S.; Schrage, C.; Lassig, D.; Lincke, J.; Staudt, R.; Krautscheid, H.; Glaser, R. Assessment of hydrogen storage by physisorption in porous materials. *Energy Environ. Sci.* 2012, 5, 8294-8303.
44. Lim, K. L.; Kazemian, H.; Yaakob, Z.; Daud, W. R. W. Solid-state Materials and Methods for Hydrogen Storage: A Critical Review. *Chem. Eng. Technol.* 2010, 33, 213-226.
45. Yurum, Y.; Taralp, A.; Veziroglu, T. N. Storage of hydrogen in nanostructured carbon materials. *Int. J. Hydrog. Energy* 2009, 34, 3784-3798.

46. Li, J. R.; Kuppler, R. J.; Zhou, H. C. Selective gas adsorption and separation in metal-organic frameworks. *Chem. Soc. Rev.* 2009, 38, 1477-1504.
47. Sculley, J.; Yuan, D. Q.; Zhou, H. C. The current status of hydrogen storage in metal-organic frameworks-updated. *Energy Environ. Sci.* 2011, 4, 2721-2735.
48. Jiang, H. L.; Liu, B.; Lan, Y. Q.; Kuratani, K.; Akita, T.; Shioyama, H.; Zong, F. Q.; Xu, Q. From Metal-Organic Framework to Nanoporous Carbon: Toward a Very High Surface Area and Hydrogen Uptake. *J. Am. Chem. Soc.* 2011, 133, 11854-11857.
49. Bhatia, S. K.; Myers, A. L. Optimum conditions for adsorptive storage. *Langmuir* 2006, 22, 1688-1700.
50. Wang, L. F.; Yang, R. T. New sorbents for hydrogen storage by hydrogen spillover - a review. *Energy Environ. Sci.* 2008, 1, 268-279.
51. Li, Y. W.; Yang, R. T. Hydrogen storage in metal-organic frameworks by bridged hydrogen spillover. *J. Am. Chem. Soc.* 2006, 128, 8136-8137.
52. Zubizarreta, L.; Menendez, J. A.; Pis, J. J.; Arenillas, A. Improving hydrogen storage in Ni-doped carbon nanospheres. *Int. J. Hydrog. Energy* 2009, 34, 3070-3076.
53. Tsao, C. S.; Tzeng, Y. R.; Yu, M. S.; Wang, C. Y.; Tseng, H. H.; Chung, T. Y.; Wu, H. C.; Yamamoto, T.; Kaneko, K.; Chen, S. H. Effect of Catalyst Size on Hydrogen Storage Capacity of Pt-Impregnated Active Carbon via Spillover. *J. Phys. Chem. Lett.* 2010, 1, 1060-1063.
54. Wang, L. F.; Yang, F. H.; Yang, R. T.; Miller, M. A. Effect of Surface

Oxygen Groups in Carbons on Hydrogen Storage by Spillover. *Ind. Eng. Chem. Res.* 2009, 48, 2920-2926.

55. Li, Y. W.; Yang, R. T. Significantly enhanced hydrogen storage in metal-organic frameworks via spillover. *J. Am. Chem. Soc.* 2006, 128, 726-727.

56. Lueking, A. D.; Yang, R. T. Hydrogen spillover to enhance hydrogen storage - study of the effect of carbon physicochemical properties. *Appl. Catal. A-Gen.* 2004, 265, 259-268.

57. Bhowmick, R.; Rajasekaran, S.; Friebel, D.; Beasley, C.; Jiao, L. Y.; Ogasawara, H.; Dai, H. J.; Clemens, B.; Nilsson, A. Hydrogen Spillover in Pt-Single-Walled Carbon Nanotube Composites: Formation of Stable C-H Bonds. *J. Am. Chem. Soc.* 2011, 133, 5580-5586.

58. Singh, A. K.; Ribas, M. A.; Yakobson, B. I. H-Spillover through the Catalyst Saturation: An Ab Initio Thermodynamics Study. *ACS Nano* 2009, 3, 1657-1662.

59. Kubas, G. J.; Ryan, R. R.; Swanson, B. I.; Vergamini, P. J.; Wasserman, H. J. CHARACTERIZATION OF THE 1ST EXAMPLES OF ISOLABLE MOLECULAR-HYDROGEN COMPLEXES, $\text{MO}(\text{CO})_3(\text{PCY}_3)_2(\text{H}_2)$, $\text{W}(\text{CO})_3(\text{PCY}_3)_2(\text{H}_2)$, $\text{MO}(\text{CO})_3(\text{PI-PR}_3)_2(\text{H}_2)$, $\text{W}(\text{CO})_3(\text{PI-PR}_3)_2(\text{H}_2)$ - EVIDENCE FOR A SIDE-ON BONDED H₂ LIGAND. *J. Am. Chem. Soc.* 1984, 106, 451-452.

60. Hoang, T. K. A.; Antonelli, D. M. Exploiting the Kubas Interaction in the Design of Hydrogen Storage Materials. *Adv. Mater.* 2009, 21, 1787-1800.

61. Zhao, Y. F.; Kim, Y. H.; Dillon, A. C.; Heben, M. J.; Zhang, S. B.

- Hydrogen storage in novel organometallic buckyballs. *Phys. Rev. Lett.* 2005, 94, 4.
62. Yildirim, T.; Ciraci, S. Titanium-decorated carbon nanotubes as a potential high-capacity hydrogen storage medium. *Phys. Rev. Lett.* 2005, 94, 4.
63. Lee, H.; Choi, W. I.; Ihm, J. Combinatorial search for optimal hydrogen-storage nanomaterials based on polymers. *Phys. Rev. Lett.* 2006, 97, 4.
64. Park, N.; Choi, K.; Hwang, J.; Kim, D. W.; Kim, D. O.; Ihm, J. Progress on first-principles-based materials design for hydrogen storage. *Proc. Natl. Acad. Sci. U. S. A.* 2012, 109, 19893-19899.
65. Lee, H.; Ihm, J.; Cohen, M. L.; Louie, S. G. Calcium-decorated carbon nanotubes for high-capacity hydrogen storage: First-principles calculations. *Phys. Rev. B* 2009, 80, 5.
66. Lee, H.; Ihm, J.; Cohen, M. L.; Louie, S. G. Calcium-Decorated Graphene-Based Nanostructures for Hydrogen Storage. *Nano Lett.* 2010, 10, 793-798.
67. Hamaed, A.; Trudeau, M.; Antonelli, D. M. H₂ storage materials (22KJ/mol) using organometallic Ti fragments as sigma-H₂ binding sites. *J. Am. Chem. Soc.* 2008, 130, 6992-6999.
68. Hoang, T. K. A.; Webb, M. I.; Mai, H. V.; Hamaed, A.; Walsby, C. J.; Trudeau, M.; Antonelli, D. M. Design and Synthesis of Vanadium Hydrazide Gels for Kubas-Type Hydrogen Adsorption: A New Class of Hydrogen Storage Materials. *J. Am. Chem. Soc.* 2010, 132, 11792-11798.
69. Hoang, T. K. A.; Morris, L.; Sun, J.; Trudeau, M. L.; Antonelli, D. M.

- Titanium hydrazide gels for Kubas-type hydrogen storage. *J. Mater. Chem. A* 2013, 1, 1947-1951.
70. Wang, Q.; Sun, Q.; Jena, P.; Kawazoe, Y. Potential of AlN Nanostructures as Hydrogen Storage Materials. *ACS Nano* 2009, 3, 621-626.
71. Sun, Q.; Wang, Q.; Jena, P.; Kawazoe, Y. Clustering of Ti on a C-60 surface and its effect on hydrogen storage. *J. Am. Chem. Soc.* 2005, 127, 14582-14583.
72. Sun, Q.; Jena, P.; Wang, Q.; Marquez, M. First-principles study of hydrogen storage on Li12C60. *J. Am. Chem. Soc.* 2006, 128, 9741-9745.
73. Lochan, R. C.; Head-Gordon, M. Computational studies of molecular hydrogen binding affinities: The role of dispersion forces, electrostatics, and orbital interactions. *Physical Chemistry Chemical Physics* 2006, 8, 1357-1370.
74. Dinca, M.; Long, J. R. Hydrogen storage in microporous metal-organic frameworks with exposed metal sites. *Angew. Chem.-Int. Edit.* 2008, 47, 6766-6779.
75. Jhi, S. H.; Kwon, Y. K. Hydrogen adsorption on boron nitride nanotubes: A path to room-temperature hydrogen storage. *Phys. Rev. B* 2004, 69.
76. Mpourmpakis, G.; Froudakis, G. E. Why boron nitride nanotubes are preferable to carbon nanotubes for hydrogen storage? An ab initio theoretical study. *Catal. Today* 2007, 120, 341-345.
77. Ma, R. Z.; Bando, Y.; Zhu, H. W.; Sato, T.; Xu, C. L.; Wu, D. H. Hydrogen uptake in boron nitride nanotubes at room temperature. *J. Am. Chem. Soc.* 2002, 124, 7672-7673.

78. Tang, C. C.; Bando, Y.; Ding, X. X.; Qi, S. R.; Golberg, D. Catalyzed collapse and enhanced hydrogen storage of BN nanotubes. *J. Am. Chem. Soc.* 2002, 124, 14550-14551.
79. Jhi, S. H. Activated boron nitride nanotubes: A potential material for room-temperature hydrogen storage. *Phys. Rev. B* 2006, 74.
80. Zhang, L. P.; Wu, P.; Sullivan, M. B. Hydrogen Adsorption on Rh, Ni, and Pd Functionalized Single-Walled Boron Nitride Nanotubes. *J. Phys. Chem. C* 2011, 115, 4289-4296.
81. Shevlin, S. A.; Guo, Z. X. Hydrogen sorption in defective hexagonal BN sheets and BN nanotubes. *Phys. Rev. B* 2007, 76, 11.
82. MacDowell, N.; Florin, N.; Buchard, A.; Hallett, J.; Galindo, A.; Jackson, G.; Adjiman, C. S.; Williams, C. K.; Shah, N.; Fennell, P. An overview of CO₂ capture technologies. *Energy Environ. Sci.* 2010, 3, 1645-1669.
83. Eide, L. I.; Bailey, D. W. Precombustion decarbonisation processes. *Oil Gas Sci. Technol.* 2005, 60, 475-484.
84. Figueroa, J. D.; Fout, T.; Plasynski, S.; McIlvried, H.; Srivastava, R. D. Advances in CO₂ capture technology - The US Department of Energy's Carbon Sequestration Program. *Int. J. Greenh. Gas Control* 2008, 2, 9-20.
85. D'Alessandro, D. M.; Smit, B.; Long, J. R. Carbon Dioxide Capture: Prospects for New Materials. *Angew. Chem.-Int. Edit.* 2010, 49, 6058-6082.
86. Samanta, A.; Zhao, A.; Shimizu, G. K. H.; Sarkar, P.; Gupta, R. Post-Combustion CO₂ Capture Using Solid Sorbents: A Review. *Ind. Eng. Chem. Res.* 2012, 51, 1438-1463.

87. Rochelle, G. T. Amine Scrubbing for CO₂ Capture. *Science* 2009, 325, 1652-1654.
88. Banerjee, R.; Phan, A.; Wang, B.; Knobler, C.; Furukawa, H.; O'Keeffe, M.; Yaghi, O. M. High-throughput synthesis of zeolitic imidazolate frameworks and application to CO₂ capture. *Science* 2008, 319, 939-943.
89. Hudson, M. R.; Queen, W. L.; Mason, J. A.; Fickel, D. W.; Lobo, R. F.; Brown, C. M. Unconventional, Highly Selective CO₂ Adsorption in Zeolite SSZ-13. *J. Am. Chem. Soc.* 2012, 134, 1970-1973.
90. Britt, D.; Furukawa, H.; Wang, B.; Glover, T. G.; Yaghi, O. M. Highly efficient separation of carbon dioxide by a metal-organic framework replete with open metal sites. *Proc. Natl. Acad. Sci. U. S. A.* 2009, 106, 20637-20640.
91. An, J.; Geib, S. J.; Rosi, N. L. High and Selective CO₂ Uptake in a Cobalt Adeninate Metal-Organic Framework Exhibiting Pyrimidine- and Amino-Decorated Pores. *J. Am. Chem. Soc.* 2010, 132, 38-39.
92. Park, H. J.; Suh, M. P. Enhanced isosteric heat, selectivity, and uptake capacity of CO₂ adsorption in a metal-organic framework by impregnated metal ions. *Chem. Sci.* 2013, 4, 685-690.
93. Lee, J.; Kim, J.; Hyeon, T. Recent progress in the synthesis of porous carbon materials. *Adv. Mater.* 2006, 18, 2073-2094.
94. Liang, C. D.; Li, Z. J.; Dai, S. Mesoporous carbon materials: Synthesis and modification. *Angew. Chem.-Int. Edit.* 2008, 47, 3696-3717.
95. Pevida, C.; Plaza, M. G.; Arias, B.; Feroso, J.; Rubiera, F.; Pis, J. J. Surface modification of activated carbons for CO₂ capture. *Appl. Surf. Sci.*

2008, 254, 7165-7172.

96. Feng, S. S.; Li, W.; Shi, Q.; Li, Y. H.; Chen, J. C.; Ling, Y.; Asiri, A. M.; Zhao, D. Y. Synthesis of nitrogen-doped hollow carbon nanospheres for CO₂ capture. *Chem. Commun.* 2014, 50, 329-331.
97. Luo, Y. L.; Li, B. Y.; Wang, W.; Wu, K. B.; Tan, B. Hypercrosslinked Aromatic Heterocyclic Microporous Polymers: A New Class of Highly Selective CO₂ Capturing Materials. *Adv. Mater.* 2012, 24, 5703-5707.
98. Xing, W.; Liu, C.; Zhou, Z. Y.; Zhang, L.; Zhou, J.; Zhuo, S. P.; Yan, Z. F.; Gao, H.; Wang, G. Q.; Qiao, S. Z. Superior CO₂ uptake of N-doped activated carbon through hydrogen-bonding interaction. *Energy Environ. Sci.* 2012, 5, 7323-7327.
99. Sevilla, M.; Valle-Vigon, P.; Fuertes, A. B. N-Doped Polypyrrole-Based Porous Carbons for CO₂ Capture. *Adv. Funct. Mater.* 2011, 21, 2781-2787.
100. Liu, L.; Deng, Q. F.; Hou, X. X.; Yuan, Z. Y. User-friendly synthesis of nitrogen-containing polymer and microporous carbon spheres for efficient CO₂ capture. *J. Mater. Chem.* 2012, 22, 15540-15548.
101. Vogiatzis, K. D.; Mavrandonakis, A.; Klopper, W.; Froudakis, G. E. Ab initio Study of the Interactions between CO₂ and N-Containing Organic Heterocycles. *ChemPhysChem* 2009, 10, 374-383.
102. Wang, X. J.; Li, P. Z.; Chen, Y. F.; Zhang, Q.; Zhang, H. C.; Chan, X. X.; Ganguly, R.; Li, Y. X.; Jiang, J. W.; Zhao, Y. L. A Rationally Designed Nitrogen-Rich Metal-Organic Framework and Its Exceptionally High CO₂ and H₂ Uptake Capability. *Sci Rep* 2013, 3, 5.

103. Park, K. S.; Lee, D. Y.; Kim, K. J.; Moon, D. W. Observation of a hexagonal BN surface layer on the cubic BN film grown by dual ion beam sputter deposition. *Appl. Phys. Lett.* 1997, 70, 315-317.
104. Song, L.; Ci, L. J.; Lu, H.; Sorokin, P. B.; Jin, C. H.; Ni, J.; Kvashnin, A. G.; Kvashnin, D. G.; Lou, J.; Yakobson, B. I.; Ajayan, P. M. Large Scale Growth and Characterization of Atomic Hexagonal Boron Nitride Layers. *Nano Lett.* 2010, 10, 3209-3215.
105. Leis, J.; Perkson, A.; Arulepp, M.; Kaarik, M.; Svensson, G. Carbon nanostructures produced by chlorinating aluminium carbide. *Carbon* 2001, 39, 2043-2048.
106. Poirier, E.; Dailly, A. Saturation properties of a supercritical gas sorbed in nanoporous materials. *Physical Chemistry Chemical Physics* 2012.
107. Sumida, K.; Horike, S.; Kaye, S. S.; Herm, Z. R.; Queen, W. L.; Brown, C. M.; Grandjean, F.; Long, G. J.; Dailly, A.; Long, J. R. Hydrogen storage and carbon dioxide capture in an iron-based sodalite-type metal-organic framework (Fe-BTT) discovered via high-throughput methods. *Chem. Sci.* 2010, 1, 184-191.
108. Choi, H.; Park, Y. C.; Kim, Y. H.; Lee, Y. S. Ambient Carbon Dioxide Capture by Boron-Rich Boron Nitride Nanotube. *J. Am. Chem. Soc.* 2011, 133, 2084-2087.
109. Seo, M. S.; Kim, J. H.; Kim, J. M.; Han, J. S.; Kang, S.; Ihm, J. S.; Kim, D. O. Tunable and selective formation of micropores and mesopores in carbide-derived carbon. *Carbon* 2013, 60, 299-306.
110. Han, F. D.; Bai, Y. J.; Liu, R.; Yao, B.; Qi, Y. X.; Lun, N.; Zhang, J.

- X. Template-Free Synthesis of Interconnected Hollow Carbon Nanospheres for High-Performance Anode Material in Lithium-Ion Batteries. *Adv. Energy Mater.* 2011, 1, 798-801.
111. Wang, C. W.; Wang, Y.; Graser, J.; Zhao, R.; Gao, F.; O'Connell, M. J. Solution-Based Carbohydrate Synthesis of Individual Solid, Hollow, and Porous Carbon Nanospheres Using Spray Pyrolysis. *ACS Nano* 2013, 7, 11156-11165.
112. Jia, C. J.; Sun, L. D.; Yan, Z. G.; You, L. P.; Luo, F.; Han, X. D.; Pang, Y. C.; Zhang, Z.; Yan, C. H. Iron oxide nanotubes - Single-crystalline iron oxide nanotubes. *Angew. Chem.-Int. Edit.* 2005, 44, 4328-4333.
113. Fellingner, T. P.; Hasche, F.; Strasser, P.; Antonietti, M. Mesoporous Nitrogen-Doped Carbon for the Electrocatalytic Synthesis of Hydrogen Peroxide. *J. Am. Chem. Soc.* 2012, 134, 4072-4075.
114. Myers, A. L.; Prausnitz, J. M. THERMODYNAMICS OF MIXED-GAS ADSORPTION. *Aiche J.* 1965, 11, 121-+.
115. Song, C.; Du, J. P.; Zhao, J. H.; Feng, S. A.; Du, G. X.; Zhu, Z. P. Hierarchical Porous Core-Shell Carbon Nanoparticles. *Chem. Mat.* 2009, 21, 1524-1530.
116. Lee, J. H. Gas sensors using hierarchical and hollow oxide nanostructures: Overview. *Sens. Actuator B-Chem.* 2009, 140, 319-336.
117. Sevilla, M.; Foulston, R.; Mokaya, R. Superactivated carbide-derived carbons with high hydrogen storage capacity. *Energy Environ. Sci.* 2010, 3, 223-227.
118. Sevilla, M.; Mokaya, R. Activation of carbide-derived carbons: a

route to materials with enhanced gas and energy storage properties. *J. Mater. Chem.* 2011, 21, 4727-4732.

119. Zhao, L.; Fan, L. Z.; Zhou, M. Q.; Guan, H.; Qiao, S. Y.; Antonietti, M.; Titirici, M. M. Nitrogen-Containing Hydrothermal Carbons with Superior Performance in Supercapacitors. *Adv. Mater.* 2010, 22, 5202-+.

120. Chen, H. C.; Sun, F. G.; Wang, J. T.; Li, W. C.; Qiao, W. M.; Ling, L. C.; Long, D. H. Nitrogen Doping Effects on the Physical and Chemical Properties of Mesoporous Carbons. *J. Phys. Chem. C* 2013, 117, 8318-8328.

121. Bae, T. H.; Hudson, M. R.; Mason, J. A.; Queen, W. L.; Dutton, J. J.; Sumida, K.; Micklash, K. J.; Kaye, S. S.; Brown, C. M.; Long, J. R. Evaluation of cation-exchanged zeolite adsorbents for post-combustion carbon dioxide capture. *Energy Environ. Sci.* 2013, 6, 128-138.

Further works

We found out that aluminum doping in boron nitride cause significant enhancement of hydrogen binding energy. Synthesis of Al_B-BN should be followed to confirm its quality as a hydrogen storage candidate.

Although hollow structure of nitrogen and boron co-doped porous carbon (CNB) without additional hard template is developed, the optimization or compositional flexibility are not done yet. More researches about these are needed.

Further investigation of CNBs as another application candidates, such as supercapacitors, lithium ion batteries and catalysts, is proceeding now. The morphological or compositional role of CNBs in these applications will be discussed.

Publications List

Kim, J. H.; Han, J. S.; Ha, D. K.; Kang, S. Synthesis of Conformal Boron-aided nitrogenous Porous Carbon: from Porous to Hollow Structure. *Submitted*.

Kim, J. H.; Han, J. S.; Seo, M. S.; Kang, S.; Kim, D.; Ihm, J. High-Surface Area Ceramic-Derived Boron-Nitride and its Hydrogen Uptake Properties. *J. Mater. Chem. A* **2013**, *1*, 1014–1017.

Seo, M. S.; **Kim, J. H.**; Kim, J. M.; Han, J. S.; Kang, S.; Ihm, J. S.; Kim, D. O. Tunable and Selective Formation of Micropores and Mesopores in Carbide-Derived Carbon. *Carbon* **2013**, *60*, 299–306.

초록

CDC (carbide derived carbon) 의 특별한 특성이 처음 발견된 이래로 이 물질은 다양한 응용 물질에 대하여 연구가 진행되어 왔으며 그 특성은 매우 흥미롭고 뛰어나다는 것이 밝혀졌다. 하지만 이 방법의 매우 유용한, 전구체의 모양을 그대로 닮아가면서 합성 방법이 매우 간단하다는 장점을 다른 조성에 사용하는 것은 매우 제한되어 왔다. 그 이유는 이 방법을 사용하는 온도와 할로젠 분위기 하에서 다른 기능화 시킬 수 있는 원자들이 매우 불안정 하여서 생산물로 남지 못하고 대부분이 부산물로 사라져 버리기 때문이다. 우리는 이 논문에서 위 방법을 사용하여 순수한 탄소 물질 뿐만 아니라 탄소와 유사한 구조를 가지고 있고 최근 들어 그 관심이 점점 늘어나고 있는 C-B-N 물질을 합성함으로써 기존의 한계를 넘어서고자 하였다.

탄소의 인접 원자인 질소와 붕소는 탄소의 유무와 관계 없이 그들의 전자 구조로 인하여 상호 보완적인 역할을 한다. 비록 그들은 서로 직접적으로 연결이 되어 B-N 결합을 형성할 때가 가장 안정하지만 붕소의 첨가는 주로 탄소로 이루어져 있는 구조 하에서 질소 기능 기의 안정화를 유도하기도 한다. 우리는 이러한 개념을 기반으로 다양한 조성의 C-N-B 물질을 합성할 수 있었다.

주목할 만한 수소와 이산화탄소 흡착 또한 합성된 C-N-B 에서 발

견할 수 있었다. 이 흡착량은 물질의 조성과 표면적에 따라 극명하게 변화를 하였다. 우선 다공성의 질화 붕소의 경우에는 순수한 탄소 물질에 비하여 향상된 흡착 에너지를 나타내었다. 반면에 질소와 붕소가 같이 치환된 다공성 탄소의 경우에는 높은 이산화탄소 흡착량을 보여주었는데 특히 많은 질소를 함유한 전구체를 사용하여 합성된 속이 빈 구조에서 가장 높은 이산화탄소 흡착량이 나타났다. 이때 이산화탄소와 질소의 선택적 흡착 또한 가장 뛰어난 것으로 조사되었다. 이러한 가스의 흡착은 활성화 과정이나 적당한 원소의 치환을 통하여 더욱더 증대시킬 수 있다는 것 또한 증명되었다.

주요어 : CDC (Carbide derived carbon), 질화 붕소, 질소 도핑, 수소 저장, 이산화탄소 흡착, 제일원리 계산.

학번 : 2008-20636